A DILATANT TWO-FLUID DEBRIS FLOW MODEL FOR HAZARD ANALYSIS IN CHANGING MOUNTAIN ENVIRONMENTS

A thesis submitted to attain the degree of

DOCTOR OF SCIENCES of ETH ZURICH

(Dr. Sc. ETH Zurich)

Presented by

GUILLAUME MEYRAT

M.Sc. Physics, EPFL

Born on August 2nd, 1993

Citizen of Switzerland

Accepted on the recommendation of

Prof. Dr. C. R. Müller, examiner

Assoc. Prof. Dr. R. Kaitna, co-examiner

Dr. P. Bartelt, co-examiner

Dr. B. McArdell, co-examiner

2023

Contents

Cette thèse est dédicassée à la mémoire de Thibault Gerber, alias Le Gauche.

List of Symbols

Symbol	Description
$h_{(*)}$	Height $[m]$
$\vec{v}_{(*)}$	Velocity $[ms^{-1}]$
$\rho_{(*)}$	Density $[kgm^{-3}]$
$M_{(*)}$	Mass per unit of basal area (A) $[kgm^{-2}]$
$M_{(*)}$	Mass $[kg]$
$N_{(*)}$	Normal stress $[Pa]$
$\mu_{(*)}$	Coulomb friction coefficient $(= tan(\varphi))$ $[]$
$\xi_{(*)}$	Turbulent (Chezy) friction coefficient $[ms^{-2}]$
$\vec{\tau}_{(*)}$	Shearing stress $[Pa]$
L	Flow length $[m]$
A	Cell's basal area $[m^2]$
V	Flow volume $[m^3]$
$\phi_{s,f}$	Solid, fluid volumetric concentration $[]$
D	Dilatancy $[m^s-1]$
$\vec{g}$	Gravitational accelaration $[ms^{-2}]$
κ	Lateral pressure coefficient $[]$
ψ	Granular dilatancy angle $[]$
χ	Debris elastic compressibility $[Pa^{-1}]$
k	Hydraulic permeability $[m^2s^{-2}]$
ν	Fluid viscosity $[Pas^{-1}]$
p	Fluid pressure $[Pa]$
p_h	Hydrostatic fluid pressure $[Pa]$
p_e	Excess fluid pressure $[Pa]$
p_b	Bottom fluid pressure $[Pa]$
p_A	Atmospheric pressure $[Pa]$
θ	Slope angle $[]$
Q_f	Inter-layer fluid exchange $[ms^{-1}]$
$\vec{P}$	Momentum exchange rate (per unit of fluid density and basal area) $[m^2s^{-2}]$
$\vec{\tau}_{sf}$	Inter-phase momentum stress $[Pa]$
η	Parameter governing the viscous shearing force magnitude between the solid and the fluid $[kgm^{-3}s^{-1}]$
γ	Shear strain $[]$
$\phi_{s,eq}$	Equilibrium volumetric solid fraction configuration $[]$
φ	Solid friction angle $(= \tan^{-1}(\mu))$ $[]$
K	Proportionality factor used to compute the solid matrix dilatancy $[]$
C_{NN} [*1]	Coefficient governing the magnitude of the non-Newtonian part of the fluid stress $[kgm^{-1}s^{-1}]$
C_{DG} [*1]	Coefficient governing the magnitude of the solid-fluid viscous drag term $[kgm^{-3}]$
C_{VMG} [*1]	Coefficient governing the magnitude of the virtual mass term $[kgm^{-2}]$
$j = 1, 2$ [*1]	coefficient allowing to choose between a laminar ($j = 1$) or turbulent ($j = 2$) flow friction
E_s	Solid erosion rate $[ms^{-1}]$
E_f	Fluid erosion rate $[ms^{-1}]$
E_1	First layer erosion rate $[ms^{-1}]$
E_s^{ri} [*1]	Coefficient governing the magnitude of the solid erosion rate $[]$
E_f^{ri} [*1]	Coefficient governing the magnitude of the fluid erosion rate $[m^{-1}]$
d_{max}	Maximum potential erosion depth $[m]$
$\frac{dz}{d\tau}$	Critical shear coefficient $[mPa^{-1}]$
τ_c	Shear stress threshold erosion value $[Pa]$
V_D	Dilatant potential energy $[J]$
W_f	Shear forces work [J]

α	Dilatant potential energy production coefficient []
β	Dilatant potential energy decay coefficient $[s^{-1}]$
Γ	$(= \alpha/\beta)$ Mean collapse time $[s]$
b	Bottom topography $[m]$
a	Acceleration $[ms^{-2}]$
τ	Stress tensor $[Pa]$
$\kappa, \kappa_n, \kappa_{n,m}$ $(n, m = x, y, z)$	Lateral pressure coefficient []
ϵ	Aspect ratio []
Δx	Grid size $[m]$
Gr	Granule size $[cm]$

The initial notation from the original papers [1, 2, 3, 4, 5, 6] has been changed for uniformity purposes. The value with a superscripted star indicates that an index can be added.

[*1] Only defined for the *r.avaflow* model.

Abstract

Gravitationally driven flows of mud and sediment debris are causing a growing threat to mountain populations. Rock/ice avalanches, glacier lake outburst floods (GLOFs) and debris flows are increasingly a result of a global temperature rise, which is leading directly to the thawing of mountain permafrost and melting of glaciers. When coupled with extreme precipitation events, the mobilization of loose sediments leads to dangerous water-saturated flows that can cause human fatalities and severe infrastructure damage. Understanding the dynamics of debris flows is essential to develop land planning and technical measures to protect mountain communities.

Numerical modeling of debris flows provides hazard engineers with a predictive tool to help plan and construct mitigation measures, including developing real-time warning systems. With the recent increase in computer power, it is now possible to simulate debris flow motion from initiation to run-out. Numerical modeling therefore links initial conditions, including precipitation and sediment availability, to flow conditions in the torrent and run-out fan. Despite recent progress, the application of numerical models is limited by the lack of understanding of the general kinematical behavior of two-phase flows, including the frictional interaction of fluid-solid mixtures with the basal surface, as well as the shearing interaction between the solid and fluid phases. The rheological problem is compounded by the complex interaction of the debris with the basal surface leading to bed erosion. Modeling debris flow motion with entrainment involves accurately predicting the interplay between debris flow composition (time evolution of the solid-fluid components) coupled with the geological setting. The lack of understanding of these complex physical processes and geo-mechanical feed-backs is preventing a reliable, and predictive, application of debris flow models in engineering practice.

In this thesis, we develop, test and calibrate a depth-averaged, two-fluid debris flow model with erosion and dilatancy. The model consists of six partial differential equations governing mass, momentum, and granular temperature. The key feature of the model is to include dilatant effects that are associated with the shearing of granular debris. We assume that the expansive and contracting action of the solid volume under shearing governs the volume of the pore space and therefore the behavior of the interstitial fluid. Moreover, the dilatant response of the solid matrix governs mass and momentum exchanges between the two layers. The model is validated using actual, field-scale debris flow measurements from the Swiss Illgraben test site (Wallis, Switzerland). The comparison between Illgraben data and the simulations reveals that the model reproduces the space-time evolution of the solid/fluid flow composition in the streamwise direction, meaning from the leading edge of the debris flow to the debris flow tail.

Following the model development, we investigate the connection between the flow composition and the flow rheology. As the well-known debris flow scientist Iverson argued [7], it is impossible to accurately simulate a debris flow from initiation to run-out using a fixed and uniform rheology. Based on Illgraben data, as well as on careful laboratory experiments, we find a physical formulation where the flow composition evolution governs the rheological changes. We propose two different methods to compute the frictional resistance from the solid/fluid composition of the flow. They are conceptually different but mathematically equivalent to large degrees. We test and compare these two approaches using data from the torrent of Ritigraben (Wallis, Switzerland). Additionally, we

introduce an erosion model adapted for two-layer debris flow, in which erosion is also a function of the flow composition. Drone flights performed before and after a specific debris flow event in Ritigraben provide us with reliable and rare erosion data, which allows us to test and calibrate the rheological and erosion models. The numerical results are in good agreement with the field measurements.

In the final theme presented in this thesis, we validate the proposed two-layer debris flow model using several well-documented case events. We study three GLOFs, two that occurred in Peru (Lake 513, 2010 and Lake Palcacocha, 1941) and one in Kyrgyzstan (Lake Uchitel in the Aksay Valley). The event documentation contains precise field observations, making the direct comparison and analysis of the model results consistent and insightful. A characteristic of long-running GLOFs is the transformation in the flow composition from initiation to run-out. Directly after initiation, usually from a moraine collapse, the flow consists primarily of fluid. However, as the flow acquires solid material via bed erosion, the flow transforms from a mud flow to a type of granular debris flow. Conversely, as the slope flattens, the solid matrix collapses (contracts) and therefore stops while the fluid which is washed-out of the interstitial pore space and continues to flow downstream. As the proposed frictional rheology depends on the internal solid-fluid composition, modeling these transitions is crucial for a model's accuracy. We demonstrate that the model can reproduce the entire flowing behavior of all three events, for which many of flowing transitions and phase separations occurred. The back-calculation of the three GLOF events is performed using the same set of rheological parameters for all three case studies.

In summary, we develop a dilatancy-based, two-fluid debris flow model that captures flow regime transitions based on the evolution of the solid-fluid composition. This composition depends directly on erosion and deposition processes which are driven in turn by the rheological behavior and the terrain topography. We test the proposed model on real-scale field data obtained from two debris flow sites in Switzerland. Finally, we apply the model to simulate well-documented GLOF events. Future applications will help to determine if the proposed model can be used for practical hazard analysis in changing mountain environments.

Résumé

Les écoulements gravitationnels de débris et de boue constituent une menace croissante pour les populations de montagne. Les avalanches de roches et de glace, les débordements de lacs glaciaires et les laves torrentielles sont de plus en plus fréquents, résultant de l'augmentation globale de la température, conduisant directement au dégel du permafrost de haute montagne et à la fonte des glaciers. Associée à des précipitations extrêmes, la mobilisation de sédiments instables entraîne des écoulements de débris saturés en eau qui peuvent mettre en danger les populations de montagne ainsi que causer de graves dommages aux infrastructures civiles. Il est essentiel de comprendre la dynamique de ce type d'écoulement granulaire pour élaborer des mesures d'aménagement du terrain et des stratégies visant à protéger les communautés de montagne.

La modélisation numérique des laves torrentielles fournit aux ingénieurs un outil de prédiction qui les aide à planifier et à mettre en place des mesures d'atténuation, notamment en développant des systèmes d'alerte en temps réel. Grâce à l'augmentation récente de la puissance des ordinateurs, il est désormais possible de simuler l'écoulement des laves torrentielles depuis leur initiation jusqu'à leur dépôt. La modélisation numérique établit donc un lien entre les conditions initiales, notamment les précipitations et la répartition spatiale des roches instables, les conditions d'écoulement dans le torrent et la zone de dépôt. Malgré les progrès récents, l'application des modèles numériques est limitée par le manque de compréhension de la dynamique globale des écoulements biphasiques, y compris la friction entre le mélange fluide-solide de l'écoulement et le sol, ainsi que l'interaction entre les phases solides et fluides. Ce problème rhéologique est aggravé par l'interaction complexe des débris rocheux avec le terrain, ce qui conduit à l'érosion du canal. La modélisation du mouvement de la coulée de débris avec entraînement implique de prédire avec précision l'interaction entre la composition de la coulée de débris (évolution temporelle des composants solides-fluides) et le contexte géologique. Le manque de compréhension de ces processus physiques complexes et des rétroactions géo-mécaniques empêche une application fiable et prédictive des modèles de laves torrentielles dans la pratique de l'ingénierie.

Dans cette thèse, nous développons, testons et calibrons un modèle de coulée de débris de type 'à deux fluides', moyenné sur la hauteur, incluant les processus d'érosion et de dilatation. Le modèle se compose de six équations différentielles partielles régissant la masse, la quantité de mouvement et les fluctuations granulaires. La principale caractéristique du modèle est d'inclure les effets de dilatation qui sont induits par l'interaction des débris granulaires avec la topographie rugueuse du terrain. Nous supposons que l'action d'expansion et de contraction du volume du solide régit le volume de l'espace poreux contenu entre les débris rocheux et donc le comportement du fluide interstitiel. De plus, la réponse dilatante de la matrice solide régit les échanges de masse et de quantité de mouvement entre les deux couches. Le modèle est validé en utilisant des mesures de laves torrentielles naturelles sur le site de mesures suisse de l'Illgraben (Valais, Suisse). La comparaison entre les données de l'Illgraben et les simulations révèle que le modèle reproduit l'évolution spatio-temporelle de la composition de la lave torrentielle (solide/fluide).

Après le développement du modèle, nous étudions le lien entre la composition (solide/fluide) de l'écoulement et sa rhéologie. Comme l'a postulé le célèbre spécialiste des laves torrentielles Iverson, il est impossible de simuler avec précision une coulée de débris de son initiation à son écoulement en utilisant une rhéologie constante et uniforme, [7]. En nous basant sur les données de l'Illgraben, ainsi que sur des expériences de laboratoire, nous trouvons une formulation physique où

les changements rhéologiques sont gouvernés par l'évolution de la composition de l'écoulement. Nous proposons deux méthodes différentes pour calculer la résistance de friction à partir de la composition solide/fluide de l'écoulement. Elles sont conceptuellement différentes mais mathématiquement quasiment équivalentes. Nous testons et comparons ces deux approches sur les données du torrent de Ritigraben (Wallis, Suisse). De plus, nous introduisons un modèle d'érosion adapté aux modèles de laves torrentielles à deux couches, dans lequel l'érosion est également fonction de la composition de la lave torrentielle. Des vols de drone effectués avant et après une lave torrentielle à Ritigraben nous fournissent des données d'érosion fiables et rares, qui nous permettent de tester et de calibrer les modèles rhéologiques et d'érosion. Les résultats numériques sont en bon accord avec les mesures de terrain.

Dans le dernier thème présenté dans cette thèse, nous validons le modèle de laves torrentielles à 'deux couches' en utilisant plusieurs événements bien documentés. Nous étudions trois débordements de lacs glaciaires, deux qui se sont produits au Pérou (lac 513, 2010 et lac Palcacocha, 1941) et un au Kirghizstan (lac Uchitel dans la vallée d'Aksay). La documentation de ces événements contient des observations de terrain précises, ce qui rend la comparaison directe et l'analyse des résultats du modèle cohérentes. Une caractéristique des débordements de lacs glaciaires est la transformation de la composition de l'écoulement entre le début et la fin. Directement après l'initiation, généralement à partir d'un effondrement de moraine, l'écoulement est principalement composé de fluide. Cependant, lorsque l'écoulement acquiert des matériaux solides par l'érosion du torrent, il passe d'une coulée de boue à un écoulement proche voire équivalent à une lave torrentielle. Inversement, lorsque la pente s'aplatit, la matrice solide se contracte et s'arrête tandis que le fluide continue à s'écouler en aval. Comme la rhéologie proposée dépend de la composition interne solide-fluide, la modélisation de ces transitions est cruciale pour la précision d'un modèle. Nous démontrons que le modèle peut reproduire l'ensemble du comportement d'écoulement des trois événements, pour lesquels de nombreuses transitions d'écoulement et séparations de phases se sont produites. Le rétrocalcul des trois événements GLOF est effectué en utilisant le même ensemble de paramètres rhéologiques pour les trois cas étudiés.

En résumé, nous développons un modèle de coulée de débris à 'deux fluides' basé sur la dilatation qui capture les transitions de régime d'écoulement en fonction de l'évolution de la composition solide-fluide. Cette composition dépend directement des processus d'érosion qui sont à leur tour déterminés par le comportement rhéologique et la composition de l'écoulement. Nous avons testé le modèle proposé sur des données de terrain à échelle réelle obtenues à partir de deux sites de mesure de lave torrentielle en Suisse. Enfin, nous avons appliqué le modèle pour simuler des débordements de lacs glaciaires bien documentés. Les applications futures permettront de déterminer si le modèle proposé peut être utilisé pour l'analyse pratique des risques dans des environnements montagneux.

Chapter 1

Introduction

1.1   Motivation

Climatic warming is significantly impacting mountain areas throughout the world. There exists increasing alarm concerning the danger arising from hazardous alpine mass movements such as debris flows, rock-ice avalanches, landslides and rockfalls, [8,9,10,11,12,13]. Of particular concern is the fact that the magnitude and frequency of debris flows are expected to increase because of extreme precipitation events, coupled with intense drought periods [14]. Debris flows are gravitationally driven, water-saturated granular flows that can transform harmless mountain streams into raging torrents of fast moving, muddy debris. They can arise as primary flows after intense precipitation, or they can arise as secondary, cascading flows after rock/ice avalanches. The loss of stability of both high mountain permafrost slopes as well as ice masses because of increasing temperatures is further driving the interest in the problem of debris hazard mitigation. In the European Alps, the effect of climatic warming can already be observed, leading to the occurrence of many dramatic events during the last few years. For instance, in 2017 in Piz Cengalo (Grison, Switzerland), eight hikers were killed after a rock/ice avalanche and a significant part of the Bondo village was destroyed by secondary debris flows [15,16,17], middle panel of Fig. 1.1. Another example occurred in 2019 in Chamoson (Wallis, Switzerland), where two persons lost their lives in dramatic circumstances [18, 19], left panel of Fig. 1.1.

Figure 1.1: **Left)** *The 2019 debris flow in Chamoson, (photo [20])* **Middle)** *After the collapse of Piz Cengalo, a debris flow partially destroyed the village of Bondo in 2017, (photo [21]).* **Right)** *A car with 6 persons inside is taken by a debris flow near Jaun (Fribourg, CH). Luckily, there were no fatalities, (photo [22]).*

Climatic warming is not only causing danger in the mountains of Switzerland. In the high mountain regions of Central Asia and South America, the retreat of glaciers creates moraine-dammed lakes (left panel of Fig. 1.3), [23, 24, 25, 26, 27, 28, 29]. The moraines are composed of an assortment of loose rocks interlaced with ice. They are highly unstable, especially in a warming climate. The sudden breaching of the dams is extremely dangerous to the downstream regions which are often densely populated [30, 31, 32, 33, 34]. The magnitude of such events can be tremendous. Indeed maximum peak discharges that reach 30'000 m^3/s and run-out distances of more than 200 km have been recorded [29]. According to a recent study, [25] taken up by the Swiss Radio and Television service (SRF) [35], 15 million persons are threatened by glacier lake outburst floods (GLOFS) in the world, 700'000 alone in Switzerland, Fig. 1.2.

To develop efficient mitigation strategies in alpine and high-mountain environments, there is a need to accurately predict the formation and flow dynamics of debris flows. In the past 20 years, several debris flow models have been developed for natural hazard analysis and prevention [1, 2, 3, 4, 5, 6, 38, 39, 40, 41]. The models are numerical, modeling debris flow motion from initiation to run-out, and are primarily based on depth-averaged approaches. Although three-dimensional models exist [42], one-dimensional (1-D) and two-dimensional (2-D) models are more prevalent. For practical applications all models must satisfy the following criteria:

1. They must have *predictive* capacity. Moreover, given a set of initial conditions (e.g. torrent geometry, estimated discharge and sediment content), the models must accurately predict debris flow velocity and run-out within acceptable accuracy. The underlying assumption behind this requirement is that debris flow models are deterministic, not statistical or probabilistic. Accurate predictions of debris flow run-out place great demands on the models since physical relationships are required to model debris flow rheology and entrainment processes. A deterministic modeling approach has a long tradition in Switzerland, where deterministic models are applied to produce snow avalanche and rockfall hazard maps ([43, 44]). The advantage of deterministic models is that they allow engineers to make process-based evaluations based on both observations (historical case studies) and therefore field experience.

2. They must provide solutions within *acceptable time limits*. The majority of debris flow problems in Switzerland and worldwide are solved by engineering offices with limited computational resources. Because of the lack of knowledge concerning initial and boundary conditions, engineering solutions are often based on hazard scenarios. These scenarios vary discharge amounts and entrainment rates to simulate likely, and less likely, but extreme events. The results are usually classified with respect to an event frequency, or return period. This methodology implies that a single debris flow problem involves a great number of simulations, that must be executed within a short time period. Presently, three-dimensional modeling approaches [42, 45, 46] give perhaps more precise results but are too expensive with respect to computing time to be useful for operational purposes.

3. The models must contain *few parameters*, with a narrow confidence interval for each free parameter. The selection of appropriate rheological parameters for mitigation and hazard mapping is a long-standing problem. In fact, it can be considered the most important problem confronting debris flow science and practice. The problem arises for many reasons. Debris flows consist of varying parts of fluid (mud) and solid (bouldery debris). As such the rhe-
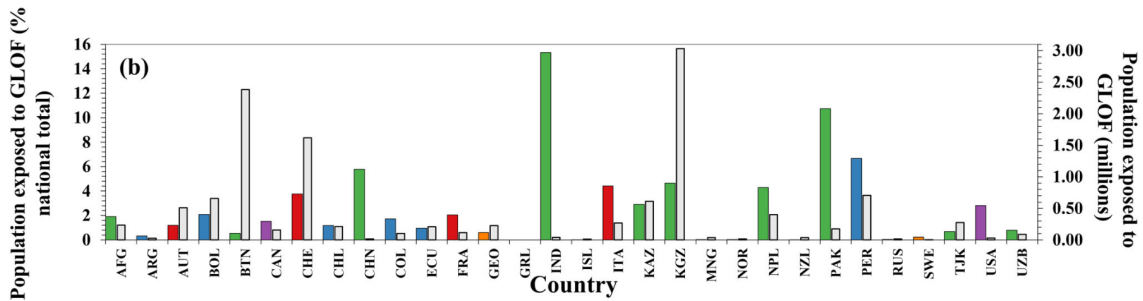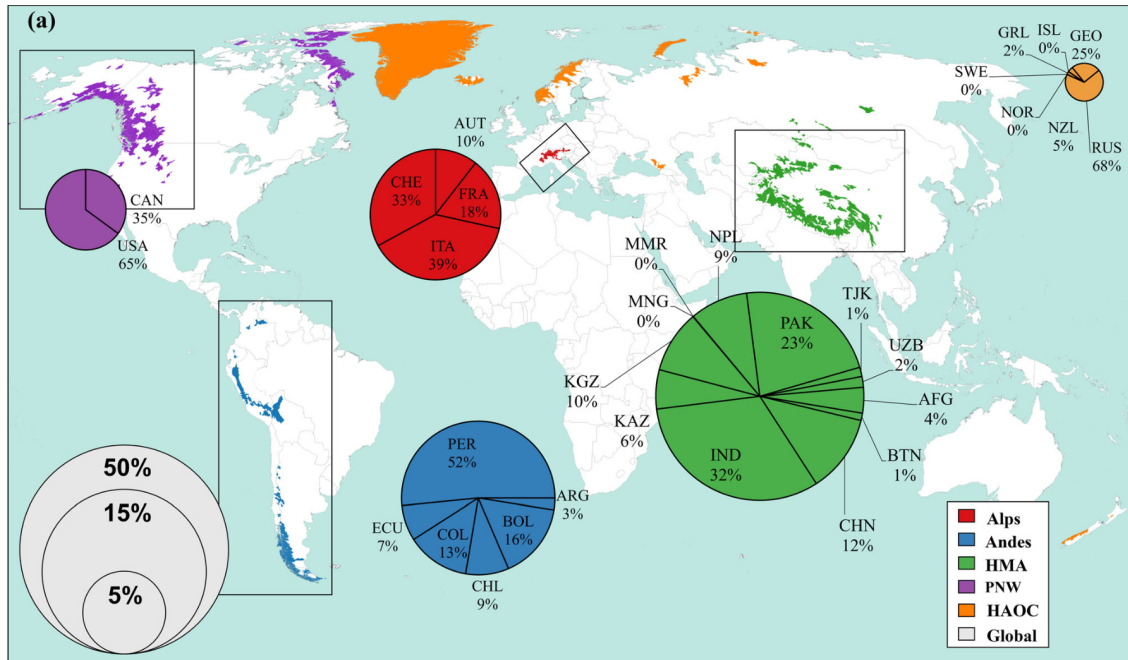
Figure 1.2: **a** *Global distribution of glacial basins, colour-coded according to mountain range, with 'High Arctic and Outlying Countries' (HAOC) representing all basins outside of the four main ranges in this study (Alps, Andes, High Mountains Asia (HMA) and Pacific North West (PNW)). Pie charts show the proportion of exposed population as individual country contributions to the mountain range total, with pie charts sized according to percentage contribution to the 2020 global total.* **b** *Grey bars show exposed population as a percentage of the national total (left axis). Coloured bars show the total exposed population per country (right axis). Fig. and caption from [25]*

Figure 1.3: **Left)** *Palcacocha Glacier lake which initiates the dramatic GLOF of 1941, (photo: Alexander Luna, [36]).* **Right)** *In 1941, the collapse of a glacier fell into the Lake Palcacocha, initiating GLOFs that transformed into a debris flow and destroyed a large part of the city center of Huaraz (Cordillera Blanca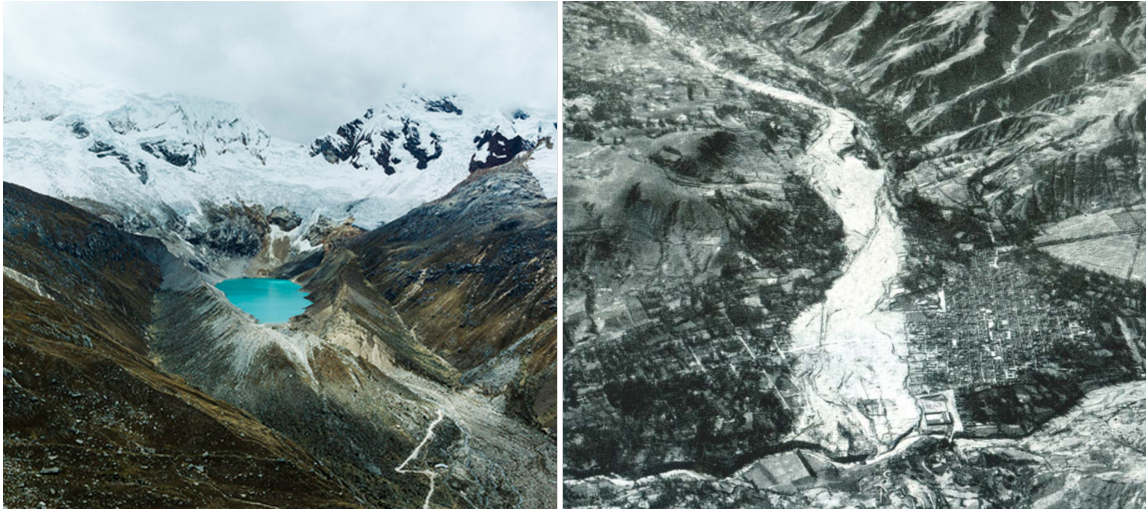, Peru), after having entrained the entire Lake Jircacocha (which does not exist anymore since). Tragically, almost 2000 persons died, [37], (photo Arnold Heim).*

ological description must account for a wide range of material mixtures. A debris flow will exhibit different flow regimes, depending on the geomorphic setting of the torrent, as well as the initial precipitation rates. During complex events, like GLOFs, the flow can increase (over entrainment of solid material) or decrease (over deposition of solid material) its internal volumetric solid concentration leading to significant changes in the solid/fluid composition and, therefore, flow rheology, [47]. This large diversity of flow regimes leads to the use of free parameters whose possible values are usually poorly constrained. Therefore, the capability of these models to make reliable predictions is questionable. Furthermore, to simulate the different flow types and their rheology occurring during an event, different sets of free parameters are needed. Even if this procedure can work to back-compute past events, it is not suitable for prediction, because it is based on information about the specific, back-computed event. Consequently, modeling the solid/fluid concentration evolution as well as the flowing transitions and phase separations is crucial to increase the model's accuracy and improve its predictions' reliability. The basic problem is in many ways experimental, as little measured data exists to quantify the rheology of different mixtures. Alternatively, the problem is also numerical, in the sense that models must simulate the mixture composition before they can apply rheological parameters obtained from experiments.

This thesis involves all three criteria of debris flow modeling: we seek an accurate, reliable debris flow model capable of making accurate predictions within the framework of scenario-based risk analysis. The model must provide solutions within a reasonable time and can be employed within the existing computational environment of most hazard engineering offices. Furthermore, we seek a model with few tunable parameters such that the model can be applied with confidence by hazard engineers. The rheological parameters must be supported by field-scale experimental measurements. The common limitation of existing models is the use of free parameters to reproduce

the complex behavior of granular, fluid-saturated debris flow. Consequently, the predictive ability of existing models is limited because the results strongly depend on the precise value of these often abstract and poorly defined free parameters.

In the next chapter, we will overview several one- and two-dimensional depth-averaged models used for debris flow mitigation. Although the section does not take all existing models into account, it serves to classify the wide range of numerical approaches existing in the literature. Existing models differ by how they include the fluid momentum balance, whether they include granular dilatancy, and how they treat excess pore fluid pressures. Although each model is based on some form of a Coulomb rheology, there are strong differences in how each model simulates fluid friction. By far the widest divergence in modeling approaches concerns how to mathematically describe the interactions between the solid particles and the viscous muddy fluid. A precise and complete description of the momentum transfer between the solid phase and the fluid one is extremely challenging, especially in the framework of a macroscopic (depth-averaged) description of the flow.

1.2   Goal of the Thesis

In this thesis we develop a depth-averaged two-fluid (two-layer) model that can accurately compute debris flow velocity, run-out distance, entrainment, deposition of solid material, solid-fluid space-time evolution and phase separation, given a well-defined set of initial and boundary conditions. Our primary aim is to build a theoretically well-founded, computationally robust debris flow model for hazard mitigation and analysis. We place the following constraints on the model development:

1. It applies well-accepted concepts of granular mechanics (dilatancy) and two-phase geophysical flows (solid-fluid interactions). The model should account for variable debris flow density, arising not only from different variations of solid and fluid solid contents, but also different geometrical configurations of the solid debris. As such the model should be able to treat flow transitions from granular type debris flows to hyperconcentrated mudflows (debris floods). The theoretical assumptions of the model should be clearly stated and differentiated from existing debris flow models currently applied in practice.

2. Our work with engineering practice suggests there is a strong need for models with a limited number of tunable parameters. The number of model free parameters should be as low as possible in order to simplify its application for practitioners.

3. Possess a robust computational solver, i.e., a stable numerical scheme that is able to give results in a reasonable time (max a few hours). As it is necessary to solve debris flow problems in narrow torrent geometries, the model should work at grid resolutions of 1mx1m.

4. The flow rheology should be based on experimental measurements of basal shear and normal forces, captured at the Swiss Illgraben test site. In addition the model should be applied to simulate well-documented case studies to demonstrate model performance and limitations. Model performance should be ascertained with regard to finding a narrow band of free parameters that can be used on the widest range of problems with varying initial and boundary conditions. That is, the ability of the model to be used as a predictive tool should be assessed.

1.3 Outline of the Thesis

This doctoral thesis is divided into six chapters:

Chapter 1 introduces the subject of debris flow modeling and motivates the work done in this thesis. How debris flow modeling will contribute to helping understand how a changing climate will influence debris flow activity is briefly outlined.

Chapter 2 documents the momentary state-of-the-art of debris flow modeling in order to compare and evaluate the model presented in this thesis with several models currently used in engineering practice.

Chapter 3 describes the debris flow model developed in this thesis. We define the phase and present the system of mass and momentum conservation equations adapted for a two-fluid two-layer debris flow model, including dilatancy. We compare the model to actual-scale debris flow density measurements from Illgraben.

Chapter 4 introduces the rheology and the erosion models used within the framework of the new debris flow model. An illustration of the consequence of adapted rheology is discussed using simulations of an actual debris flow event. The erosion model is calibrated using erosion field measurements obtained by drone flights.

In **Chapter 5**, we apply the model to three well-documented GLOF events, which exhibit a complex flowing behavior and are therefore challenging to simulate accurately. We discuss the forces and weaknesses of the model.

Chapter 6 concludes this doctoral thesis by summarizing the main findings and presenting an outlook for future research. It also includes a discussion of the relevance and implications of the presented results.

Chapter 2

Debris Flow Modeling

2.1 Overview

Physics-based debris flows science began in the former Soviet republics of Central Asia. These republics were confronted with immense debris flows (volumes greater that 1 million m^3) and began designing large deflecting and catching dams to mitigate debris flow run-out, Fig. 2.1. In fact, Soviet scientists performed the first large-scale field experiments in the 1960s by releasing dammed, muddy debris in mountain torrents. To model debris flow run-out, they employed primarily empirical, analytical models to estimate discharge and flow heights. Numerical debris flow models began to emerge in Europe and North America in the late 1980s. The first models employed depth-averaged, shallow water-type approaches, modeling the debris flow as a single-phase mixture of rocky debris and mud [48, 49, 50, 51]. Around 2010, two-phase models began to emerge to improve debris flow hazard mitigation [1, 3, 6].

In the following sections, we present an overview of single and two-phase modeling as well as the physical and the mechanical processes underlying the model equations. As it is impossible to summarize all debris flow models, we concentrate on four of the most well-known, two-phase/layer depth-averaged models presently in practical use. These are D-CLAW [1, 2], r.avaflow [6, 53], the model of Bouchet [4, 5, 41] and Titan2D [3, 48]. The presentation of the four models serves to highlight the different physical assumptions, underscoring the large difference in model design. Clearly, the list of models is not complete.

The debris flow models presented here possess solid physical and mathematical foundations and are implemented with robust numerical schemes. However, most have only been subjected to little testing or application to real scenarios. For instance, The *D-Claw* model has been compared to large-scale debris flow experiments [2]. However, these experiments are mainly performed on simple terrain topography. Only one actual debris flow event [54] has been back-computed and the results were comparable to one-phase model accuracy. The model of *Bouchut* was only compared to other debris flow models on simple terrain topography (ideal slope without roughness and a uniform slope angle). Only the *r.avaflow* [55, 56, 57, 58, 59, 60], and *Titan2D*, [61, 62, 63] model have been widely tested on real events with convincing results. However, often, to reproduce complex events, manual tuning of the parameters during a simulation is needed, [55, 56, 64].

The discussion of basic model assumptions helps to understand how we designed our model
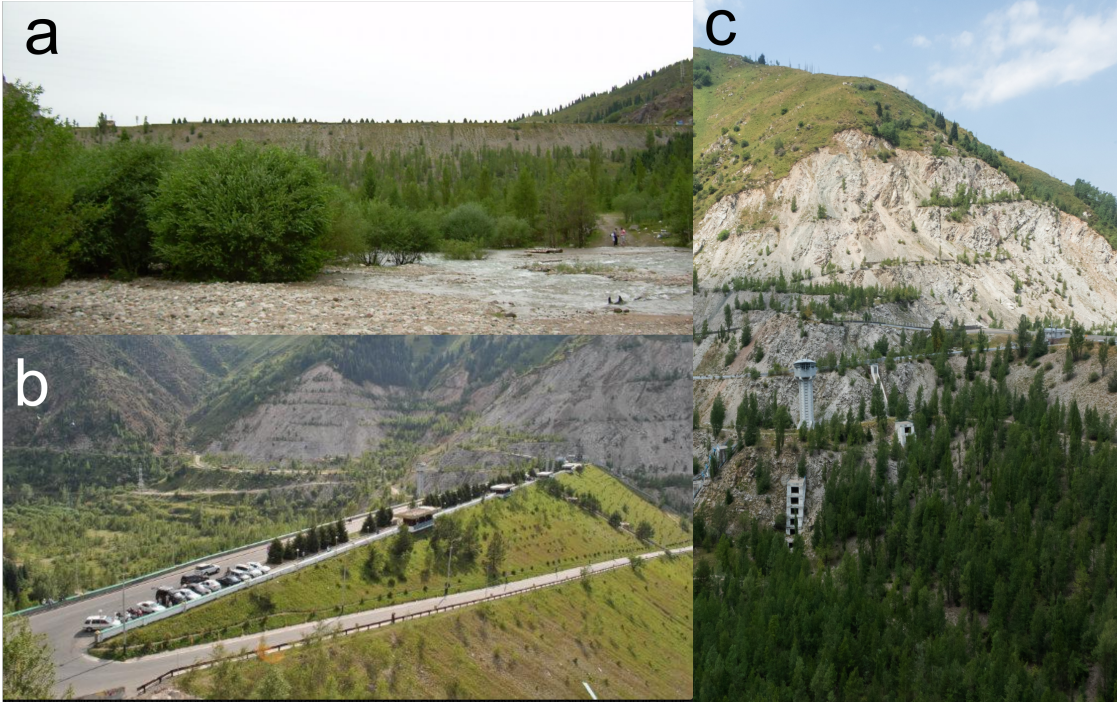
Figure 2.1: *The Meudeu mud flow control dam (southeast of Almaty, Kazakhstan), has been designed to protect the city of Almaty from devastating debris flows. The construction started in the middle of the sixties. a) and b): views from downstream ([52]) c) view from upstream (J. Münch).*

equations, providing physical reasons why we adopted a particular approach. All the models have features which we eventually implemented, but also other features which we discarded, primarily because they did resolve the problems of rheology, entrainment and flow regime transitions. We begin our discussion with an overview of the general, governing three-dimensional equations for debris flows.

2.2   General Governing Equations and Depth-averaging

Here we present the general governing equations for a three-dimensional, multi-phase debris flow model based on mixture theory. Presently, we make no assumptions concerning the physical components. The components (typically fluid/solid) are labeled using the subscript i; the associated density is given as ρ_i and flow velocity $\vec{v}_i$. If ϕ_i denotes the volume fraction of the i-th component. It can be written as,

$$\phi_i = \frac{V_i}{\sum_{i=1}^{n} V_i} = \frac{V_i}{V} \qquad \text{with} \qquad \sum_{i=1}^{n} \phi_i = 1. \tag{2.1}$$

where V represents the entire volume filled by the material and n denotes the number of components. According to [1, 2, 6, 65], the general mass balance equation for the i-th component in Cartesian coordinates is given by:

$$\frac{\partial}{\partial t}\left(\phi_i \rho_i\right) + \vec{\nabla} \cdot \left(\phi_i \rho_i \vec{v}_i\right) = E_i + Q_i, \tag{2.2}$$

with $\vec{\nabla} = (\partial/\partial_x, \partial/\partial_y, \partial/\partial_z)^T$ the divergence operator, E_i the i-th component erosion rate and Q_i the mass transfer rate between the i-th component and all the other ones. Similarly, the momentum balance equation of the i-th phase is:

$$\frac{\partial(\phi_i \rho_i \vec{v}_i)}{\partial t} + \vec{\nabla} \cdot (\phi_i \rho_i \vec{v}_i \otimes \vec{v}_i) = \vec{\nabla}(\phi_i p_i) - \vec{\nabla} \cdot (\phi_i \tau_i) + \phi_i \rho_i \vec{g} + \vec{P}_i \tag{2.3}$$

where $\otimes$ denotes the tensor product, $\vec{g}$ the gravitational acceleration, p_i the pressure, τ_i the shear stress tensor acting on the i-th component and $\vec{P}_i$ the total momentum transfer rate with the other components [1, 2, 6, 65].

To simplify the equations and reduce the computation time, we introduce the depth-averaged approximation. This reduces the three-dimensional model to a two-dimensional model. The depth-averaged approximation consists in replacing any physical value $\lambda(x, y, z)$ by its average over z, $\lambda^*(x, y)$,

$$\lambda^*(x, y) = \frac{1}{h} \int_0^h \lambda(x, y, z) \mathrm{d}z. \tag{2.4}$$

This approximation is valid if the flow depth h is negligible compared to the flow length L,

$$\frac{h}{L} \ll 1. \tag{2.5}$$

In the framework of debris flow, Eq. 2.5 is always satisfied. Most importantly the debris flow velocities, volumetric fluid fraction and densities are given by,

$$\vec{v}^*(x, y) = \frac{1}{h} \int_0^h \vec{v}(x, y, z) dz \qquad \text{and} \tag{2.6}$$

$$\phi^*(x, y) = \frac{1}{h} \int_0^h \phi(x, y, z) dz \qquad \text{and} \tag{2.7}$$

$$\rho^*(x, y) = \frac{1}{h} \int_0^h \rho(x, y, z) dz \tag{2.8}$$

The integration over z implies that the model will never be able to describe vertically varying physical values. For example, a uniform volumetric volume fraction along z is assumed for each component. This can be considered a disadvantage when trying to implement complex frictional rheologies. Another important aspect of depth-averaging is that the velocity profile is neglected. Only the mean material velocity can be computed. We assume that the velocity is homogeneously distributed from $z=0$ to $z=h$. Under the assumption that the shearing in the vertical direction (z) and the vertical acceleration are negligible with respect to gravity and vertical pressure gradient, Eq. 2.3 along z simplifies to :

$$\frac{\partial p}{\partial z} - \rho g = 0 \tag{2.9}$$

If we assume a uniform, atmospheric pressure at the flow surface, the solution to this equation is:

$$p - p_A = \rho g(h - z) \tag{2.10}$$

This assumption implies that the pressure is hydrostatic and that there are no slope perpen-

dicular accelerations other than gravity. Non-hydrostatic excess pore pressure can arise from the dilatant action of the solid matrix. The velocities are primarily valid for flat to moderately steep slopes. Depth-averaged approaches have many advantages over more computationally demanding three-dimensional approaches. One advantage is that they directly calculate the flow height h, which can be measured in field observation stations. In fact, a direct comparison to measurements can also be made to measure shear S and normal stresses N. That is, calculated field variables can be compared directly to measurements. In the following, we will attempt to exploit this advantage when developing debris flow rheologies. Finally, we note that the calculated velocities are always the internal velocities, not necessarily the propagation speed of the leading edge which can be captured from video recordings. Here, care must be taken when comparing depth-averaged velocities to measured leading edge speeds. Finally, the primary advantage of depth-averaged approaches is computational speed, especially for long run-out ($>$10km) debris flow events, for example GLOFs. Presently, GLOF calculations are not tractable at the full three-dimensional level. For readability purposes, all the physical values will be replaced from now on by their depth-averaged values without change in the notation (without the *). We do not present here general depth-average equations in x and y direction. Indeed, the results strongly depends on the hypothesis while integrating eq. 2.3.

Depth-averaging is an efficient approximation for reducing numerical modeling computation time. Depth-averaging essentially allows debris flow models to be applied in large-scale, regional analyses [66, 67, 68] or for long run-out events such as GLOFS [47, 54, 56, 58, 63, 69, 70]. The cost of depth-averaging is the loss of information concerning the vertical variation of the physical quantities, most importantly flow velocity and density. Clearly, depth-averaging leads to approximation errors of the conservation equations. Indeed, for a general non-linear mathematical function (i.e., with more than one varying parameter), the integration along z is generally all but impossible. Therefore, the procedure consisting of replacing the standard quantities with depth-averaged ones can be done up to an inevitable error. A mathematical quantification of the induced error is provided in [3].

2.3   One-phase Models

One-phase, depth-averaged models are widely applied in debris flow mitigation [38, 40, 48, 49, 71]. They operate on the basic assumption that the debris flow body consists of a solid-fluid mixture of constant density, and therefore singular rheology. A good example for the widespread use of a one-phase debris flow model is depicted in Fig. 2.2, which shows the worldwide distribution of the *RAMMS* model [50, 51], developed at the WSL Institute for Forest, Snow and Landscape Research in Switzerland.

By definition, a one-phase model treats the solid and the fluid components together (the indices in Eq. 2.2 and 2.3 disappear). This leads to a simple system of mass and momentum balance equations of the general form,

$$\frac{\partial h}{\partial t} + \vec{\nabla} \cdot (h\vec{v}) = E \tag{2.11}$$

and the momentum balance equation is

$$\frac{\partial (h\vec{v})}{\partial t} + \vec{\nabla} \cdot (h\vec{v} \otimes \vec{v} + \frac{gh^2}{2}I) = h\vec{g}_z - \vec{\tau}, \tag{2.12}$$

Figure 2.2: *The one-phase RAMMS debris flow model, [50, 51], has already been widely used and applied in many case studies. Each point on this map corresponds to a RAMMS license bought. The main users are Engineering offices, National, regional, and local authorities or Universities and research institutions.*

where E is the erosion rate and $\vec{\tau}$ is the depth-averaged shearing stress acting on the flow [40, 50] and I is the 2-dimensional unity matrix. Gravity is the first right-hand term of Eq. 2.12. Note the absence of a flow density, which disappears in the one-phase model equations.

One-phase model approaches differ in their treatment of the erosion rate E and shear stress $\vec{\tau}$ [38, 39, 40, 48, 49, 64, 71, 72, 73, 74]. Interestingly, several one-phase models [38, 39, 48, 49], do not consider erosion. This is clearly questionable, because the overall mass balance of a debris flow event is directly related to the bed erosion [50, 75, 76]. A primary quantity to predict in debris flow simulations is the flow height (to simulate channel outbreaks, bridge clearance or dam heights), which can be underestimated without erosion. However, the problem is circumvented in practice by modifying the initial conditions of the problem. Typically, one-phase debris flow simulations are started either using a dam-break approach, or by assuming a flow discharge. In both cases the initial height of the dam-break or discharge rate can be increased to account for any possible torrent erosion. This leads to higher calculated flow heights. Other models include erosion, for example the *RAMMS* model [40, 50]. Erosion models require additional free parameters to define the critical shear stress of the bed, the erosion rate and the maximum erosion depth [40, 50]. The erosion parameters are based on field measurements [75] and well-documented events, see Sec.2.6.4.

The primary problem of one-phase models (from the standpoint of practical application) is the definition of the shear stress $\vec{\tau}$, or flowing rheology. One-phase models are unable to track the

space-time evolution of the flow composition: the density is constant and uniform during the entire simulation. This problem is related to the erosion problem, as erosion and deposition processes transform the flow's internal solid-fluid composition, influencing the density and flow rheology. When using one-phase debris flow models, a wide range of friction values need to be applied to give plausible results, [64, 72, 73]. In order to be able to back compute complex events, like GLOFs, the users of one-phase models need to manually the friction parameters during a single simulation [47]. In fact, it is almost impossible to apply one-phase models in a torrent without historical information of torrent activity, including run-outs of extreme events. As stated in the introduction, it is this problem which is driving the development of two-phase models.

2.4   Two-phase/Two-fluid Debris Flow Models

In this section, we present four two-phase debris flow models. Three of the four two-phase models are in practical use by debris flow engineers today. These are Iverson's *D-Claw* model [1], *r.avaflow*, the model developed by Pudasaini and colleagues [6] and *Titan2D*, the model developed by Pitman and Le [3, 48]. The fourth model, initially developed for submarine flow, *Bouchut* model, is chosen because it is mathematically similar to the model developed in this thesis.

Clearly, more models can be found in the scientific literature; however, these models have not found their way into application. Our motivation is to supply the reader with an overview of the state-of-the-art of debris flow modeling from a practical perspective. Our comparison highlights the underlying physics and difference in model assumptions. Our basic goal is twofold. Firstly, we would like to show that large physical differences exist between models, and further, how these differences affect engineering practice when applying modeling techniques to debris flow mitigation problems. Secondly, we provide the reader with the necessary background to evaluate our model development, providing the necessary information and reasons for specific mathematical and physical formulations.

The four models are divided into two separate classes. The first class of debris flow model separates the solid and fluid phases, stating mass and momentum equations for each phase. The two most well-known models of this type are *D-Claw* and *r.avaflow*. These models can be classified as "two-phase" or "two-component" models because they adopt the conventional approach of separating the solid and fluid phases. (In the following the subscript s refers to the solid phase and f to the fluid.) On first inspection, the natural separation between the fluid and solid appears logical and intuitive. The mathematical description is straightforward and tractable. However, as we shall show it leads to problems concerning the solid-fluid interactions, which couple the solid-fluid momentum equations. These interactions are difficult to define and are not experimentally accessible. This leads to problems defining model parameters. Strong interactions between phases, for example during entrainment of solid debris, or de-watering, can lead to numerical instabilities because they physically represent sudden changes in momentum.

The second class of debris flow models can be considered "two-layer" or "two-fluid" models. Here, the approach is to keep a mixture layer of solid and fluid debris and then add an additional entirely fluid layer. This approach hinders the separation of the model equations into two separate solid and fluid phases (despite the fact *Bouchut* model and *Titan2D* do mathematically separate the components between the solid and the fluid). Such models contain a mixed layer of flowing water-

saturated debris and an entirely fluid layer. Models of this type are *Titan2D* and *Boutchut*. If the fluid layer disappears, the models can be considered similar to one-phase models. The advantage of two-fluid models is that they can simplify the mass and momentum exchanges between layers. Because the layers are not mixed, as in the two-phase models, but geometrically positioned one on top of the other, they can treat flow stratification problems, such as de-watering. However, their derivation and mathematical formulation are less natural, often requiring ad-hoc assumptions regarding the layer interactions and the introduction of pseudo-physical variables to solve the mass and momentum conservation equations.
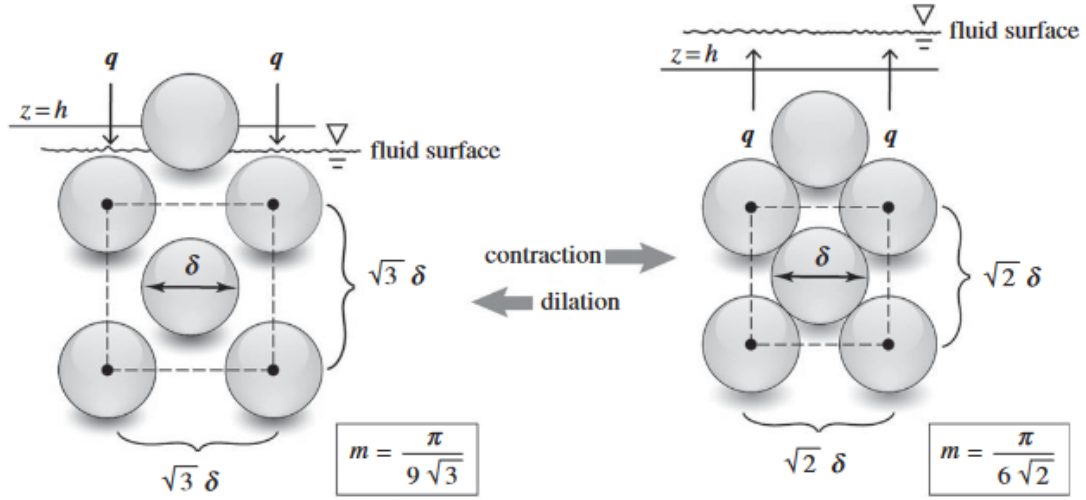

Figure 2.3: *Layer definition in the D-Claw model [1, 2]. The phases are divided between the solid (gray circles), assumed to be spherical particles, and the fluid, which fills the interstitial space in between the solid particles. The effects of dilatancy, Sec.2.6.2, are visible, through the spatial evolution of the solid matrix. A flux of fluid material, **q**, through the virtual free surface at $z = h$ accompanies changes in the volumetric solid concentration ϕ_s (noted m on the figure) caused by dilation or contraction. The original picture can be found in [1].*

2.4.1 Two-phase *D-Claw* Model

The depth-averaged *D-Claw* model, introduced by Iverson [1, 2] in 2014, divides the debris flow body into solid and fluid phases, see Fig.2.3. It consists of four partial differential equations that govern the mass and momentum balances:

$$\frac{\partial}{\partial t}(h\phi_s) + \vec{\nabla} \cdot (h\phi_s\vec{v}) = -\frac{\rho_f}{\rho}D\phi_s \,, \tag{2.13}$$

$$\frac{\partial}{\partial t}(h\phi_f) + \vec{\nabla} \cdot (h\phi_f\vec{v}) = \frac{\rho_s}{\rho}D\phi_s \,, \tag{2.14}$$

$$\frac{\partial}{\partial t}(h\vec{v}) + \vec{\nabla} \cdot \left(\vec{v} \otimes \vec{v} + \kappa\vec{g}_z h^2 + \frac{h(1 - \kappa p_b)}{\rho}\right) = h\vec{g}_z + \vec{v}D\frac{\rho - \rho_f}{\rho} - \frac{\vec{\tau}_s + \vec{\tau}_f}{\rho} \,, \tag{2.15}$$

$$\frac{\partial}{\partial t}p_b + \vec{v} \cdot \vec{\nabla}(p_b) + \rho g_z \Lambda h \vec{\nabla} \cdot \vec{v} = \zeta D - \frac{3}{\chi h}\|\vec{v}\|\tan(\psi), \tag{2.16}$$

where $\vec{g} = (g_x, g_y)^T$. g_x, g_y and g_z are the projection of the gravitational acceleration along x, y and z, $\vec{\tau}_s$, $\vec{\tau}_f$ are the basal shear stresses of solid and fluid respectively (for more detail, see Sec.2.6.3),

13

D represents the dilatancy effects (for more detail, see Sec.2.6.2), p_b is the basal fluid pressure, and κ (lateral pressure coefficient), ψ (granular dilatancy angle), and χ (debris elastic compressibility) are free model parameters.

For notational convenience, ξ and ζ are introduced and can be expressed as

$$\Lambda = \frac{\rho_f + 3\rho}{4\rho}, \tag{2.17}$$

$$\zeta = \frac{3}{2\chi h} + \frac{g_z \rho_f(\rho - \rho_f)}{4\rho}. \tag{2.18}$$

Finally, ρ and $\vec{v}$ are the average flow density and velocity,

$$\rho = \rho_s \phi_s + \rho_f \phi_f, \tag{2.19}$$

$$\vec{v} = \frac{\rho_s \phi_s \vec{v}_s + \rho_f \phi_f \vec{v}_f}{\rho}. \tag{2.20}$$

The system of differential equations (Eqs. 2.13 - 2.16), contains only one (vector) momentum conservation equation (Eq. 2.15) instead of the expected two (one for each phase solid and fluid). Instead of computing the solid and fluid velocities independently, Iverson computes an average flow velocity Eq. 2.20, avoiding the problem of the solid-fluid interaction. To simplify the model, Iverson invokes the hypothesis that the average velocity of the debris flow is controlled essentially by the velocity of the solid phase, *i.e.* $\vec{v} \approx \vec{v}_s$. This approximation, combined with eqs. 2.19 and 2.20 imply that the difference between the solid and fluid velocities are negligible with respect to the mean flow velocity: $\|\vec{v}_s - \vec{v}_f\| \ll \|\vec{v}\|$. With this assumption the *D-Claw* model is no longer a full two-phase model, but rather a reduced, or pseudo two-phase model.

The fluid velocity is computed from the solid one using a Darcy-like approximation,

$$\phi_f(\vec{v}_f - \vec{v}_s) = \frac{k}{\nu}\vec{\nabla}(p_e), \tag{2.21}$$

where k (hydraulic permeability) and ν (pore fluid viscosity) are two free parameters and p_e is the excess pore pressure, i.e. the deviation from the hydrostatic pressure, p_h. The basal fluid pressure p_b is the sum of the hydrostatic and excess pressure,

$$p_b = p_h(z=0) + p_e(z=0) = \rho_f gh + p_e(z=0). \tag{2.22}$$

One of the unique features of this model is to use a depth-averaged equation, derived by a dimensional analysis, to compute the basal pore fluid pressure p_b, Eq. 2.16. In principle, this procedure permits the computation of the space-time evolution of the pore fluid pressure in the flow. Interestingly, the authors find that the excess pore pressure is linked to the dilatant action of the solid matrix by the equation

$$D = -\frac{2k}{h\nu}p_e. \tag{2.23}$$

Therefore, dilatation and collapse (compaction) of the solid debris induce a negative ($p_b < p_h$) and a positive ($p_b > p_h$) deviation from the hydrostatic pressure, respectively. Moreover, the pressure at the base of the debris flow *decreases* with a dilating action of the solid matrix, and *increases* with a collapse of the solid matrix. The additional equation introduced by Iverson can therefore

be considered a "dilatancy" equation, but expressed in terms of the excess pore pressure p_e. The inclusion of dilatancy is one of the attractive features of the Iverson model, making it a general, granular theory based debris flow model.

2.4.2   Two-phase *r.avaflow* Model

Similar to the *D-Claw* model, the depth-averaged *r.avaflow* model, developed by Pudasaini and colleagues [6], divides the flowing debris into solid and fluid parts. It is therefore classified as a two-phase model. The mass equations are similar to the mass equations of the *D-Claw* model,

$$\frac{\partial}{\partial t}(h\phi_s) \quad +\vec{\nabla}\cdot(h\phi_s\vec{v}_s) = E_s, \tag{2.24}$$

$$\frac{\partial}{\partial t}(h\phi_f) \quad +\vec{\nabla}\cdot(h\phi_f\vec{v}_f) = E_f. \tag{2.25}$$

The right-hand side terms, E_s and E_f, represent the solid and fluid erosion rates, respectively. In the original model equations [6], the erosion processes are not considered, but the authors developed an extension of the model [53] taking erosion into consideration (see Sec.2.6.4 for more details).

However, the *r.avaflow* model quickly diverges from *D-Claw* model because the full set of momentum balance equations are solved to predict the solid/fluid flow velocities in the slope-parallel directions. Unlike *D-Claw*, no assumptions are made to reduce the number of momentum equations. As an example of a momentum equation, we present the solid-phase equation in the x-direction (the complete system of depth-averaged momentum equations is not presented here, as they are presented in full in [6]):

$$\frac{\partial}{\partial t}\left[\phi_s h\left(v_{x,s} - rC(v_{x,f} - v_{x,s})\right)\right] + \frac{\partial}{\partial x}\left[\phi_s h\left(u_{x,s}^2 - rC(v_{x,f} - v_{x,s}) + \omega_x\frac{h}{2}\right)\right] +$$
$$\frac{\partial}{\partial y}\left[\phi_s h\left(v_{x,s}v_{y,s} - rC(v_{x,f}v_{y,f} - v_{x,y}v_{y,s})\right)\right] = \phi_s\left[g_x - \frac{v_{x,s}}{\|\vec{v}_s\|}(r-1)g_z\tan\phi - \epsilon(r-1)g_z\frac{\partial b}{\partial x}\right] +$$
$$\epsilon\phi_s rg_z\frac{\partial}{\partial x}(h+b) + C_{DG}(v_{x,f} - v_{x,s})\|\vec{v}_f - \vec{v}_s\|^{j-1}, \tag{2.26}$$

in which $\omega_x = \epsilon\kappa_x(r-1)g_z$, $r = \rho_f/\rho_s$, $C = (1+2\phi_s)/(2\phi_f)$, κ_x is the lateral pressure coefficient (in direction x), $\epsilon = H/L$ is the aspect ratio, C_{DG} is the generalized drag coefficient. The superscript $j = 1, 2$ is used to select between laminar (j=1) or turbulent (j=2) flows, indicating that the user must select the flow regime *a priori*. The parameter b represents the bottom topography.

As demonstrated above, the coupled momentum conservation equations are rather complex and dominated by momentum exchanges (both laminar and turbulent). The absence of a Darcy-like approximation requires introducing complex interactions between the solid and the fluid phases in order to compute the interfacial momentum transfer. It includes, for instance, viscous drag, related to the relative velocity between the two phases; turbulent drag, related to the relative velocity square between the two phases. Inertial effects are included by introducing the so-called *virtual mass concept* that accounts for the relative acceleration between the two phases, see Sec.2.6.3 for more details. As these interactions are poorly understood and challenging to implement in a macroscopic description of a granular flow, use of the model requires defining many free parameters (around fifteen). Some of these parameters, such as the solid or the fluid densities, can be well-

estimated by users, while others possess broad confidence intervals concerning their exact values (e.g. the virtual mass coefficient). Even if a careful choice of all these parameters can allow back computing past events with high accuracy, the large uncertainties concerning their exact value make the model difficult and hazardous for practitioners to apply for predictions.

A primary difference between the *r.avaflow* and *D-Claw* models is the absence of a method in *r.avaflow* to account for the solid matrix dilatant action. *D-Claw* accounts for granular dilatations by increasing or decreasing the basal pressure via the excess pore pressures. In fact, the *r.avaflow* model does not consider excess pore pressures at all. In *r.avaflow* the solid and fluid densities are constant; the bulk flow density is subsequently given by the volumetric fractions of solid and fluid. The basal pressure is defined entirely by the hydrostatic pressure alone.

2.4.3   Two-fluid *Bouchut* Model

Bouchut and al. have introduced a two-fluid, two-layer model to simulate granular submarine flows [4, 5]. The basic idea behind the model formulation is to separate the flow into two layers. The bottom layer (the layer closest to the running surface, the ocean floor) is a mixed layer consisting of both solid material and interstitial fluid, see Fig. 2.4. The upper layer (the layer on top of the bottom layer, the ocean) is a pure fluid layer, containing no solid debris. This general approach can be classified as a two-fluid, or two-layer approach, first introduced by [77]. The first fluid is the interstitial fluid (which we term the bonded fluid) and the second fluid is the debris-free ambient fluid (which we term the free fluid). Clearly, the approach of Bouchut has strong similarities to our model design, but with clear differences, such as the height of the ambient fluid, leading to strong differences in the magnitude of the hydrostatic pressure and therefore the interaction with the mixed flow layer.
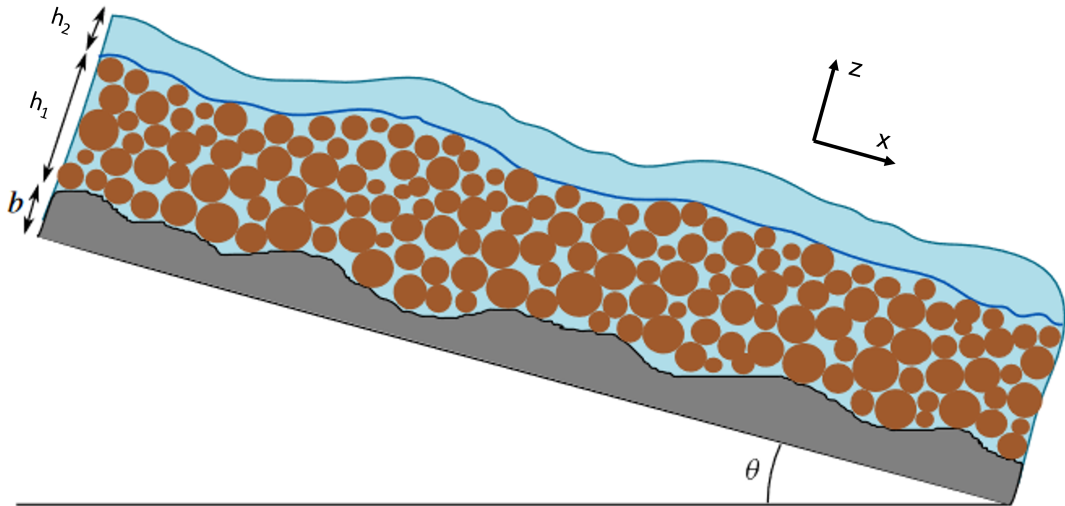

Figure 2.4: *Layer definition in the Bouchut debris flow model [4, 5]. The first layer, whose height is h_1, is composed of a mixture of solid and interstitial fluid. The second layer, whose height is h_2, is entirely fluid. b represents the bottom topography and θ is the general slope angle. The original figure is found in [5].*

The mass and momentum equations of the Bouchet submarine flow model [4] are

$$\frac{\partial}{\partial t}(\phi_s h_1) + \vec{\nabla} \cdot (\phi_s h_1 \vec{v}_s) = 0, \tag{2.27}$$

$$\frac{\partial}{\partial t}(h_1 \phi_f) + \vec{\nabla} \cdot (h_1 \phi_f \vec{v}_f) = -Q_f, \tag{2.28}$$

$$\frac{\partial}{\partial t}(h_2) + \vec{\nabla} \cdot (h_2 \vec{v}_f) = Q_f, \tag{2.29}$$

$$\frac{\partial}{\partial t}(h_s \vec{v}_s + \vec{\nabla} \cdot (h_s \vec{v}_s \otimes \vec{v}_s) = \frac{\rho_s - \rho_f}{2\rho_s} g_c \left(\vec{\nabla} \left(\phi_s h_1^2 \right) - 2h_s \vec{\nabla} \hat{b} \right) + \frac{\vec{\tau}_{sf}}{\rho_s} - \frac{\vec{\tau}_s}{\rho_s} \frac{\vec{v}_s}{\|\vec{v}_s\|}, \tag{2.30}$$

$$\frac{\partial}{\partial t}(\phi_f h_1 \vec{v}_f) + \vec{\nabla} \cdot (\phi_f h_1 \vec{v}_f \otimes \vec{v}_f) = -\frac{1}{2} Q_f \vec{v}_f - \frac{\vec{\tau}_{sf}}{\rho_f}. \tag{2.31}$$

The model consists of five differential equations. As three flow components are defined, three mass conservation equations are needed to describe fully the system. Two mass balance equations are needed for the mixture layer (height h_1) and one equation is needed for the upper fluid layer (height h_2). The mass in the mixture layer is defined by the solid and fluid volumetric contents, ϕ_s and ϕ_f, respectively. For example, the amount of fluid in the mixture layer is $h_{f,1} = \phi_f h_1$ and the solid amount is $h_s = \phi_s h_1$, see Fig. 2.4. The fact that two-layer models require three mass conservation equations (instead of two, as in the two-phase models) is a general feature of two-fluid models. The right-hand side of the fluid equations consists of the term Q_f, which is the fluid exchange rate between the two layers, due to the dilatant action (expansion or contraction) of the solid matrix. It is defined as positive when interstitial fluid is removed from the mixture and becomes part of the free fluid (that is, during a contraction of the solid matrix). How dilatancy is modeled and how Q_f is mathematically quantified will be discussed in Sec.2.6.2.

The model contains two momentum equations. The first equation defines the momentum of the solid in the mixture layer; the second equation defines the momentum of the fluid in the mixture layer. The momentum of the upper layer is not considered, and therefore this layer can be considered as a passive, motionless layer. It represents the lake, sea, or ocean in which the submarine flow does not influence global motion. This assumption is specific for submarine flows, and cannot be generally adopted for debris flows.

Of interest is the treatment of the total momentum in the mixture layer, as it contains interaction terms. The solid matrix is driven by gravity, $g_c = g \cos(\theta)$ and includes buoyant effects (difference between solid and fluid densities). The internal friction between solid particles and the running surface is given by S_s. The solid-fluid interaction is introduced via the term $\vec{\tau}_{sf}$, which represents the shear stress between the solid-fluid components in the first layer. It is given by

$$\vec{\tau}_{sf} = \phi_f h_1 \vec{\nabla} p_e + \eta h_1 (\vec{v}_f - \vec{v}_s), \tag{2.32}$$

with p_e the excess pore pressure, see Eq. 2.22 and η a free parameter governing the viscous shearing force magnitude between the solid and the fluid. Note that fluid friction is absent in Eq. 2.31 because the fluid is assumed to be inviscid (S_f=0).

Of particular interest in the model of Bouchet is mass (and therefore momentum) exchange between the interstitial fluid (mixture layer) and passive ambient layer. In this sense, the model has strong similarities with the Iverson approach as dilatancy of the granular solid plays an important role in controlling the motion of the solid phase, see Sec. 2.6.2 for more details.

In a later paper, the authors derived a general debris flow model starting from the submarine model [5]. However, they postulated that the fluid in the first and second layers flow at the same velocity; that is, the bonded, interstitial fluid has the same velocity as the unbonded, free fluid. With this assumption, the mass and momentum balance equations are valid for the entire fluid (interstitial + second layer). Hence, the mass and momentum fluid exchanges vanish, and dilatancy no longer impacts the equations. The debris flow model uses a Darcy-like approximation to reduce the model complexity and to compute the fluid velocity using a similar equation as in the *D-Claw* model, Eq. 2.21.

Finally, a multi-layer model is introduced in [41]. It contains N mixture layers and one additional fluid layer flowing on top. Each mixture layers contains dilatancy of the solid matrix and allows vertical variations of the system's physical parameters (e.g. solid fraction, velocity, fluid pressure). This method was developed to improve the accuracy of the results, but this, at the expense of the computational time.

2.4.4 Two-fluid *Titan2D* Model

A two-fluid approach was also introduced into the well-known one-phase *Titan2D* [48] model toolbox to include the effects of an interstitial fluid phase when modeling (soil, rock) avalanches and debris flows [3]. The mass conservation equations are therefore similar to Eqs. 2.27-2.29 of the *Bouchut* model,

$$\frac{\partial}{\partial t}(\phi_s h_1) + \vec{\nabla} \cdot (\phi_s h_1 \vec{v}_s) = 0, \tag{2.33}$$

$$\frac{\partial}{\partial t}(h_1 \phi_f) + \vec{\nabla} \cdot (h_1 \phi_f \vec{v}_f) = 0, \tag{2.34}$$

$$\frac{\partial}{\partial t}(h_2) + \vec{\nabla} \cdot (h_2 \vec{v}_f) = 0, \tag{2.35}$$

The important difference to the Bouchut model, however, is the absence of a fluid exchange between the two fluid layers because the two-fluid *Titan2D* model does not consider dilatancy (or entrainment). The right-hand sides of the mass balance equations are all zero. With this assumption, the momentum exchanges between the two layers can only occur through the solid-fluid interactions (see Sec. 2.6.3). To exemplify the momentum equations, we present the momentum balance equation of the solid phase in the mixture layer in the x-direction,

$$\frac{\partial}{\partial t}(\phi_s h v_{x,s}) + \frac{\partial}{\partial x}(\phi_s h v_{x,s}^2) + \frac{\partial}{\partial y}(\phi_s h v_{x,s} v_{y,s}) = \frac{1}{2}\epsilon(1-r)\frac{\partial}{\partial x}\left(\alpha_{xx} h^2 \phi_s g_z\right)$$

$$+ \frac{1}{2}\epsilon(1-r)\frac{\partial}{\partial y}\left(\alpha_{xy} h^2 \phi_s g_z\right) + \frac{1}{2}\epsilon r \phi_s \frac{\partial}{\partial x}\left(h^2 g_z\right) + (1-r)(\epsilon\alpha_{xx}\frac{\partial}{\partial x}b + \epsilon\alpha_{xy}\frac{\partial}{\partial y}b - \alpha_{xz})h\phi_s g_z$$

$$+ \epsilon r h \phi_s g_z \frac{\partial}{\partial x}b + (1-r)\frac{h(1-\phi_s)\phi_s}{v_T(1-\phi_s)^s}(v_{x,f} - v_{x,s})h\phi_s g_x \tag{2.36}$$

where $r = \rho_f/\rho_s$, ϵ is the aspect ratio, α_{**} the lateral pressure coefficients (In *D-Claw*, they treat it as a scalar, in *r.avaflow* it is a vector and here as a tensor), v_T is the terminal velocity of a typical solid particle falling in the fluid under gravity and s is related to the Reynolds number of the flow. b represents the bottom topography.

As in the *D-Claw* and *Bouchut* models, the computation of the fluid velocity is based on a

Darcy-like approximation. Indeed, it is assumed that fluid inertia effects are small. It leads to a simple ordinary equation for the fluid velocity, similar to Eq. 2.21:

$$(1-r)\frac{h\phi_s}{v_T(1-\phi_s)^s}(\vec{v}_s - \vec{v}_f) = -\frac{1}{2}\epsilon\vec{\nabla}h^2 g_z + h\vec{g}. \tag{2.37}$$

2.5   Model Comparison

We end our overview and assessment of multi-component debris flow models by tabulating the main characteristics of each model. For comparison we also include the model developed within this dissertation. We find that there are *five* model characteristics that can be used to differentiate between approaches. These are:

1. The strict division of debris material into solid and fluid parts (two-phase models) or the division of the debris flow into mixed layers with fluid behavior divided into interstitial fluid and free fluid (two-fluid/two-layer models).

2. The treatment of the fluid momentum. Either the fluid motion is treated relative to the solid velocity using a Darcy-type approximation, or, the fluid is considered to be entirely independent of the solid, albeit with momentum mass and exchanges with the solid phase. All models treat buoyancy effects.

3. The assumption of dilatant actions in the granular, solid matrix of the flowing debris material. These actions can change the pore pressure of the saturated debris. Therefore, debris flow models with dilatancy are often accompanied by excess pore pressures.

4. How shearing, that is flow friction, is formulated within the two-phase/two-layer model. This characteristic can be subdivided into three sub-parts: the friction of the *solid* phase, the friction of the *fluid* phase and the *shearing interactions* between the solid and fluid parts.

5. The inclusion of solid/fluid entrainment or sediment erosion in the governing mass and momentum balances. A detailed discussion of this topic is outside the scope of this thesis.

We did not include all debris flow models in our review. However, we regard the strong variation in model assumptions within the four models we analyzed as exemplary of the debris flow problem and the state of debris flow science, especially with regard to depth-averaged approaches. Within our model selection, it appears that the minimum number of free parameters to be around six, while the maximum number is approximately 15 (without erosion taken into account). This is summarized in Tab. 2.1.

2.6   Physical Processes

2.6.1   Fluid Momentum and Darcy Approximation

The division of debris flow models into two-phase and two-fluid categories is centered around the basic problem of how to mathematically treat the momentum associated with the fluid phase.

In two-phase models, the fluid is treated as a physical component independent of the solid fraction. The fluid phase exists either as pore fluid, bonded to the solid matrix or as free fluid;

	Two-phase models		Two-fluid models		
Model type					
Model name	*D-Claw*	*r.avaflow*	*Titan2D*	*Bouchut*	*Meyrat*
First phase/layer	Solid	Solid	Mixture	Mixture	Mixture
Second phase/layer	Fluid	Fluid	Fluid	Fluid	Fluid
Fluid momentum conservation equations [1]	No	Yes	No	No	Yes
Erosion	No	Yes	No	No	Yes
Dilatancy	Yes	No	No	Yes	Yes
Fluid exchange	Yes	No	No	No/Yes[2]	Yes
Buoyancy	Yes	Yes	Yes	Yes	Yes
Excess pore fluid pressure	Yes	No	No	Yes	No
Solid friction	Coulomb with effective stress and dilatancy	Standard Coulomb	Standard Coulomb	Coulomb with effective stress and dilatancy	1.Coulomb with effective stress and dilatancy 2. Turbulent drag $\propto \|\vec{v}_s\|^2$
Fluid friction	Viscous drag $\propto \|\vec{v}_f\|$	Viscous drag $\propto \|\vec{v}_f\|$	Inviscid	Viscous drag $\propto \|\vec{v}_f\|$	Turbulent drag $\propto \|\vec{v}_f\|^2$
Solid-fluid interaction	Absent	$\propto \vec{v}_f - \vec{v}_s$ $\propto \|\vec{v}_f - \vec{v}_s\|^2$ $\propto \frac{d}{dt}\|\vec{v}_f - \vec{v}_s\|$	$\propto \|\vec{v}_f - \vec{v}_s\|$	$\propto \vec{v}_f - \vec{v}_s$	Fluid bonded to solid
No. of free parameters [3]	7	$\approx 15 \mid > 20$	≈ 8	≈ 6	6 | 11

Table 2.1: Overview of two-phase/two-fluid debris flow models. [1] "No" implies the model uses a Darcy-like approximation to compute the fluid velocity; "Yes" indicates a separate momentum equation for the fluid phase. [2] In the submarine model, they consider fluid mass and momentum exchanges. However, in the debris flow model, the exchanges vanish, as they treat both fluid components (interstitial and second layer) together. [3] The number of free parameters is quite difficult to state precisely. We counted the total number of parameters included in both the rheological as well as the erosion sub-models. The first number in the column represents the number of rheological parameters; the second number includes the erosion model parameters.

that is, as a fluid stream unhindered by interactions with the solid phase. A single mass equation contains both fluids, both bonded and free. Bulk friction coefficients are posed (see below) that contain drag terms that unify the frictional interactions such that they can be treated in a single fluid momentum equation. This general approach is adopted in the *r.avaflow* model.

In the three other models, i.e. *D.claw*, *titan2D* and *Bouchut* model, a Darcy-like approximation is used to replace the fluid momentum equation. The velocity of the fluid phase is defined relative to the velocity of the solid matrix. This assumption is valid in the case of a standard debris flow characterized by a high solid fraction. In this case, the solid phase governs the motions and flow dynamics. However, it is not realistic for a muddy or low solid-concentrated flow. The simplification cannot be applied to model dewatering or phase separations processes in which the solid stops and the fluid is washed-out of the solid matrix. The "freed" fluid phase is no longer represented by an independent fluid phase momentum equation, with drag terms representing basal frictional processes of free flowing muddy stream. Two-phase models that employ Darcy-like approximation will most probably fail to simulate flow transitions and phase separations encountered in long run-out debris flows or GLOFs.

Two-fluid models operate under the assumption that the physical behavior of the interstitial (bonded pore-fluid) and free fluid are fundamentally different. As such, they cannot be lumped into a single fluid momentum equation. The consequence of this assumption is that three mass conservation equations are required to track the debris flow mass, the interstitial fluid, the free fluid and the solid debris. Given that a free fluid stream can exist, the Darcy-approximation becomes a valuable modeling assumption as it tracks the velocity of the pore-fluid relative to the solid. This could play an important role when developing debris flow models that attempt to model a partially saturated solid matrix, or the entrainment of partially saturated debris.

2.6.2 Dilatancy and Solid/Fluid Phase Exchanges

Dilatancy is the property of a granular material to increase or decrease its physical volume under a shearing action. A well-known display of dilatancy in the real world is walking on the beach and noting that sand is drying under your feet. This is due to the volume expansion in the sand, which increases the void space into which the water can sink, see Fig. 2.5.

Figure 2.5: *When walking on a beach, the sand dries around the foot. This effect is caused by granular dilatancy in the sand.*

The notion of granular dilatancy was introduced in 1885 by Reynolds in a pioneering paper [78]. Since then, many different stress-dilatancy theories have been developed, either on energy-based concepts, [79,80], or mechanical constraints due to internal reorganization of grain geometry [81,82].

In a debris flow, dilatancy is an essential feature of the flow dynamics due to the shearing of the solid fraction ϕ_s [83, 84, 85, 86]. Among the two-phase/layer models presented above, only the *D-Claw* and *Bouchut* models consider dilatancy (a one-phase model can only include dilatancy via empirical relationships). Both these models link the divergence of the solid velocity and the solid volume fraction through [87],

$$\vec{\nabla} \cdot \vec{v}_s = -\frac{1}{\phi_s} \frac{d\phi_s}{dt} = -\frac{1}{\phi_s} \frac{\partial\phi_s}{\partial\gamma} \frac{d\gamma}{dt} = \dot{\gamma}\tan(\psi), \tag{2.38}$$

with γ the shear strain and ψ the dilatancy angle, which is defined as [88]:

$$\tan(\psi) = -\frac{1}{\phi_s} \frac{\partial\phi_s}{\partial\gamma} \ . \tag{2.39}$$

Afterwards, following the work of [89,90] a linear relation between $\tan(\psi)$ and ϕ_s is assumed. We have

$$\vec{\nabla} \cdot \vec{v}_s = \dot{\gamma}\tan(\psi) = \dot{\gamma}K(\phi_s - \phi_{s,eq}), \tag{2.40}$$

where K is a proportionality parameter (generally close to 1) and $\phi_{s,eq}$ is an equilibrium configuration that depends on the system's physical parameters and therefore evolves during the flow. These two equations allow the computation of the dilatant space-time evolution of the solid matrix.

In *D-Claw*, Iverson additionally assumes that the evolution of ϕ_s is not only due to the shear stress but also due to mean effective normal stress σ_e. This assumption implies an enlargement or reduction of the particle's void space due to bulk compressibility of the mixture. For more details, the reader is referred to [1]. In other models, for example in the *Bouchut* model, this effect is not explicitly taken into account. However, it is possible to consider it through the solid-fluid fluxes, as in the second term on the right-hand side of Eq. 2.42. As the solid particles dilate or collapse, fluid is squeezed-out or sucked in the solid matrix. Importantly, the mass and momentum exchanges are associated with this dilatancy, see terms with D in Eqs. 2.13-2.16, and with Q_f in Eqs. 2.28 and 2.29. Dilatancy is therefore the physical process that links volumetric solid/fluid fraction content and finally the flow rheology, and therefore the flow regime.

By defining the dilatancy D as

$$D \equiv \int_0^h \vec{\nabla} \cdot \vec{v}_s dz, \tag{2.41}$$

the right-hand terms in Eqs. 2.13 and 2.14 act as a sink of solid material $\frac{\rho_f}{\rho}D\phi_s$ and simultaneously as a source $\frac{\rho_s}{\rho}D\phi_s$ of fluid. Here we assume that the space left by the solid dilatation is *instantaneously* filled by fluid; moreover, there are no cavitation effects. Eqs. 2.13 and 2.14 automatically fulfill the requirement of total mass conservation – but not total volume conservation, as the flow height evolves with dilatancy.

In [4,5] a similar approach is followed. The fluid source and sink terms on the right-hand side of the mass conservation equations Q_f can be expressed as,

$$Q_f = -D - \vec{\nabla} \cdot (\phi_f h_1 (\vec{v}_f - \vec{v}_s)), \tag{2.42}$$

with D given by Eq. 2.41 as before. However, in this model, D, and therefore the dilatancy, is defined only in the first mixture layer. Changing the integration bounds from h to h_1 in Eq. 2.41, we find the first term on the right-hand side of Eq. 2.42, which comes from the dilatancy of the solid, while the second term comes from the difference of the fluid and solid fluxes in the first layer. In a two-fluid mixture model a relative motion between the center of mass of the solid and fluid phases can occur. Indeed, in a dilatant equilibrium, the center of mass of both solid and fluid components always coincides. Therefore, a relative movement between them induces fluid exchanges between the two layers because all the void space between the particles is, by definition, filled by fluid, i.e., $\phi_s + \phi_f = 1$.

Finally, granular dilatancy is present in the solid mass conservation equation for the *D-Claw* model, Eq. 2.13, but not in the *Bouchut* model, Eq. 2.27. Indeed, in the *Bouchut* model, the mass conservation equations are computed with respect to the first phase height, which moves according to the solid particle's dilatation actions. Therefore, the solid mass remains unchanged even if the first layer height evolves under dilatancy. However, in *D-Claw* model, the mass conservation equations are computed with respect to a 'virtual free surface', which does not follow the movement of the dilatant solid, see Fig. 2.3. Consequently, the solid mass is not conserved beneath this virtual free surface.

2.6.3 Rheology of Two-phase/Two-fluid Debris Flows

It is well-known that debris flow motion is complex and cannot be simulated by a single phase, constant and uniform rheological model [7]. The state-of-the art is to divide rheological behavior into solid and the fluid parts, that cannot be considered independently from the internal flow composition (solid/fluid fractions). A significant problem in debris flow science is that almost no shear stress measurements have been performed on real debris flows, and then only in specific field conditions. Presently, the separation of solid-fluid friction and the internal solid-fluid interactions are based on empirical relationships.

For two-phase/layer debris flow models, the rheology is subdivided into three parts: the solid friction $\vec{\tau}_s$, the fluid friction $\vec{\tau}_f$ and the internal solid-fluid friction $\vec{\tau}_{sf}$. These are considered separately in the sections below.

Solid friction

The four models presented in sections 2.4 employ a Coulomb friction law to treat the solid phase rheology. For *r.avaflow* and the model of *Titan2D*, the simplest form of the Coulomb friction model is used,

$$\vec{\tau}_s = \tan(\varphi)N\hat{e}_{v_s}, \tag{2.43}$$

φ is the solid friction angle of the material, N is the normal stress and $\hat{e}_{v_s} = \frac{\vec{v_s}}{\|\vec{v_s}\|}$ is a unitary vector pointing in the direction of flow.

Iverson adopts a similar approach. However, following the work of Terzaghi [91], he employs an effective stress concept [91]. In this approach the pore-fluid pressure is subtracted from the normal stress. The effective stress model of Iverson also includes the effect of the dilatation of the solid

content by adding the dilatancy angle to the internal friction angle,

$$\vec{\tau}_s = \tan(\varphi + \psi)(N - p_b)\hat{e}_{v_s}, \tag{2.44}$$

according to [82, 92, 93, 94]. Therefore, an enlargement of the solid matrix decreases the friction, while a contraction (collapse) increases it.

The *Bouchut* model also uses a Coulomb friction. However, in order to take dilatancy into account, Bouchut adds the tangent of the dilatancy angle to the tangent of the friction angle. This differs from Iverson who takes the tangent of the sum of both angles.

$$\vec{\tau}_s = (\tan(\varphi) + \tan(\psi))(N - p_b)\hat{e}_{v_s}. \tag{2.45}$$

In summary, all models employ a Coulomb-type friction to model the solid phase rheology; however, there are significant differences in exact model approach. It would be erroneous to use the same Coulomb friction angle for all models when applying each model to a specific case study.

Fluid friction

Each model considers some form of fluid friction. Both the *D-Claw* and *Bouchut* models employ a simple Newtonian viscous stress rheology. This approach assumes that the friction is proportional to the fluid velocity according to,

$$\vec{\tau}_f \propto \frac{\nu}{h}\vec{v}_f, \tag{2.46}$$

where ν is the (muddy) fluid viscosity. In the *Bouchut* model, the fluid friction is added to the solid momentum balance equation, to take into account the action of the fluid on the solid phase inside the mixture layer.

In *r.avaflow*, the fluid friction is divided into one Newtonian viscous term and a non-Newtonian one,

$$\vec{\tau}_f = \underbrace{\frac{\nu}{h}\vec{v}_f}_{\text{Newtonian}} + \underbrace{\frac{C_{NN}}{\phi_f h}\int_0^h \vec{\nabla}\phi_f(\vec{v}_f - \vec{v}_s)dz}_{\text{non-Newtonian}}, \tag{2.47}$$

where C_{NN} is a free model parameter controlling the magnitude of the non-Newtonian part of the fluid stress. Note that the non-Newtonian term belongs to the solid-fluid friction. Indeed, it is closer to a solid-fluid frictional term because it represents a momentum transfer from the fluid phase to the solid one. However, to stay consistent with the original paper [6], we include it in the fluid friction term.

Finally, in the model of *Titan2D*, Pitmann and Le assume that the fluid is inviscid. This implies that the pore pressure is the only fluid stress. As it is a two-fluid model that includes a mixture layer, the intergranular fluid friction is added to the solid momentum conservation equation (equivalently to *Bouchut*). Therefore, the fluid friction is entirely governed by the solid-fluid momentum transfer. The different model approaches are summarized in the overview Table 2.1. Here we would like to emphasize that a viscous drag term for the fluid phase looks plausible for a standard debris flow. However, it is unlikely that a viscous term will accurately capture the flowing behavior for a fast moving mud flow.

Solid-fluid internal friction

The computation of the momentum transfer between the solid and the fluid phases is one of the most difficult aspects of two-phase/layer debris flow models, especially in a macroscopic and depth-averaged framework. The primary problem is experimental as there is almost no data available to evaluate different model approaches. The momentum exchanges between the two phases can be weak, or strong. Strong interactions between the phases, represented by large velocity differences, can potentially induce stability problems, requiring small time-integration steps by the numerical equation solvers [95].

Iverson's *D-Claw* model essentially avoids the problem by computing an average velocity between the fluid and the solid fractions using a Darcy-like approximation. As we mentioned before, this method is a good approximation if the solid fraction governs the dynamics of the flow but is not adequate to reproduce the correct behavior of a fluid-driven (hyperconcentrated) flow.

Both the *Titan2D* and *Bouchut* models include the effects of buoyancy (first term of right-hand side) and a viscous drag term (second term of right-hand side) proportional to the difference between the solid and fluid velocities

$$\vec{\tau}_{sf} \; = \; \phi_s h_1 \vec{\nabla} p_e + \eta h_1 (\vec{v}_f - \vec{v}_s) \qquad \textit{Bouchout} \text{ model}, \tag{2.48}$$

$$\vec{\tau}_{sf} \; = \; \underbrace{h_s \vec{\nabla} p}_{\text{buoyancy}} + \underbrace{\phi_f \eta h (\vec{v}_f - \vec{v}_s)}_{\text{viscous drag}} \qquad \textit{Titan2D} \text{model}, \tag{2.49}$$

where η is a free parameter governing the viscous shearing force magnitude between the solid and the fluid. In the *Bouchut* model, only the excess pore pressure is used because the hydrostatic pressure has already been considered in the solid friction, throughout the effective stress, Eq. 2.45.

In *r.avaflow*, the viscous drag stress is similar to *Titan2D* and *Bouchut*. However, the drag term is proportional to the square of the solid-fluid relative velocity. The inertial stress due to the relative acceleration of the solid and the fluid (call 'virtual mass' term) is added to the formulation and is given by

$$\vec{\tau}_{sf} = \underbrace{C_{DG}(\vec{v}_f - \vec{v}_s)(|\vec{v}_f - \vec{v}_s|)}_{\text{Viscous drag term}} + \underbrace{C_{VMG}\frac{d}{dt}(\vec{v}_f - \vec{v}_s)}_{\text{virtual mass term}}, \tag{2.50}$$

where C_{DG} (generalized drag coefficient) and C_{MVG} (generalized virtual mass coefficient) are two additional free parameters of the model. Again an overview of the different approaches is contained in Table 2.1.

2.6.4 Erosion

The *D-Claw*, *Titan2D*, and *Bouchut* models do not consider sediment erosion. As entrainment can represent more than 90% of the mass of an event [76, 96], this limits the usefulness of these models in practical applications. It appears unlikely (see Chapter 5) that flow regime transitions can be modeled with considering torrent erosion.

The first version of the *r.avaflow* model [6] did not consider erosion. However, an extension has been implemented which includes erosion [53]. It is assumed that erosion is governed by the jump in the shear stress and the momentum at the interface between the flow and the basal surface. Two

expressions for the solid (E_s, see Eq. 2.24) and fluid (E_f, see Eq. 2.25) erosion rate are introduced,

$$E_s = E_s^{ri}(\phi_s)\sqrt{g_z h} \qquad \text{solid erosion rate,} \qquad (2.51)$$

$$E_f = E_f^{ri}(\phi_f)h\|\vec{v}_f\| \qquad \text{fluid erosion rate,} \qquad (2.52)$$

with E_s^{ri} and E_f^{ri} two constants depending on eight free parameters of the model.

As a comparison, we introduce the erosion model implemented in RAMMS one-phase debris flow model which is based on measured erosion rates at the Illgraben channel [40,50,51]. Assuming that there exists a critical shear stress τ_c, which is the threshold value for erosion to occur, the maximum potential erosion depth, d_{max}, is computed using the following formula

$$d_{max} = C(\tau_{max} - \tau_c), \qquad (2.53)$$

where C is a free parameter and τ_{max} is the maximum shear stress. Then, the erosion rate for solid E material is assumed to be uniform and constant, and the flow carries material until the erosion depth reaches d_{max}. Given the density of the eroded material and assuming that the soil is fully saturated, the ratio of solid-fluid entrained material is calculated.

Chapter 3

A Dilatant, Two-layer Debris Flow Model Validated by Flow Density Measurements at the Swiss Illgraben Test Site

abstract

We propose a dilatant, two-layer debris flow model validated by full-scale density/saturation measurements obtained from the Swiss Illgraben test site. Like many existing models, we suppose the debris flow consists of a matrix of solid particles (rocks, boulders) that is surrounded by muddy fluid. However, we split the muddy fluid into two fractions. One part, the inter-granular fluid, is bonded to the solid matrix and fills the void space between the solid particles. The combination of solid material and inter-granular fluid forms the first layer of the debris flow. The second part of the muddy fluid is not bonded to the solid matrix and can move independently from the first layer. This free fluid forms the second layer of the debris flow. During flow the rocky particulate material is sheared which induces dilatant motions that change the location of the center-of-mass of the solid. The degree of solid shearing, as well as the amount of muddy fluid and of solid particles, leads to different flow compositions – including debris flow fronts consisting of predominantly solid material, or watery debris flow tails. De-watering and the formation of muddy fluid washes can occur when the solid material deposits in the run-out zone. After validating the model on two theoretical case studies, we show that the proposed model is able to capture the streamwise evolution of debris flow density in time and space for real debris flow events.

3.1 Introduction

The assessment of debris flow hazard relies on both numerical simulation models [97, 98, 99, 100, 101, 102] and empirical methods [103]. Most numerical approaches solve shallow-water type equations [104] and therefore can be effectively applied to predict flow heights and debris flow run-out distances. Nonetheless, the application of numerical models in hazard engineering practice remains limited [105]. This is due to two salient problems. Firstly, it is difficult to quantify accurately the initial starting and entrainment masses for a specific torrent. And secondly, historical case studies are still necessary to calibrate the rheological parameters that govern debris flow motion at a specific site, and therefore possible inundation area [101, 102, 106]. Without this information, the motion of a debris flow is difficult to model because it depends strongly on the relative amounts of solid and fluid masses [107]. Typically, the front of the debris contains most of the rock material whereas the tail is more fluid like [108, 109], see Fig. 3.1. When the solid material stops in the run-out zone, the muddy fluid de-waters from the rocky material, or is overrun by the fluid tail, creating muddy floods and channel outbreaks [110]. The varying solid/fluid composition of debris flows leads to a wide range of possible deposition behaviors, making the prediction of the hazard extent for a specific torrent highly uncertain, [105].

Two-layer approaches that simulate both the motion of the rocky solid and muddy fluid would serve to alleviate many of these problems involved in modeling debris flows, including the specification of the initial conditions, modeling entrainment and selecting appropriate rheological parameters. This is evidenced by the recent development of several two-layer debris flow models [1, 2, 3, 6, 111, 112]. To apply these two-layer debris flow models in practice we must first demonstrate that they predict the correct streamwise structure of the flow. It must be shown that the distribution of solid and fluid material from the debris flow front to tail can be accurately modeled. This is a difficult problem because it depends both on entrainment processes (the entrainment of solid material at the leading edge of the flow), detrainment (solid mass loses at the debris flow sides) as well as the momentum exchange between solid and fluid components [113]. In many ways this problem can be considered experimental, in the sense that little data exists to substantiate/refute different model approaches that predict the evolution of flow density in the streamwise direction. Once the relative amounts of solid and fluid are known, these must be linked to follow laws that govern the bulk speed of the flow, as well as important processes such as de-watering and the eventual separation of the solid and fluid components. Again, this problem is a large part experimental, since there are few basal shear measurements of actual debris flows that would allow a testing of different modeling approaches.

In this paper we address the important problem of the distribution of solid/fluid mass in the debris flow body. Using density measurements captured at the Swiss Illgraben test site [114, 115], we model the streamwise structure of a series of debris flows. That is, we attempt to simulate the volumetric solid and fluid parts of the debris body, and therefore the flow density of the debris flow from initiation to run-out. Similar to many existing approaches, we adopt a shallow-water approach because of its computational speed. Within the framework of the shallow-water approach, we must therefore divide the fluid part of the debris flow into *inter-granular* and *free* parts in order to model the separation of the solid and muddy components, and therefore processes such as de-watering and fluid flooding. The data and model results integrate a series of recent works that introduce dilatant flow mechanics [1,2,116] into debris flow modeling. Although we present actual shear measurements

Figure 3.1: *A debris front passes a concrete check dam at the Illgraben test site on August 20, 2020. Note the blocky front and watery tail. The front appears to dam the muddy fluid flowing behind; the rocks in the tail appearing completely submerged in the muddy fluid. Saturation increases from front to tail. Photograph WSL.*

showing how shear resistance decreases with increasing fluid content, we do not address the rheology problem here, concentrating first on capturing the streamwise variation of bulk flow density.

The rest of this paper is organized as follows: in Sections 2 and 3 we describe the basic ideas behind our two-layer model, in Sec. 4 we present the governing equations of debris flows (mass and momentum conservation laws), in Sec. 5 we show the numerical results, the comparison to Illgraben measurements could be found in Sec. 6. The paper is rounded-off with some concluding remarks and an outlook to future work in Sec. 7.

3.2 Debris Flow Density, Solid Particles and Muddy Fluid

We consider a debris flow to be constituted of two material components: a solid component (subscript s) consisting of coarse granular sediment (e.g. boulders, cobbles, and gravel), associated with a density ρ_s, and a fluid component (subscript f) consisting of fine sediment likely to behave as suspended sediment (e.g. sand, silt, clay), hereinafter referred to as the muddy fluid content denoted by ρ_f. Although the grain-size distribution of the solid layer is likely to be important in the dynamics of debris flows [117], herein we do not consider grain size in our approach. We consider the individual solid particles to be undeformable; however, the ensemble of solid particles can be deformed and sheared, leading to different spacings between the particles. Therefore, the local bulk density of the debris flow ρ varies because it consists of a mixture of solid particles combined with different amounts of muddy fluid. For now, we will always make the assumption that the solid component is fully saturated with muddy fluid. It contains no interstitial air.

Most existing debris flow models [1, 2, 6, 111, 112, 118] consider the solid and fluid components to be two independent phases, moving with different velocities. They assume that the first phase/layer
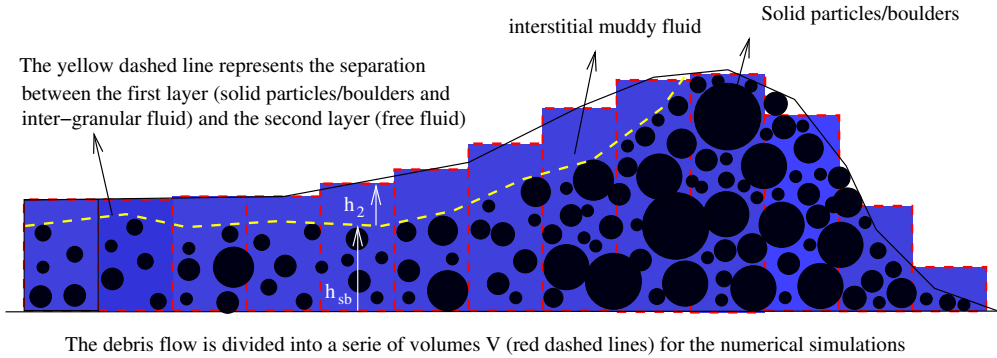
The yellow dashed line represents the separation between the first layer (solid particles/boulders and inter−granular fluid) and the second layer (free fluid)

interstitial muddy fluid

Solid particles/boulders

h_2

h_{sb}

The debris flow is divided into a serie of volumes V (red dashed lines) for the numerical simulations

Figure 3.2: *The debris flow is divided into a serie of volumes V. The flowing material is separate into two layers. The first layer is composed by all the solid mass (particles and boulders) and inter-granular fluid (h_{sb}), while the second layer is only composed by free fluid, ($h_{f,2}$), flowing on top of the first one. The density of the first layer can vary from dense flowing configurations (front of the debris flow) to wet flowing configurations (tail of the debris flow) under dilatancy, see Sec. 3.3 and Fig. 3.3.*

(subscript 1) is equal to the solid component and the second phase/layer (subscript 2) to be equivalent to the muddy component. Therefore, there can be no mass exchanges between the two phases/layer. Momentum can be exchanged between the two phases by shearing and rubbing interactions between the solid particles and the fluid mud.

In our model we follow the two-fluid assumption, [3, 4, 5, 41]. The first layer (subscript 1) consists of a mixture of solid particles *and* inter-granular muddy fluid that is bonded to the particle ensemble. The mass per unit area of this layer is denoted M_1. It consists of solid mass (M_s) and *inter-granular* fluid mass ($M_{f,1}$). The second layer (subscript 2) consists only of the fluid that is free to move independently of the first layer. We term this second layer the *free* fluid which has a mass $M_{f,2}$ (also per unit of area), Figs. 3.2 and 3.3. These relations can be mathematically expressed as,

$$M_1 = M_s + M_{f,1} = \rho_s h_s + \rho_f h_{f,1} = \rho_1 \underbrace{(h_s + h_{f,1})}_{h_{sb}} \tag{3.1}$$

$$= \rho_s \underbrace{(h_s + \frac{\rho_f}{\rho_s} h_{f,1})}_{h_1} \tag{3.2}$$

$$M_2 = M_{f,2} = \rho_f h_{f,2}. \tag{3.3}$$

The heights h_s and $h_{f,1}$ represent the height of the solid and inter-granular fluid components; they can likewise be considered as volumetric parts of the debris flow mass. Be aware that even if h_{sb} and $h_2 = h_{f,2}$ represent real heights of the first and second layers, this is not the case for h_s and $h_{f,1}$ which represent the volumetric concentrations of solid and inter-granular fluid in the first layer, respectively. The same remark holds for h_1 which does not have any physical meaning but is added to simplify the shallow water equations, Sec. 3.4. The total mass of the debris flow M is the sum

of the mass of layer 1 (solid particles and inter-granular fluid) and mass of layer 2 (free fluid),

$$M = M_1 + M_2 = M_s + \underbrace{M_{f,1} + M_{f,2}}_{M_f} = \rho_s h_s + \rho_f \underbrace{(h_{f,1} + h_{f,2})}_{h_f} \qquad (3.4)$$

where $h_f = h_{f,1} + h_{f,2}$ defines the total amount of fluid in the flow. In order to completely define our mass in a given volume, the last step is to differentiate the inter-granular and the free fluid. This is accomplished by assuming that the separation between the inter-granular and the free fluid is given by the location of the highest solid particle. We suppose that the solid content is homogeneously distributed in the first layer. Therefore, the center of mass of the solid is $\frac{h_{sb}}{2}$. Moreover, all the fluid which fills the void space is considered as bonded (it forms the inter-granular fluid component) and all the remaining fluid, is considered as free (see Figs. 3.2 and 3.3). All the fluid which flows above the first layer is considered free, and subsequently it can escape the matrix of solid particles, allowing the debris flow to de-water. Thus, fluid can escape from the solid part of the flow.

Finally, we denote the velocity of layer 1 as $\vec{v}_1$ [1]; the velocity of the second layer is $\vec{v}_2$. The velocity is a vector quantity as we consider velocity to be in two plane-parallel directions given by the digital terrain model.
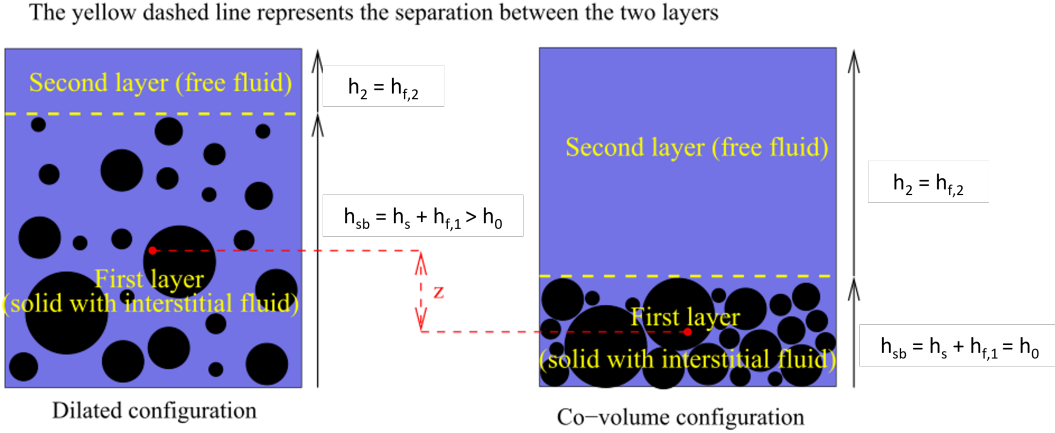

Figure 3.3: *Sketch of two different debris flow configurations, possessing the same amount of solid and fluid mass. The left one is a dilated configuration, happening during flowing, while the right one is the reference configuration, called the co-volume configuration, typically when the flow is at rest. The different heights we have defined in Sec. 3.2 and 3.3 are depicted here. The red dots show the center of mass of the corresponding configuration. The parameters z, introduced in Eq. 3.6, is the difference between the centers of mass of the dilated and co-volume configuration.*

3.3 Dilatancy in the Solid Boulder Matrix

The basic idea behind our model is to describe the debris flow as a dilating mixture of solid particles (boulders, rocks) and muddy fluid. Because of shearing interactions between the individual particles and the ground, the solid matrix dilates; that is, the spacing between the particles can increase or decrease, changing the overall volume of the first layer, [80]. More precisely, in our model, dilatancy will be responsible of fluid mass exchanges between the two layers. These mass exchanges

---

[1] We assume zero slip between the granules and the inter-granular fluid.

will change the flow composition and allow us to have a varying density profile inside the flow. Indeed, without dilatancy, our model would be closer to two independent one-layer model than a real two-layer model with interactions. Therefore, the density evolution in our model is the consequence of dilatancy.

We define three variables associated with the solid mass, h_s, h_0 and h_{sb}. The height h_s is the volume of the solid particles in the flow, h_0 represents the reference height of the non-dilated mass, we call it the co-volume[2], whereas h_{sb} represents the dilated height of the solid mass, Sec. 3.2 (see Fig. 3.3). We refer to h_0 as the *co-volume*, in an analogy to Van der Waals work on non-ideal gasses with large molecules and cohesion [119]. Note that, even if the solid mass is conserved, the first layer density can vary, according to Eq. 3.1, if the inter-granular fluid concentration evolves :

$$\rho_1 = \frac{\rho_s h_s + \rho_f h_{f,1}}{h_s + h_{f,1}} \tag{3.5}$$

The potential energy V_D (per unit area) associated with the dilatation of solid material is

$$V_D = \underbrace{[\rho_s - \rho_f] h_s}_{\text{buoyant mass}} g \underbrace{\frac{1}{2} [h_{sb} - h_0]}_{z}. \tag{3.6}$$

where z is the distance between the center of mass of the dilated configuration and the co-volume one, Fig. 3.3. Because the configuration of the particles in the dilated volume defines the potential energy V_D, we sometimes refer to the energy V_D as the *configurational energy* of the debris flow [120, 121, 122]. Importantly, we are making the following physical assumption: the potential energy is associated with the *buoyant weight* of the solid particles immersed in the inter-granular fluid. Any change in z implies a change in the potential energy, $\Delta V_D \propto \Delta z$.

For a debris flow, changes in void space are always associated with movement of the interstitial muddy fluid. When the void space between particles increases, fluid will fill the space between particles, or conversely, when the void space decreases, fluid will be squeezed out. Fluid mass that fills the void space will eventually move at the same speed as the particles and therefore becomes inter-granular, whereas fluid that is squeezed out becomes free to move independent of the particulate mass. This implies there is a mass exchange between the inter-granular and the free fluid components, that depends on the void space of the solid mass. If the flow is dilating, typically just after the release, free fluid is transformed into inter-granular fluid. Inversely, if the solid void space is decreasing (e.g. in the run-out area) the rate of fluid exchange changes, and inter-granular fluid becomes free (de-watering). To model this effect, we let Q_f denote the rate of the fluid mass exchanges. It can be calculated directly from any change in the distance between the center-of-masses of the reference and dilated configurations Δz,

$$Q_f \Delta t = \Delta z. \tag{3.7}$$

In this paper the configurational energy V_D is governed by a simple production (parameter α) and decay (parameter β) term, similarly to what has been used for snow avalanches, see [80]:

$$\frac{\partial V_D}{\partial t} + \vec{\nabla} \cdot (V_D \vec{v}_1) = \alpha \dot{W}_f - \beta V_D. \tag{3.8}$$

---

[2]It is different from h_s, because we consider that, even in the non-dilated configuration, the void space is not zero

The quantity W_f represents the shear work. That is, the change in the energy of configuration V_D (dilatation) is directly related to the shear work, in accordance to Reynolds [78]. The parameter α defines the fraction of the shear work that produces a dilatation, whereas the parameter β defines how quickly the dilatation collapses in the absence of shear, due to energy dissipation caused by shearing between particles. The balance between the production of V_D and its decay essentially defines the degree of saturation in the debris flow, as this defines the amount of void space (inter-granular water) in the moving solid. As we will show in the final section, the parameters α and β can be determined from experimental measurements such as the ones in Illgraben.

An important fact is that mass exchanges between the inter-granular and free fluid components are also associated with a transfer of momentum ($\vec{P}$) between the two debris layers.

3.4 Model Equations

Depth-averaged mass conservation equations can be written for the three material components $h_{f,1}$ (inter-granular fluid), h_1 (first layer) and $h_2=h_{f,2}$ (free fluid),

$$\frac{\partial h_{f,1}}{\partial t} + \vec{\nabla} \cdot (h_{f,1}\vec{v}_1) \;\; = \;\; Q_f \qquad \text{inter-granular fluid} \qquad (3.9)$$

$$\frac{\partial h_1}{\partial t} + \vec{\nabla} \cdot (h_1\vec{v}_1) \;\; = \;\; \frac{\rho_f}{\rho_s}Q_f \qquad \text{first layer} \qquad (3.10)$$

$$\frac{\partial h_{f,2}}{\partial t} + \vec{\nabla} \cdot (h_{f,2}\vec{v}_2) \;\; = \;\; -Q_f \qquad \text{free fluid} \qquad (3.11)$$

where $\vec{\nabla}$ is the divergence operator in Cartesian coordinates. The right-hand side of the inter-granular fluid and free fluid equations contains the term Q_f, Eq. 3.7, which is the mass exchange rate between the inter-granular and free fluid because of dilatant actions in the solid matrix. In Eq. 3.10, as well as in Eq. 3.12, we include the density as the left hand side contains the density ρ_s, Eq. 3.2, while the right hand side contains the density of the muddy fluid. Here we assume no entrainment of solid material from the mountain torrent. Note that in Eq. 3.10, as well as in Eq. 3.12, we use h_1 instead of h_{sb}. Indeed, h_1 has a constant density, which allows us to simplify the equations. In this form, the equations are mass conservative. Note also that it is possible to find the equation for the boulders/solid content of the flow combining Eq. 3.9 and 3.10 together with Eq. 3.2.

We have in total four momentum conservation equations, viz. two equations for each of the two layers. If $b := b(x,y)$ denotes the bottom topography, they can be written in vectorial form as [123, 124]:

$$\partial_t(h_1\vec{v}_1) + \vec{\nabla} \cdot \left(h_1\vec{v}_1 \otimes \vec{v}_1 + \frac{gh_1^2}{2}I \right) + gh_1\vec{\nabla}\left(b + \frac{\rho_f}{\rho_s}h_{f,2} \right) \;\; = \;\; -\frac{\vec{\tau}_1}{\rho_s} + \frac{\rho_f}{\rho_s}\vec{P} \qquad (3.12)$$

$$\partial_t(h_{f,2}\vec{v}_2) + \vec{\nabla} \cdot \left(h_{f,2}\vec{v}_2 \otimes \vec{v}_2 + \frac{gh_{f,2}^2}{2}I \right) + gh_{f,2}\vec{\nabla}\left(b + h_{sb} \right) \;\; = \;\; -\frac{\vec{\tau}_2}{\rho_f} - \vec{P} \qquad (3.13)$$

The first, resp. second, equation represents the first, resp. second, layer. The symbol $\otimes$ denotes the tensor product and I is the two-dimensional unity matrix. The left side is the total variation of the momentum with respect to time, including the effect of gravitation and the influence on one phase to the other, [123, 124]. The right side represents the change in momentum due to external

forces (excluding gravitation). $\vec{\tau}_i$ is the shearing stress acting on the i-th layer. As we are using the Voellmy-Salm model [125], the shearing stresses can be expressed as:

$$\vec{\tau}_i = \left(\mu_i N_i + \frac{g||v_i||^2}{\xi_i} \right) \hat{e}_i \tag{3.14}$$

N_i is the $i - th$ layer normal stress and $\hat{e}_i$ the unit vector along the flowing direction : $\hat{e}_i = (\frac{v_{i,x}}{||v_i||}, \frac{v_{i,y}}{||v_i||})^T$. The gravity component g_z is the slope-perpendicular acceleration due to gravity, $g_z = g\sin(\theta)$ where θ is the slope angle of the corresponding cell. We emphasize that we neglect the shearing between the two layers. Indeed, we can consider the shearing processes acting at the interface between the two layers as a Coulomb type friction. However, we use a value of the fluid Coulomb coefficient close to zero ($\mu_2 \approx 0.01$). Therefore, the shearing between the two layers can be assumed negligible.

Finally, $\dot{P}$ is the rate of momentum exchange associated with the mass exchange. Because Eq. 3.12 is defined per unit of ρ_s, while Eq. 3.13 is defined per unit of ρ_f. Together, these terms invoke Newtons' third law of action and reaction between the layers. The momentum exchange rate can be expressed as,

$$\vec{P} = \begin{cases} Q_f \vec{v}_2 & \text{if the first layer is dilating} \quad \dot{h}_1 > 0 \\ Q_f \vec{v}_1 & \text{if the first layer is collapsing} \quad \dot{h}_1 < 0 \end{cases} \tag{3.15}$$

3.5   Numerical Validation

Various numerical schemes for depth-averaged shallow-water type equations can be applied to solve numerically this system of equations [104, 126, 127]. We numerically solve Eqs. 3.8 -3.13 using finite volume schemes within the RAMMS avalanche software [43]. The equations are solved in two steps. First, we solve the hyperbolic part of the equations, i.e. without the source term (right-hand side) using a second order ENO scheme. The second step is to integrate the source terms using a second order Runge-Kutta method.

To check the mathematical consistency of the model (Eqs. 3.6 and 3.8 to 3.13), we performed two numerical tests. The first test is designed to test the stability of the three-component momentum equations (solid, free and inter-granular fluid) while the second test is designed to check the mass conservation between the inter-granular and free fluid contents during dilatative changes in the solid boulder/rock matrix.

The first test is based on the idea that for a steady flow, the dimensionless Froude number is constant, defined only by the Voellmy-type friction parameters μ and ξ in relation to the slope angle θ. This condition must hold for the two-component flow (inter-granular fluid/solid material) even if the solid material is undergoing shearing and dilatative changes. The derivation of this fact is contained in a short Appendix, 3.9.1. We therefore performed block release simulations on a flat plane with a uniform slope angle, Fig. 3.4.a. The plane connects to a flat run-out area. In order to prove the existence of steady-state our interest is directed towards the slope above the run-out plane. Obviously in real-terrain conditions, the flow would generally not reach a pure steady state configuration.

The convergence of the numerical simulations to the theoretical results is depicted in Fig. 3.4a (input parameters are summarized in Table 3.5). Here, the Froude number is plotted as a function

of the simulation time t. The red curves represent the theoretical Froude numbers evolution for a sliding rigid block (see Appendix, 3.9.1) for two different sets of friction values (Table 3.5, markers 'x' and '+'), while the blue markers are the numerical outputs. The mass of the block used in the theoretical computation is equivalent to the initial mass of the release block used in the numerical simulations. This plot reveals an important feature of model; namely, that in steady-state, there are no dilatative changes in the solid boulder/rock matrix. The flow density is constant in steady-state and therefore there is no changes in the amounts of free and inter-granular fluid components. Indeed, momentum exchanges would result in a deviation in the Froude number convergence. Therefore, a constant Froude number, which coincides with the mathematically computed value, means that no momentum exchanges are occurring, which is the proof that the flow has attained a constant density[3]. Changes in slope angle encountered in real torrents therefore always produce changes in the debris flow density and streamwise structure.

Note that in the mathematical derivation of the Froude number value, Appendix 3.9.1, we do not consider the influence of one phase on each other. However, this effect is taken into account when we performed the numerical simulations. The fact that the numerical output converges to the theoretical value shows that these effects are negligible. Therefore, the mathematical derivation can be considered as valid even for a dilatant two-layer model with phase interactions.

Simulation	μ []	ξ $[m/s^2]$	θ [°]	Froude Number
1 ('x')	0.1	100	15	1.29
2 ('+')	0.15	300	30	3.36

Table 3.1: *Summary of the free parameters governing the Froude number value.*

The second consistency check demonstrates that when the debris flow is outside steady-state, and there are changes in the streamwise structure and dilatant actions in the boulder/rock component, the mass of free and inter-granular fluid (total fluid) are always conserved. Therefore, for model consistency, we have to check that the entire amount of fluid contained in the flow is conserved with time. The simulations are again perform on an ideal, flat plane with a constant 30°slope. This time, however, we are interested when the flow leaves the slope and enters the run-out zone; that is, when the flow is no longer in steady-state as in the previous case. We have plotted the mass of the different fluid flow components as a function of the time for three values of α : 10%, 15% and 20%, Fig.3.4.b. The orange and red curves represent the free and inter-granular fluid for $\alpha = 10\%$, while the blue lines are the total fluid composing the flow (sum of the two previous curves). the green and cyan dashed lines are the evolution of free(lower curves) and inter-granular (upper curves) fluid, for $\alpha = 15\%$ and $\alpha = 20\%$. This result demonstrates that fluid mass is conserved during unsteady motions in uneven terrain. Moreover, we can check that the mass exchanges (and therefore the debris flow saturation), increase with α, which is the consistent numerical behavior.

3.6 Comparison to Illgraben Measurements

The Illgraben debris flow test site (Fig. 3.5) is located near Leuk, Canton Valais, Switzerland [107, 114, 115]. Since 2005, the Illgraben torrent has been instrumented with a rectangular force

---

[3]A constant density does not mean that the streamwise density distribution is uniform.
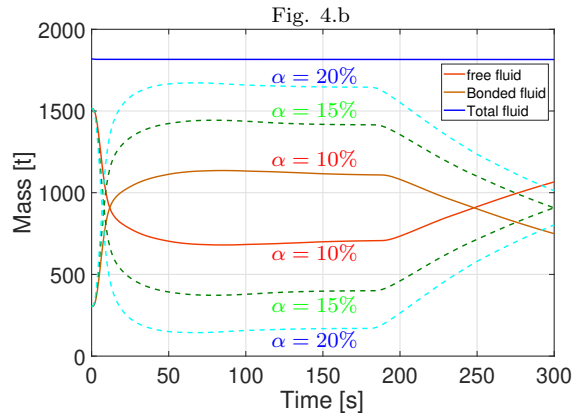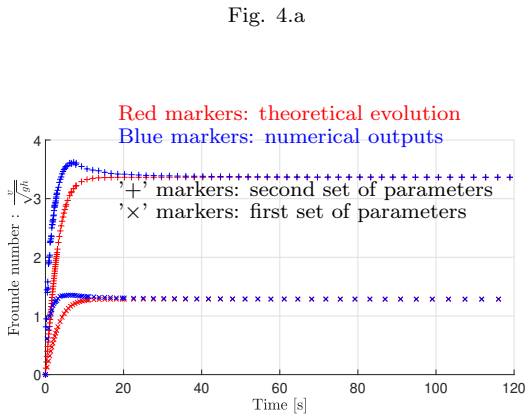
Figure 3.4: *a) Results of two simulation checks. For a flow on a flat slope governed by Voellmy-type friction parameters, the Froude number is constant at steady-state. b) The total fluid mass composing the flow is plotted as a function of the time. The dark orange line is the inter-granular fluid, the light orange line is the free fluid; the blue line is the total amount of fluid, i.e. the sum of the two previous ones, for $\alpha = 10\%$. The dashed line represent the inter-granular (upper curves)-free(lower curves) fluid evolution for two different values of alpha, i.e. $\alpha = 15\%$ (green dashed lines) and $\alpha = 20\%$ (cyan dashed lines). Total fluid is conserved as slope changes cause unsteady motions.*

plate (area A=4m^2) that measures shear (S) and normal (N) stresses at the base of a passing debris flow. A laser sensor located above the plate measures the total debris flow height h as the flow passes over the plate. The force plate is located at the end of a 2.5km long torrent (in orange on Fig. 3.5) that has an average slope of 5°. The torrent is fed by a large (9.5km^2), steep catchment zone (in blue on Fig. 3.5), which supplies the measuring channel with debris flows of various sediment/fluid compositions. In this paper we consider four specific debris events, see Table 3.6. All four events can be considered single surges, with well-defined front-tail structure. The debris flow fronts contained boulders and rocks, leading to large measured normal stresses $N \approx$ 20kPa - 25kPa (Fig. 3.6a, 3.6b, 3.6c and 3.6d). The debris flow fronts were followed by fluid tails containing much less solid mass, reducing the measured normal stresses.

From the measurement data it is possible to estimate the streamwise bulk density ρ of the flow, and therefore the time-variation of the solid and fluid components as debris flow passes over the plate. Keeping the same notation as in Sec. 3.2, we can write the two following equations:

$$h = h_s + h_f \tag{3.16}$$

$$M = \frac{NA}{g_z} = A(\rho_s h_s + \rho_f h_f) = \rho h A. \tag{3.17}$$

In these equations, M is the total mass running over the plate which has the mean bulk density ρ. As the basal area A is constant we can represent the volumetric components of the solid/fluid as a corresponding height. With these Equations, we can equivalently write,

$$\rho = \frac{\rho_s h_s + \rho_f h_f}{h_s + h_f} \tag{3.18}$$

$$h_s = h \left[\frac{\rho - \rho_f}{\rho_s - \rho_f} \right]$$

$$h_f = h \left[\frac{\rho_s - \rho}{\rho_s - \rho_f} \right]. \tag{3.19}$$

Therefore, thanks to this experimental setup, we can extract from the measurements the streamwise evolution of the bulk density, Eq. 3.18. (Equivalently it is possible to calculate the volumetric fluid concentration $\frac{h_f}{h}$). In the four events studied, the variation of the density with respect to time is highly different from one event to the others (Fig. 3.6a, 3.6b, 3.6c and 3.6d). However, the variation of the density with the normal stress exhibits a similar behavior for each of the measured events (Fig. 3.7a, 3.7b, 3.7b and 3.7d). The color is an additional time information. The blue markers represent the front of the flow and time is evolving as we approach the yellow color. From this time information, we can check that the flow density is higher in the front (blue) than in the tail (yellow). As a consequence of the uniformity in the density-normal stress space, we compare the density behavior with respect to the normal stress, rather than the time variation of the flow composition itself.
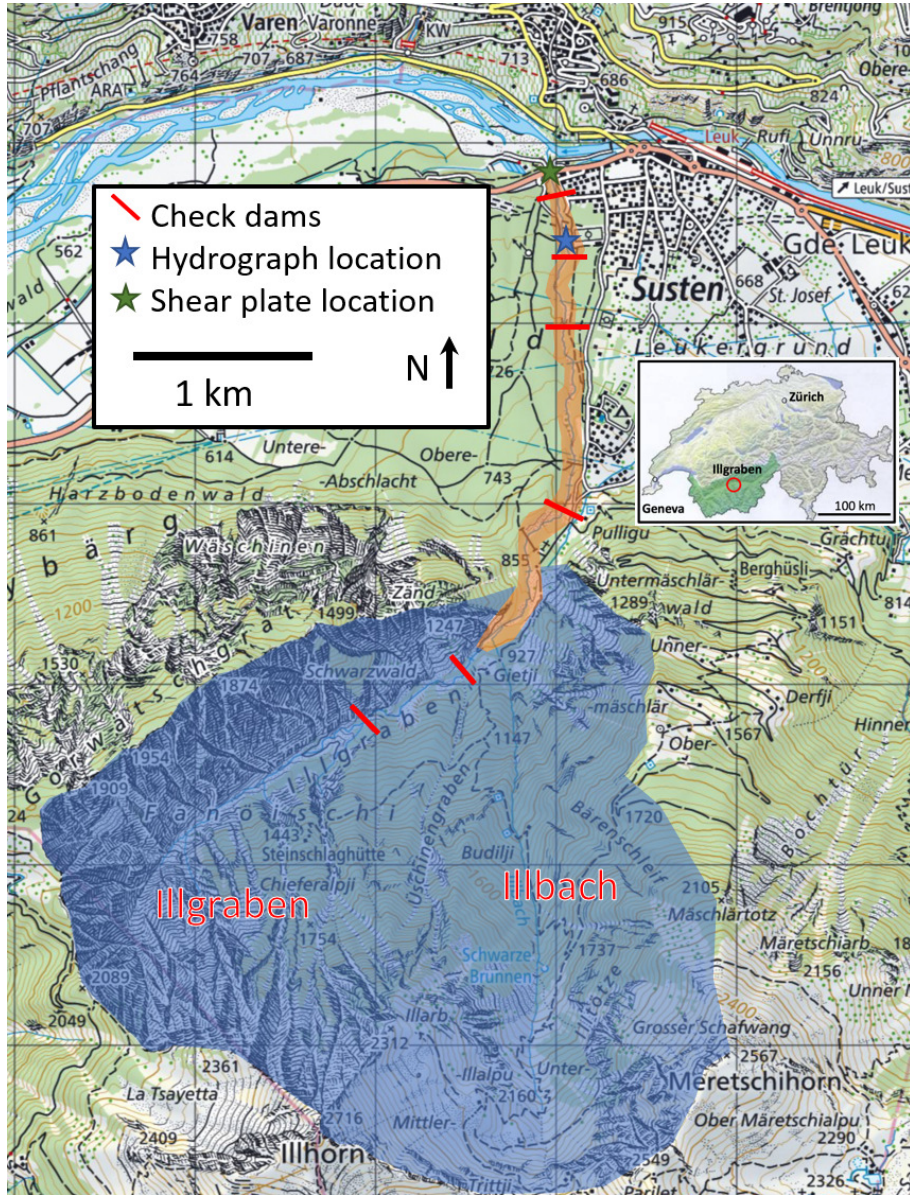
Figure 3.5: *Map of the Illgraben test site. The catchment zone is given by the blue polygon, while the channel is drawn in orange. The check dams are also shown (red line). The blue star represents the starting point of the hydrogaph, used for the numerical simulation, and the green star is the location of the shear plate. The original map can be found in [107].*

Event	Description	$\approx$ Max flow height	$\approx$ Time event	$\approx$ Front velocity
(a) 02.08.2005	Event with a high density: rocky event	1.1 m	20 min	no data
(b) 28.07.2006	Unconventional event the tail becomes again less saturated	1.5 m	55 min	2 m/s
(c) 31.08.2008	Rocky front and very fluid tail, large saturation difference between the front and the tail	1.4 m	25 min	1.9 m/s
(d) 29.07.2013	extremely fluid event	1 m	50 min	1.9 m/s

Table 3.2: *Main characteristics of the simulated debris flows.*

(a) *Event of the 2nd August 2005*

(b) *Event of the 28th July 2006*

(c) *Event of the 31th August 2008*

(d) *Event of the 29th July 2013*
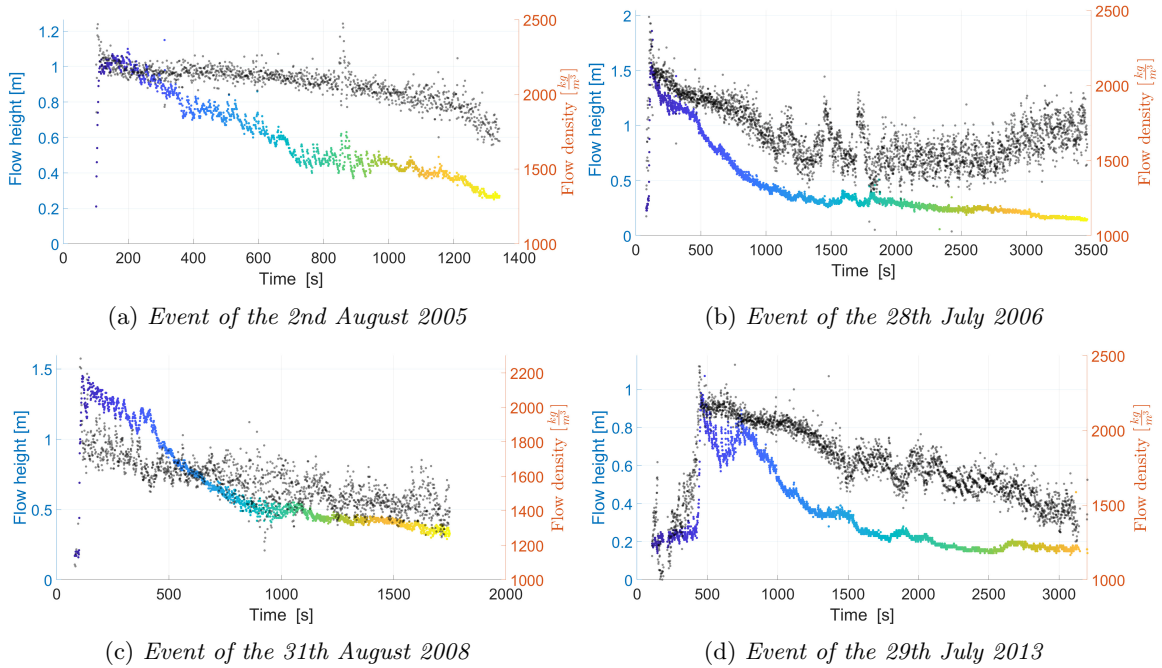
Figure 3.6: *Data of the Illgraben data measurements. The colored markers plot the flow height behavior, whereas the black markers plot the density evolution. Both markers are plotted with respect to time. The color is an additional temporal information, the blue represents the front and the yellow the tail.*

In Fig. 3.6a, 3.6b, 3.6c and 3.6d, the debris flow height (colored curves) and the density (black curves) is plotted as a function of time for the four different events. Colour should help to guide the reader over the duration of the event. However, be aware that the color is more an indication than a real temporal data. Indeed, for both sub- graphics, the two curves (Illgraben data and numerical outputs) do not have the same duration. Therefore, the yellow markers, by instance, represent in both (Illgraben and numerical simulation) case the end of the flow, but are associated with different times.

To validate our model, we have selected four events at the Illgraben site: the 2nd of August 2005, the 28th July 2006, the 31th August 2008 and the 29th July 2013. We use a hydrograph for the release method [128]. In order to compare the numerical prediction with the experimental results, we have selected four cells (a square of 2 by 2 cells), corresponding to the shear place location. For
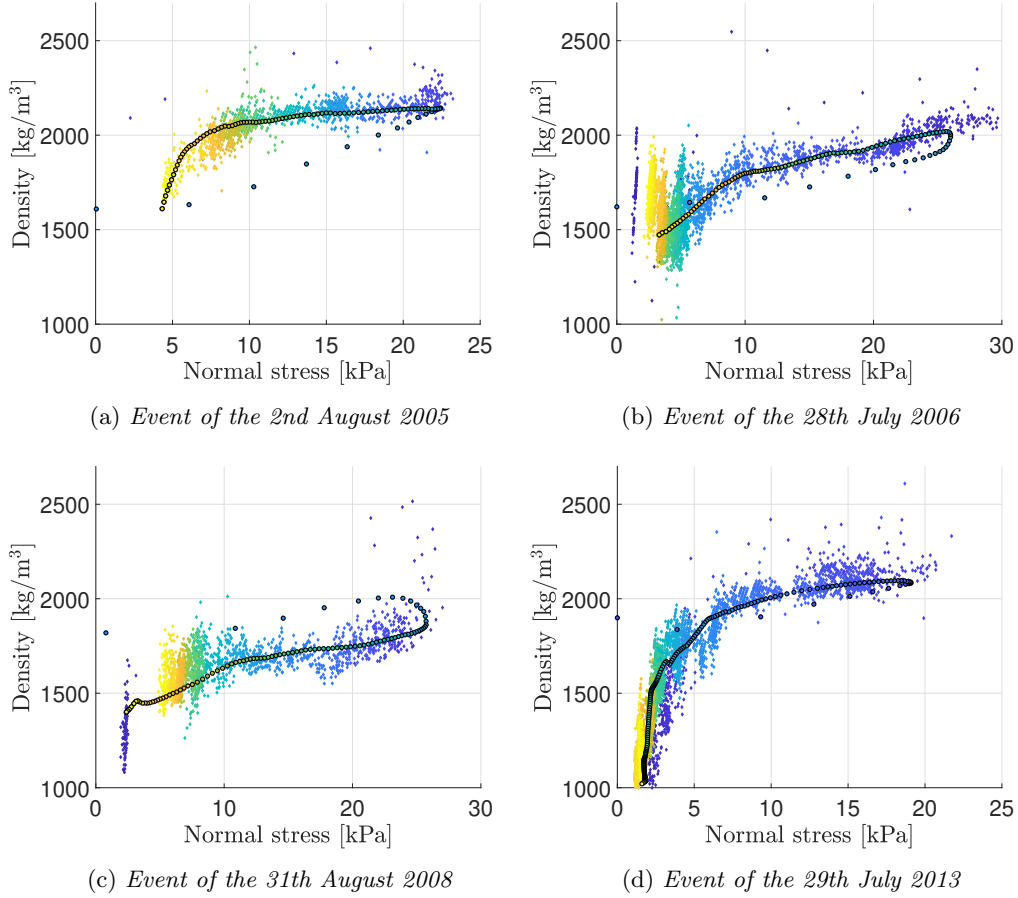
(a) *Event of the 2nd August 2005*

(b) *Event of the 28th July 2006*

(c) *Event of the 31th August 2008*

(d) *Event of the 29th July 2013*

Figure 3.7: *Comparison between Illgraben data and numerical simulations results. Bulk density ρ as a function of normal stress N. The colored dots are the experimental data while the black edge dots are the numerical outputs. The color is an additional temporal information, the blue represents the front and the yellow the tail.*

comparison we used the average of different variable of the debris flow on these cells.

The comparison between experimental and numerical results is shown in Fig. 3.7a, 3.7b, 3.7c and 3.7d, which plots the first layer density as a function of the first layer normal stress. The colored dots are the experimental data while the black edge symbols, filled with color, are the numerical outputs. These results suggest that the dilatant, two-component model is able to reproduce the streamwise density structure of several debris flows observed at the Illgraben test site. The numerical results not only predict the correct dependency between density and normal stress, but also the correct time dependency. Although this is a positive result, it must be emphasized that the model is not able to differentiate between the inter-granular and free fluid components and therefore the exact degree of solid dilatation. This is largely due to the fact that the Illgraben data, although extensive, does not provide a means to separate the inter-granular and fluid parts of the interstitial muddy fluid. We are able only to measure the sum of the muddy fluid passing the normal plate over time. This leads to an important observation: as we cannot distinguish the interstitial and free fluid from the Illgraben measurements, we can choose to match the experimental data either with the first layer density or with the entire debris flow density. We have chosen the former case
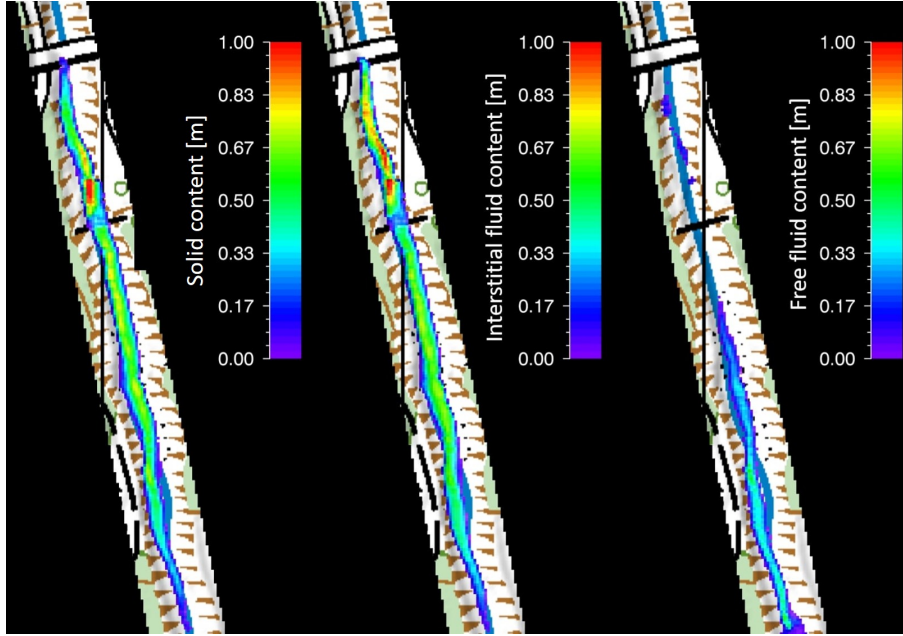
Figure 3.8: *Three pictures of the simulations performed to match the 2013 event. From left to right: the solid height, the interstitial fluid height and the free fluid height. The picture is taken when the first layer reaches the shear plate. We can see here an important point of the model: during flowing, a large part of the fluid belongs to the first layer and there is only a small amount of free fluid left.*

for the following reason. Our final goal is to compute the flow rheology as a function of the flow composition. However, in our model the rheology of the first layer only will change, because the second layer is completely composed by fluid. Therefore, it is relevant to match the data with the first layer only, as this will determine in large part the rheology of the flow [4]. Moreover, we can also choose to initialize the flow in a already dilated configuration, in which case all the fluid is assigned to belong to the first layer and there is no free fluid as long as the solid matrix does not start to collapse. However, we did not use this way to initialize the flow for consistency reasons. Indeed, we wanted to show that we were able to catch the right density profile even when we initialize the flow in the co-volume configuration, to demonstrate the applicability of the dilatancy approach.

As a last results, we show on Fig. 3.8, the time-spatial evolution of the three flow contents, that is to say: the solid matrix, the interstitial fluid and the free fluid. One can see an important aspect of the model. During flow, the amount of free fluid is small with respect to the first layer, which is the sum of the two left plots.

3.7   Discussion and Conclusion

Measurements of S/N ratios of debris flow reveal a strong decrease in friction with increasing volumetric fluid content (Fig. 3.9a, 3.9b, 3.9c and 3.9d). This statement can, of course, be alternatively stated: S/N ratios increase with increasing solid content. However, the experimental data reveals an important second point: the solid/fluid content distribution varies in the streamwise direction. Often, the debris flow front contains less fluid than the tail, indicative of higher friction, or bulking,

---

[4]We can also possible to match the Illgraben measurements with the entire flow data.

at the leading edge of the flow (Fig. 3.6a, 3.6b, 3.6c and 3.6d). The solid mass will have a tendency to stop sooner, in comparison to the fluid concentrated tails, causing a wide array of different stopping possibilities in run-out zones. Stopped solid concentrations can de-water, or be overflown by their muddy tails. Torrents can be blocked and dammed, leading to channel outbreaks and muddy flows that inundate large areas.
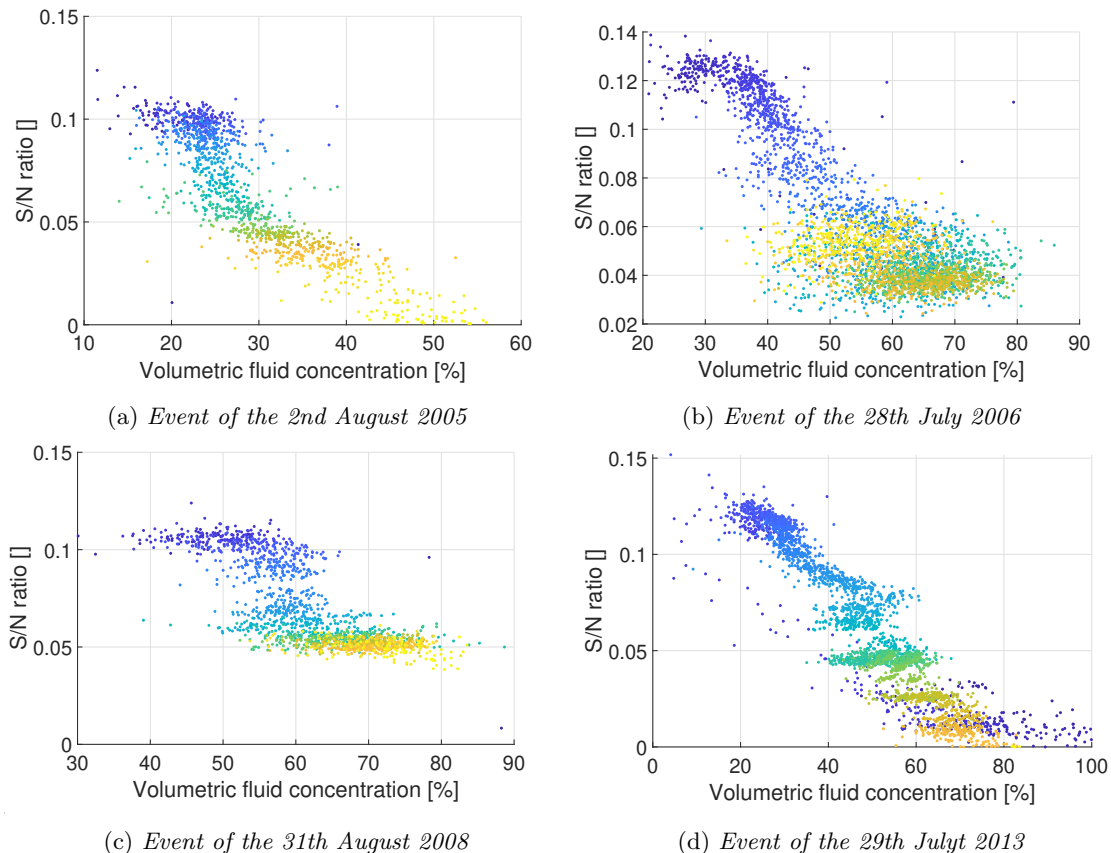

(a) *Event of the 2nd August 2005*

(b) *Event of the 28th July 2006*

(c) *Event of the 31th August 2008*

(d) *Event of the 29th Julyt 2013*

Figure 3.9: *Experimentally measured S/N ratio as a function of the measured saturation. Each dot represents an experimental measurement. The color is an additional temporal information, the blue represents the debris flow front and the yellow the tail.*

The first step to model accurately the mobility of a debris flow is the ability to predict the variation of volumetric fluid/solid components – essentially the streamwise variation of the bulk density from the head to the tail of the flow. This task cannot be achieved within the framework of simple one-layer models and is the purpose of this paper.

The approach adopted in this paper is to divide the fluid content into two parts – the intergranular part (that moves with the speed of the solid matrix) and the free fluid (which moves independently from the solid). We assume that all fluid that can be contained in the void space of the solid is inter-granular. The problem here is that the void space is continuously changing because of the continuous interactions between the rocks and boulders themselves and the ground. Shearing changes the volume of the solid matrix and thus the relative amounts of inter-granular and free fluid. Importantly, the solid concentration moderates the speed of the overall flow, causing the fluid to move at a slower speed, backing up the fluid into the tail of the debris flow. With this approach it was possible to simulate the density variation (i.e. the volumetric fractions of solid/fluid) in the

streamwise direction.

The model imposes two physical constraints:

1. *In steady-state, there is no variation in the solid configuration, and therefore the density is constant.* Volumetric dilatation in the solid matrix are governed by the balance between the shear work rate (production) and collapse of the volume in the surrounding fluid (decay). In steady state the work done by shearing is constant and equal to the collapse rate, leading to a constant solid volume and therefore a constant void ratio. In this case there can be no exchange between the inter-granular and free fluid fractions which remain constant. This leads to constant Froude numbers in the steady-state, and, because no mass can be exchanged, in turn to no momentum exchange between the two components. On steep slopes, the production term dominates leading to more dilated flows with suspended particles. In the run-out zone, the flows collapse, the particles return to the basal layer and the void space disappears. The debris flows de-waters.

2. *Mass exchanges imply momentum exchanges.* In existing debris flow models [1, 2, 6, 111, 112], momentum exchanges must be devised to regulate the speed of the two phases/layers solid/fluid models. By transferring mass between the inter-granular fluid locked in the solid matrix and the free fluid, we also transfer momentum. The transfer of momentum is regulated by the void space (dilatation) in the solid boulder/rock matrix of the flow. As we have demonstrated in the numerical examples, these momentum exchanges will only occur when the flow is in a non-steady-state. For example, when the flow is undergoing sharp slope changes such as when entering the run-out zone. Of importance, is the fact that the transfer of mass and momentum between the solid/inter-granular fluid (layer 1) and free fluid (layer 2) layers regulates both the speed and the density of the debris flow.

In our debris flow model formulation, the free fluid has two main roles. First, it surrounds the solid matrix and therefore facilitates the buoyant dispersion of the solid mass. It effectively allows dilatancy and therefore streamwise density variations. Secondly, when the solid matrix stops, the solid particles deposit out of the fluid content. It then becomes possible to simulate phase separation (de-watering) between the solid and free fluid.

Alternatively, when the debris flow mixture is still flowing, a significant proportion of the fluid is flowing at the same speed as the solid in the inter-granular void space. The amount of the free fluid layer is small comparing to the first layer, Fig. 3.8, in some cases non-existent. Another important practical point is that we can initiate the flow in an already dilated configuration by using an hydrograph. Therefore, we start the debris flow as a single layer flow, assigning all fluid to be inter-granular. It means that in this case, the two-layer model reduces to a one-layer model, which implies a reduction in computational time, while keeping the possibility to have a density profile. Only in the run-out zone, when the solid matrix deposits, will the inter-granular fluid become free.

To summarize, our model is able to predict the complexities of two-layer behavior (streamwise density distribution, phase separation), while solving, for a large part of the simulation time, a system of one layer equations. This offers the possibility to reduce calculation time, which is an crucial aspect in practical engineering applications. With regard to the flow rheology, we note that the experimental decrease in S/N (Fig. 3.9a, 3.9b, 3.9c and 3.9d) appears almost linear with volumetric fluid content, providing strong evidence of effective stress like concepts which reduce the

shear stress linearly with increasing fluid pressure. A first step to develop and test different two-layer rheological models is first to capture the streamwise density variation of the flow. Although our major goal was to develop a model for practical applications, because we can define variable amounts of solid and muddy fluid, the model might help also to understand how debris flow mobility will be affected in a changing climate, where we expect changing geomorphological and precipitation conditions.

3.8   Acknowledgments

3.9   Annex

3.9.1   Appendix A: Analysis of a Sliding Block along an Inclined Plan with a Vollemy-Salm Shearing Model
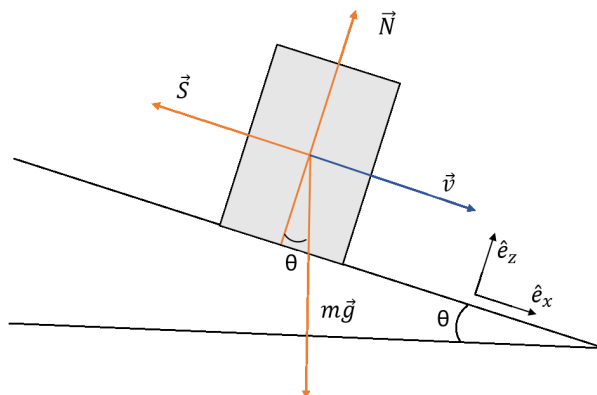
Figure 3.10: *Block sliding on a flat plan with constant slope angle θ.*

In this section we study the mathematical solution of a sliding rigid block along an inclined plan with a constant slope angle θ. The shearing stress will be given by the Vollemy-salm model. it means :

$$\vec{\tau} = \mu N \hat{e}_{\vec{v}} + \frac{\rho g}{\xi} v^2 \hat{e}_{\vec{v}} = \left(\mu N + \frac{\rho g v^2}{\xi} \right) \hat{e}_x \tag{3.20}$$

Where A is the basal area, $\vec{v}$ is the center of mass velocity, always parallel to the slope direction $\hat{e}_x$ (we suppose than either the ground and the block are unalterable). If we use the second law of Newton and we decompose the forces along $\hat{e}_x$ and $\hat{e}_z$, slope perpendicular direction, it gives:

$$\text{along} \quad \hat{e}_x \quad \rightarrow \quad mg\sin(\theta) - \frac{\rho g A v^2}{\xi} - \mu N A = ma = m\dot{v} \tag{3.21}$$

$$\text{along} \quad \hat{e}_z \quad \rightarrow \quad -mg\cos(\theta) + NA = 0 \tag{3.22}$$

Combining these two equations, we find a first-order differential Eq.:

$$mg\sin(\theta) - \frac{\rho g A}{\xi}v^2 - \mu mg\cos(\theta) = m\dot{v} \tag{3.23}$$

We can solve it with respect to v. After integration, with the initial condition $v(t = 0) = 0$ we obtain:

$$v(t) = \frac{\Omega}{\sqrt{\zeta}}\tanh\left(\frac{\Omega\sqrt{\zeta}}{m}t\right) \tag{3.24}$$

with $\Omega^2 = mg(\sin(\theta) - \mu\cos(\theta))$ and $\zeta = \frac{\rho g A}{\xi}$. Therefore, for time long enough ($\lim_{t\to\infty}$), the block reaches a steady state, given by the steady value:

$$Fr = \lim_{t\to+\infty}\frac{v(t)}{\sqrt{gh(t)}} = \sqrt{\frac{\xi(\sin(\theta) - \mu\cos(\theta))}{g}}\left[\underbrace{\lim_{t\to+\infty}\tanh\left(\frac{\Omega\sqrt{\zeta}}{m}t\right)}_{=1}\right] \tag{3.25}$$

$$= \sqrt{\frac{\xi(\sin(\theta) - \mu\cos(\theta))}{g}} \tag{3.26}$$

which is the well known Froude number. It means that, once the entire flow (each cell) reaches a steady state, the value of the Froude number should converge to a constant and uniform value which depends only on the slope angle and the two friction parameters of the Voellmy-Salm model. We can note, that even if the mathematical derivation remains valid for every density of the block, momentum exchanges between the layers would not conserve the Froude number convergence. Therefore, to have a correspondence between the numerical output and the mathematical analysis, momentum exchanges have to be zero, which reflect the fact that we have a constant density (not uniform!!).

Chapter 4

Voellmy-Type Mixture Rheologies for Dilatant, Two-layer Debris Flow Models

Abstract

We formulate and test different Voellmy-type mixture rheologies that can be introduced into two-layer debris flow models. The formulations are based on experimental data from the Swiss Illgraben test site as well as on mathematical constraints in steady flow conditions. In agreement with the ideas of Iverson, we show that the uniform, fixed rheological models cannot accurately represent the changing frictional resistance when debris flows undergo spatial and temporal changes in solid-fluid composition. Indeed, the experimental results of Illgraben indicate that flow friction decreases with increasing volumetric fluid concentration, however, the degree of reduction depends on both the pore-pressure and the solid particle agitation. The interplay between these processes make friction in debris flows highly nonlinear and difficult to quantify. Changing the friction according to the flow composition must be carefully executed, because it can lead to numerical instabilities, which is a recurrent problem in two-layers debris flow models. We test the different rheological formulations using a real event documented with differential topographic data collected using Unmanned Aerial Vehicles (UAVs). The model is able to reproduce the correct erosion pattern and exhibit the right density profile. The event includes de-watering at the front and deposition of sediment which cause a change from debris flow to debris flood or hyperconcentrated flow, which indicates that two completely different flow states can be modelled with a single Voellmy-type mixture rheology.

4.1 Introduction

The increasing application of two-phase debris flow models in hazard engineering [1,2,6,111,112,118] has renewed interest, and subsequently research, into the debris flow rheology problem, see Fig. 4.1. Presently debris flow calculations are performed using fixed rheologies using frictional parameters that vary strongly depending on the debris flow type [105]. This limits the predictive power of model calculations and their application in hazard engineering. The evolving behavior of debris flows is simply too complex to be modelled by a fixed rheology (with regards to space and time) that ignores spatial and temporal variations of fluid content, pore-pressure and particle agitation. Iverson [7] or more recently Hungr [129] termed the impossibility of finding a fixed rheology, the *rheology myth*, and proposed Coulomb mixture theories to model debris flows of variable solid-fluid composition.

In this paper, we investigate two Coulomb mixture theory formulations of Voellmy-type. Our use of Voellmy-type models is motivated by the fact that they are widely applied in debris flow practice (at least in Switzerland [105]) and therefore empirical parameter ranges are known. Because Voellmy-type models contain only two parameters for each layer, the total number of parameters remains small. Our primary motivation, however, is to show that improved simulation results in terms of predictive power are possible. In this work, we aim at demonstrating, using shear and normal force measurements at the Illgraben test site [107,109], that there is also a good experimental foundation for this rheological approach. We investigate the influence of rheology on debris flow composition, de-watering, entrainment and prediction of channel outbreaks, [130, 131].

The general mathematical form of the Voellmy-type mixture formulations is:

$$\vec{\tau}_i = \vec{\tau}_{\mu,i} + \vec{\tau}_{\xi,i} \tag{4.1}$$

where $\vec{\tau}_i$ denotes the frictional resistance of the i-th layer ($i=1$ stands for the mixed debris flow layer and $i=2$ for the free water layer, for more details, see section 4.2). As in the case for single-layer/layer Voellmy-type models, the frictional resistance is split into two parts: the Coulomb friction part $\vec{\tau}_{\mu,i}$ of the i-th layer and the hydraulic, velocity-dependent friction $\vec{\tau}_{\xi,i}$. Here, we adopt the Swiss convention of denoting the Coulomb friction with the greek symbol μ and the hydraulic friction with the symbol ξ. Coulomb friction depends on the normal stress N_i and is given by:

$$\vec{\tau}_{\mu,i} = \mu_i N_i \vec{e}_i \tag{4.2}$$

and $S_{\xi,i}$ is given by:

$$\vec{\tau}_{\xi,i} = \frac{g\rho_i ||\vec{v}_i||^2}{\xi_i} \vec{e}_i. \tag{4.3}$$

Where ξ_i is the turbulent friction coefficient for the layer i and $\vec{v}_i$ is the velocity of the i-th layer. The vector $\vec{e}_i$ is a unit vector along the flowing direction of the i-th layer, $\vec{e}_i = \frac{\vec{v}_i}{||v_i||}$.

To test the rheological formulations, it is necessary to implement them into a two-layer debris flow model. For this purpose, we use the approach recently proposed by Meyrat and others [132]. We choose to work with a depth-averaged model since it has been shown to accurately reproduce the spatial and temporal flow composition measured in actual debris flows at the Swiss Illgraben test station [109, 114, 115]. This includes the simulation of the measured density distribution from leading edge of the debris flow to the flow tail [132]. It contains both a free-fluid layer and mixture

Figure 4.1: *Debris flows inundated the village of Bondo, Switzerland after the Piz Cengalo rock/ice avalanche collapse in 2017.*

layer (solid - bonded fluid), and therefore allows the determination of excess pore-pressures, as well as an agitation-driven dilatancy terms arising from the shearing of the granular solid. As such, it fulfills the basic debris flow model requirements formulated by several authors including Takahashi [118] and Iverson [1, 108]. The rheological formulations presented here are formulated in general terms such that they can be applied in *any* two-layer model. Moreover, we wish to separate as much as possible the proposed rheological formulations from the specific two-layer debris flow model that we apply.

The natural state of a debris flow is unsteady, especially when considering flow in steep, twisting torrents in complex mountain terrain. Bed erosion also serves to disrupt any possibility of steady flow. Nonetheless, we decide to test the Voellmy-type mixture rheologies both in steady and unsteady conditions. Indeed, a steady-state analysis of the mixture formulations is necessary, especially to test the overall model performance (and the correctness of the numerical implementation since the model results must converge to analytically-derived steady solutions). Since steady solutions exist in most, if not all, two-layer debris flow models, the steady-state analysis facilitates a comparison between different two-layer model approaches. It also helps clarifying the underlying physics of the different mixture formulations.

In the following section, we present the governing equations of our two-layer approach. We discuss the physical ideas underpinning the model. This presentation serves to identify the friction terms in the momentum balance equations. In Section 4.3 we present the two basic rheological formulations based on pore-pressure and dilatancy concepts. In section 4.4 we investigate the
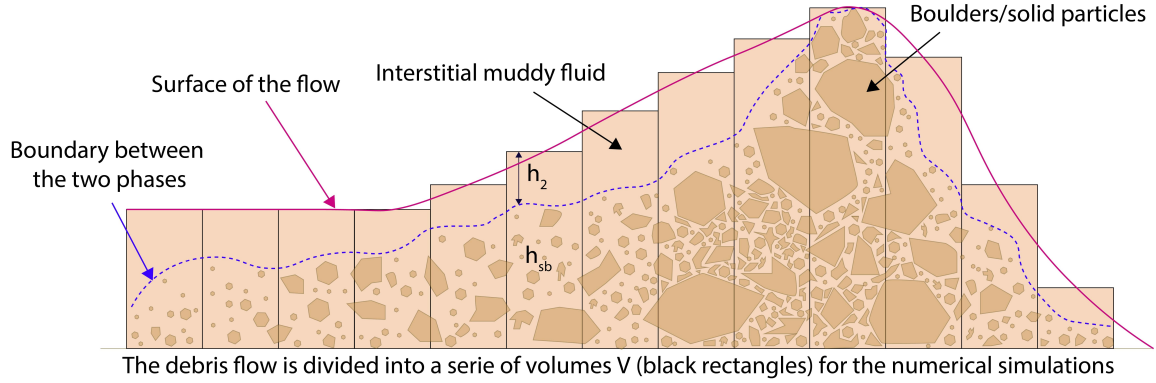
Boulders/solid particles

Interstitial muddy fluid

Surface of the flow

Boundary between
the two phases

h_2

h_{sb}

The debris flow is divided into a serie of volumes V (black rectangles) for the numerical simulations

Figure 4.2: *A sketch of the debris flow model. The flow consists of solid material in the form of boulders (granules) as well as two types of fluid. The bonded/interstitial fluid is located between the boulders and is 'fixed' to the solid. The free fluid is located above the granular solid/fluid mixture and moves independently. In the numerical simulations, the debris flow is divided into a series of volumes V (black rectangles).*

numerical stability of the proposed formulations. Documented real events simulations are found in section 4.5. The paper is rounded-off with some concluding remarks and an outlook to future work in Section 4.6.

4.2 Two-Layer Debris Flow Model with Dilatancy

We model debris flows with a two-layer, depth-averaged formulation [132], see Fig. 4.2. The debris flow contains two material components: a solid component (subscript s) consisting of coarse granular sediments (e.g. boulders, cobbles, and gravel), associated with a density ρ_s, and a fluid component (subscript f) consisting of fine sediment likely to behave as suspended sediment (e.g. sand, silt, clay), hereafter referred to as the muddy fluid content, the density of which is denoted by ρ_f.

The solid and fluid components are divided into two layers. The first layer (subscript 1) contains the granular solid material and a part of the fluid. The fluid is contained in the interstitial space between particles and is assumed to be bonded to the solid particles. The second layer (subscript 2), is formed by the fluid which can flow independently from the first layer. The total mass per unit of area (all the quantities in the following are defined per unit area A) of the debris flow M is the sum of the mass of layer 1 (solid particles and inter-granular fluid) and mass of layer 2 (free fluid),

$$M \;=\; M_1 + M_2 = M_s + \underbrace{M_{f,1} + M_{f,2}}_{M_f} = \rho_s h_s + \rho_f \underbrace{(h_{f,1} + h_{f,2})}_{h_f} \tag{4.4}$$

where $h_{f,1}$ and $h_{f,2}$ represent the amount of fluid in the first (interstitial fluid) and second (free

50

fluid) layer, respectively, and h_f defines the total amount of fluid in the flow. We write h_s instead of $h_{s,1}$ because the solid always belongs to the first layer only. $M_{f,i} = \rho_f h_{f,i}$ is the fluid mass contained in the i-th layer. These assumptions lead to a system of three depth-averaged mass balance equations,

$$\frac{\partial h_1}{\partial t} + \vec{\nabla} \cdot (h_1 \vec{v}_1) = \left[\frac{\rho_f}{\rho_s}\right] Q_f + \left[\frac{\rho_e}{\rho_s}\right] E \qquad \text{solid and inter-granular fluid} \qquad (4.5)$$

$$\frac{\partial h_{f,2}}{\partial t} + \vec{\nabla} \cdot (h_{f,2} \vec{v}_2) = -Q_f \qquad \text{second layer, free fluid} \qquad (4.6)$$

$$\frac{\partial h_{f,1}}{\partial t} + \vec{\nabla} \cdot (h_{f,1} \vec{v}_1) = Q_f + \left[\frac{\rho_e - \rho_f}{\rho_f - \rho_s}\right] E \qquad \text{inter-granular fluid} \qquad (4.7)$$

where $\vec{\nabla}$ is the divergence operator in Cartesian coordinates. The vectors $\vec{v}_1$ and $\vec{v}_2$ represent the depth-averaged velocity of the first and second layers, respectively. For notation purposes, we do not denote the depth-averaged quantities differently in the following of this paper. The right-hand side of the inter-granular fluid and free fluid equations contains the term Q_f [132], which is the mass exchange rate between the inter-granular and free fluid driven by dilatant actions in the solid matrix (see following). The equations relevant for the first phase (eq. 4.5 and 4.7) also contain the erosion rate, denoted by E. The density ρ_e characterizes the density of the entrained mass. In order to compute the erosion rate E, we began with the model introduced in [40, 50] which is based on careful field measurements [75] and well-documented events. The model was subsequently adapted for the two-layer model. In the modified model the erosion rate E is no longer uniform (as in [40, 50]), but a function of the flow composition. If E_s represents the erosion rate for a purely solid flow and E_f for a completely fluid layer, the erosion rate E is expressed as follows:

$$E = (1 - \phi_f)E_s + \phi_f E_f \qquad (4.8)$$

where ϕ_f is the volumetric fluid fraction of the first layer, defined as:

$$\phi_f = \frac{h_{f,1}}{h_s + h_{f,1}} \qquad (4.9)$$

The term E is absent in Eq. 4.6, because the second layer i.e., the free fluid, cannot entrain solid material by definition. Solid material must be entrained by the first layer. Unlike in [130, 131] in which the erosion rate is a function of the flow depth and velocity, the solid and fluid erosion rates E_s and E_f are constant and uniform. However, the maximum potential erosion depth is computed from the shear stress, [40, 50], which depends on the flow height, velocity, and composition.

We emphasize that the pseudo-variable h_1 does not represent the physical height of the first phase (the one that a sensor would measure). This variable is introduced to simplify the mass and momentum conservation equations. The pseudo-height h_1 is defined as the sum of the solid and bonded fluid mass (equal to first layer mass), normalized by the solid density ρ_s:

$$h_1 = h_s + \frac{\rho_f}{\rho_s} h_{f,1} \qquad (4.10)$$

This relation can be found by noting that the total mass of the first layer M_1 can be expressed as the sum of the solid material M_s and the interstitial fluid mass M_b. As the heights h_s and $h_{f,1}$

represent the height of the solid and inter-granular fluid components in the first layer, respectively (these quantities can be considered as the solid and fluid volumetric parts of the debris flow mass), we find that,

$$M_1 \;=\; M_s + M_b = \rho_s h_s + \rho_f h_{f,1} = \rho_s \underbrace{\left(h_s + \frac{\rho_f}{\rho_s} h_{f,1}\right)}_{h_1} = \rho_1 \underbrace{(h_s + h_{f,1})}_{h_{sb}} \tag{4.11}$$

$$M_2 \;=\; \rho_f h_{f,2}. \tag{4.12}$$

where $h_{sb} = h_s + h_{f,1}$ represents the physical height of the first layer and $M_2 = M_f$ the mass of the second layer, see Fig. 4.2. All the fluid which flows above the first layer is considered free, and subsequently it can escape the matrix of solid particles, allowing the debris flow to de-water. As the solid particles settle, and the interstitial space between particles collapses, fluid can escape from the solid part of the flow.

At first instance, the division of masses using a pseudo-height h_1 appears cumbersome. h_1 is however associated with a constant and uniform density ρ_s (Eq. 4.10), in contrast with h_{sb} which is associated with the 'real' first layer density ρ_1 which evolves with the dilatant action of the solid matrix. Therefore, using h_1 simplifies the momentum balance equations by the density. They are given for the two layers [123, 124], by:

$$\partial_t(h_1 \vec{v}_1) + \vec{\nabla} \cdot \left(h_1 \vec{v}_1 \otimes \vec{v}_1 + \frac{g h_1^2}{2} I\right) + g h_1 \vec{\nabla}\left(b + \frac{\rho_f}{\rho_s} h_{f,2}\right) \;=\; -\frac{\vec{\tau}_1}{\rho_s} + \frac{\rho_f}{\rho_s} \vec{P} \tag{4.13}$$

$$\partial_t(h_{f,2} \vec{v}_2) + \vec{\nabla} \cdot \left(h_{f,2} \vec{v}_2 \otimes \vec{v}_2 + \frac{g h_{f,2}^2}{2} I\right) + g h_{f,2} \vec{\nabla}\left(b + h_{sb}\right) \;=\; -\frac{\vec{\tau}_2}{\rho_f} - \vec{P}. \tag{4.14}$$

Where the vectors $\vec{v}_1$ and $\vec{v}_2$ represent the depth-averaged velocity of the first and second layers, respectively and $b := b(x, y)$ denotes the bottom topography. The symbol $\otimes$ denotes the tensor product and I is the two-dimensional unity matrix. The left side of Eqs. 4.13 and 4.14 is the total variation of the momentum with respect to time, including the effect of gravitation and the influence of each layer on the other [123, 124]. The right side represents the change in momentum due to external forces (excluding gravitation). $\vec{\tau}_i$ corresponds to the shearing forces acting on the i-th layer (we divide it by the density ρ_s for the first layer and ρ_f for the second one, because Eq. 4.13 and 4.14 are defined per unit of density). Different Voellmy-type mixture models for the shearing stresses $\vec{\tau}_i$ are provided in the next chapter. Contrarily to [53, 133], we do not account for any momentum production or softening of the basal topography due to erosion. Consequently, erosion is not directly present in the momentum balance equations, Eqs. 4.13 and 4.14. However, it influences the mass balance and the mixture layer composition, which governs the shear resistance of the flow. Therefore, although we do not explicitly consider momentum production, entrainment changes the entire flow dynamics.

The vector $\vec{P}$ is the rate of momentum exchange associated with the mass exchange Q_f,

$$\vec{P} = \begin{cases} Q\vec{v}_2 & \text{if the first layer is dilating} \quad \dot{h}_{sb} > 0 \\ Q\vec{v}_1 & \text{if the first layer is collapsing} \quad \dot{h}_{sb} < 0. \end{cases} \tag{4.15}$$

The mass exchange Q_f is a result of the dilatant actions of the solid particles in layer 1. Under interactions with the rough bed of the channel, the solid matrix can expand its volume during flowing, leading to different flowing configurations, associated with different densities (see left sketch of Fig. 4.3). Note that, even if the solid mass is conserved, according to Eq. 4.11, the first layer density can vary if the inter-granular fluid concentration evolves:

$$\rho_1 = \frac{\rho_s h_s + \rho_f h_{f,1}}{h_{sb}} = (1 - \phi_f)\rho_s + \phi_f \rho_f. \tag{4.16}$$

When the flow is at rest, the first layer is in the so called co-volume configuration, the height of which is denoted h_0, which corresponds to the configuration where the solid matrix is completely collapsed, see right sketch on Fig. 4.3. However, potential energy is required to rise up the center of mass of the solid matrix. We call it the configurational energy, V_D, and it can be expressed, considering buoyancy, as:

$$V_D = \underbrace{[\rho_s - \rho_f] h_s}_{\text{buoyant mass}} g_z \underbrace{\frac{1}{2}[h_{sb} - h_0]}_{z} \tag{4.17}$$

where z denotes the vertical displacement of the center of mass, from the collapsed configuration to a dilated configuration and gravity g_z is the slope-perpendicular gravity component. Changes in the center of mass of the solid matrix implies changes in the void space. When the void space increases, free fluid fills the additional space between the particles. Conversely, if the solid matrix collapses, interstitial bonded fluid is transformed into free fluid and will be squeezed out of the first layer. Therefore, changes in the solid matrix center of mass will always be accompanied by fluid mass exchanges between the interstitial bonded fluid and the free fluid. These exchanges are denoted Q_f and are responsible for the evolution of the flow composition.
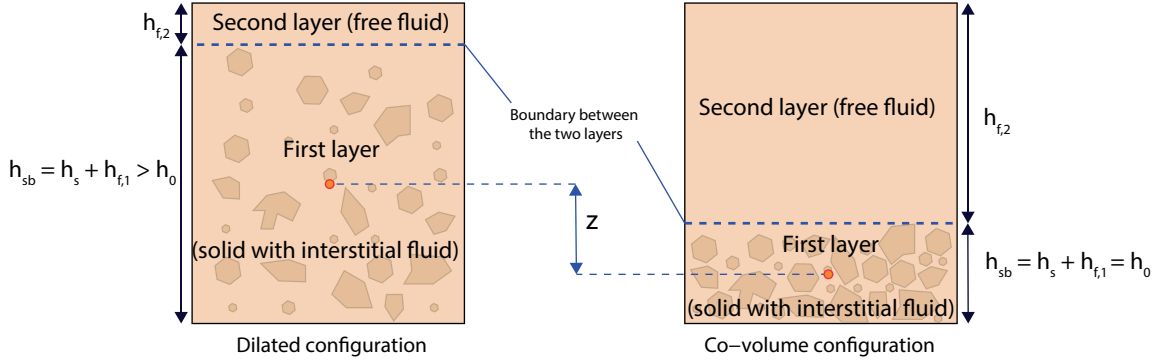

Figure 4.3: *Sketch of two different debris flow configurations, containing overall of the same amount of solid and fluid mass. The left panel is in a dilated configuration, occurring while flowing. The right configuration is the reference configuration, called the co-volume configuration, typically occurring when the flow is at rest. The different heights and further physical parameters are described in [132]. We define three variables associated with the solid mass, h_s, h_0 and h_{sb}. The height h_s is the volume of the solid particles in the flow, h_0 represents the reference height of the non-dilated mass, we call it the co-volume (It is different from h_s, because we consider that, even in the non-dilated configuration, the void space is not zero), whereas h_{sb} represents the dilated height of the solid mass, section 4.2. We refer to h_0 as the co-volume, in an analogy to Van der Waals work on non-ideal gasses with large molecules and cohesion [119].*

We postulate that the configurational energy V_D is governed by a simple production (parameter α) and decay (parameter β) term [132]

$$\frac{\partial D}{\partial t} + \vec{\nabla} \cdot (D\vec{v}_1) = \alpha \dot{W}_f - \beta D. \tag{4.18}$$

The quantity W_f represents the shear work. That is, the change in the energy of configuration V_D (dilatation) is directly related to the shear work, in accordance to Reynolds [78]. The parameter α defines the fraction of the shear work that produces a dilatation, whereas the parameter β defines how quickly the dilatation collapses in the absence of shear, due to energy dissipation caused by shearing between particles. The balance between the production of V_D and its decay defines the degree of saturation in the debris flow, as this defines the amount of void space (inter-granular water) in the moving solid. For more details, the reader is referred to [132].

4.3 Voellmy-type Mixture Rheologies

The two parameters Voellmy formulation is popular in natural hazard mitigation because the Coulomb friction determines the debris flow runout, as it defines the critical slope angle θ at which the flow begins to decelerate $\tan \theta = \mu$ [105]. The hydraulic friction ξ defines the steady flow speed of the movement. Thus, with only two parameters we can define the approximate runout distance and steady flow velocity. Default values for single-layer/layer debris flows are known (approximately μ=0.20 and ξ=200 m/s^2). However, these values can change significantly in practical case-studies, because they depend on the fluid content of the debris flow and torrent conditions, such as grain size distribution. With the aim of reducing the range of possible values of the two Voellmy parameters, we now introduce two models, the *Voellmy Mixture model* (denoted as **VM**), section 4.3.1 and the *Voellmy Mixture Model including Pore Pressure Effects* (denoted **PP**), section 4.3.2. In these models, the rheology is not uniform and constant anymore but evolves with the flow composition. Before going to the details of the different models, here we make some general comments:

The rheological formulation of any two-layer/phase model with an entirely fluid layer/phase (the free fluid one here) has to ensure the following consistency conditions:

$$\lim_{\phi_f \to 1} S_{\mu,1}(\phi_f) = S_{\mu,2} \qquad \text{and} \qquad \lim_{\phi_f \to 1} S_{\xi,1}(\phi_f) = S_{\xi,2} \tag{4.19}$$

where ϕ_f is the volumetric fluid fraction, as defined in eq. 4.9. These limit conditions ensure the following: if the first layer density becomes close to the density of the second layer (meaning that it contains no solid material), the frictional shear forces acting on the first layer must be similar to the second layer. The density of the first layer can vary, from a rocky density ($\approx$ 2000-2200 kg/m^3, debris flow front) to the density of the muddy fluid ($\approx$ 1000-1300 kg/m^3, debris flow tail). Therefore, if the first layer acquires the density of the muddy fluid (for example, at the tail of the flow), the consistency condition enforces a rheological uniformity between the layers. Because bed entrainment can suddenly change the solid and fluid concentrations of the debris flow anywhere, the consistency condition physically constrains the effects of bed erosion on the evolving flow properties of the debris flow.

The assumption that the debris flow rheology is not constant and uniform but evolving with the

flow composition is supported by the experimental data from Illgraben. The Illgraben debris flow test site (Fig. 4.4) is located near Leuk, Canton Wallis, Switzerland [107,114,115]. Since 2005, the Illgraben torrent has been instrumented with a rectangular force plate (area A=8m^2) that measures shear and normal stresses at the base of a passing debris flow. A laser sensor located above the plate measures the total debris flow height h as the flow passes over the plate. The force plate is located at the end of a 5 km long torrent (in orange on Fig. 4.4) that has an average slope of 5° at the downstream end of the channel at the location of the force plate. The torrent is fed by a large (9.5 km^2), steep catchment zone (in blue on Fig. 4.4), which supplies the channel. The Illgraben sub-catchment supplies most of the water and sediment, whereas the Illbach catchment supplies mainly water [109].

From the normal stress and height measurements, it is possible to compute the flowing density ρ or equivalently the fluid volume fraction ϕ_f, [132]. It is therefore possible to investigate the link between the flow composition and the intensity of the shear forces. The ratio between the shear and the normal stress (S/N) is a good representation of the shear force intensity. In Fig. 4.5, the ratio S/N is plotted as a function of the volumetric fluid concentration (which is simply equal to $100 \times f$). In this figure, we can see clearly that the ration S/N depends strongly on the flowing fluid saturation.

In order to take into account the effects of the evolving debris flow composition in the first layer on its rheology, we define four rheology coefficients: ξ_s and μ_s which are relevant for the densest configuration, i.e the co-volume configuration while μ_f and ξ_f if the flow is composed of fluid only. As the second layer is always composed only by fluid, its coefficients are uniform and constant, i.e. $\mu_2 = \mu_f$ and $\xi_2 = \xi_f$.

4.3.1   Voellmy Mixture Model (VM Model)

One method to account for the reduction of friction with increasing fluid concentration, Fig. 4.5, is to express the rheology coefficients μ and ξ as a linear function of fluid fraction ϕ_f. Therefore, we assume that the shearing coefficients are given by the weighted average of μ_s and ξ_s of the flow composition. Formally,

$$\mu_1(\phi_f) \quad = \quad \frac{h_s \mu_s + h_{f,1} \mu_f}{h_s + h_{f,1}} = (1 - \phi_f)\mu_s + \phi_f \mu_f \tag{4.20}$$

$$\xi_1(\phi_f) \quad = \quad \frac{h_s \xi_s + h_{f,1} \xi_f}{h_s + h_{f,1}} = (1 - \phi_f)\xi_s + \phi_f \xi_f. \tag{4.21}$$

Eq. 4.20 combined with Eq. 4.1, 4.2 and 4.3, satisfy the consistency condition given by Eq. 4.19. In general we assume that for the muddy fluid (i=2),

$$\mu_2 \quad = \quad \mu_f = 0 \tag{4.22}$$

$$\xi_2 \quad = \quad \xi_f \tag{4.23}$$

Thus, we have for the mixture stresses

$$\vec{\tau}_{\mu,1} = \mu_1(\phi_f)N_1\vec{e}_1 = \mu_s g_z \rho_1 h_s \vec{e}_1 \qquad \text{and} \qquad \vec{\tau}_{\mu,2} = 0 \tag{4.24}$$
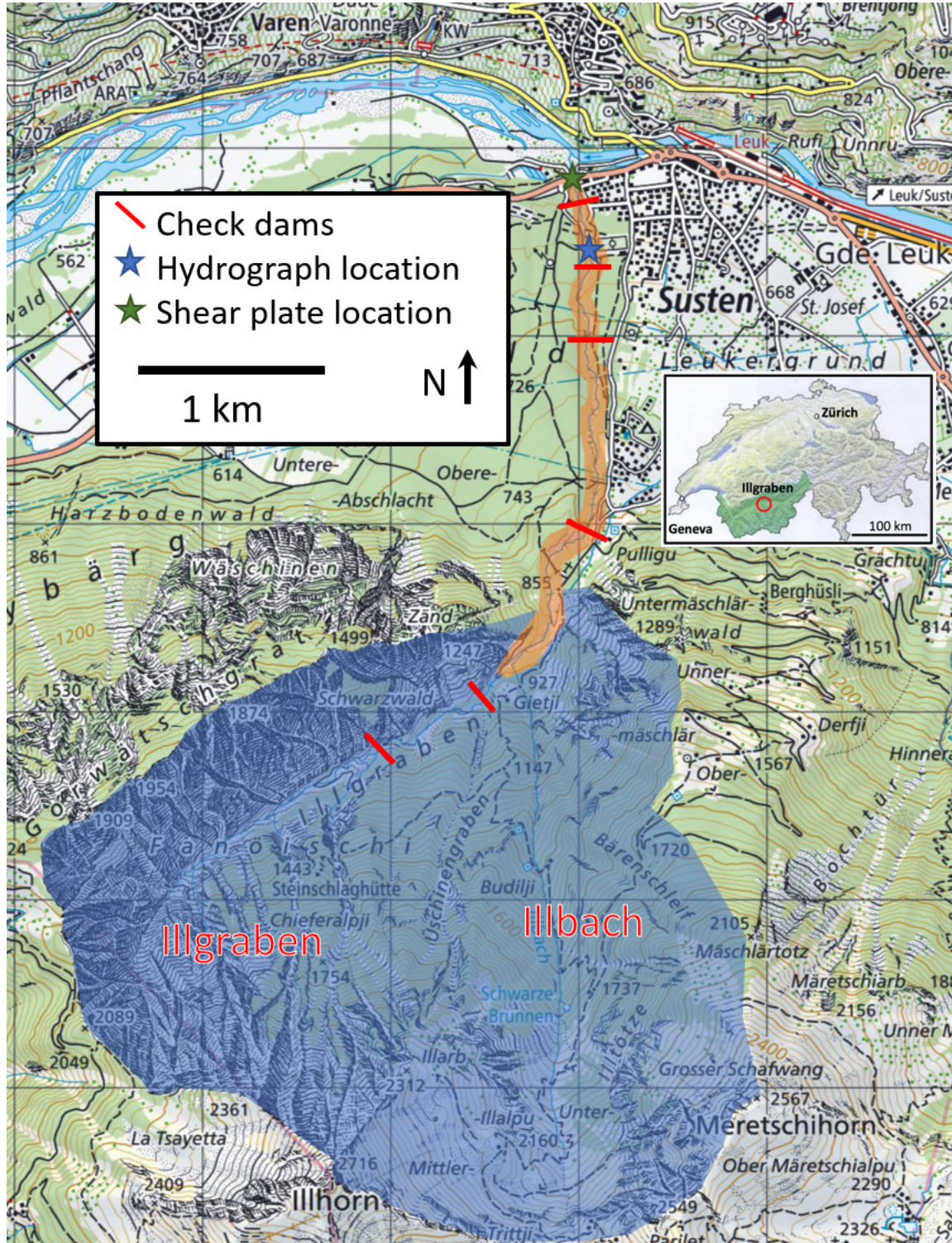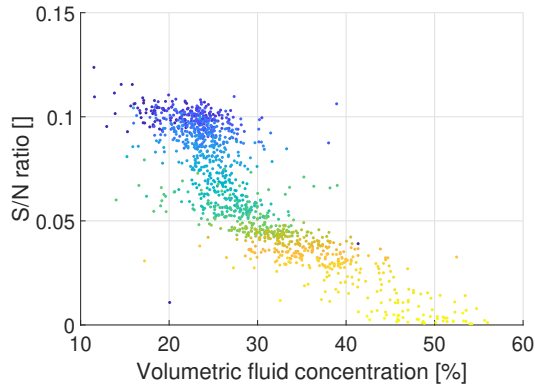
Figure 4.4: *Map of the Illgraben test site. The catchment zone is colored in blue, while the channel is drawn in orange. The check dams are also shown by red lines. The blue star represents the starting point of the hydrogaph, used for the numerical simulation, and the green star is the location of the force plate. The original map can be found in [107].*
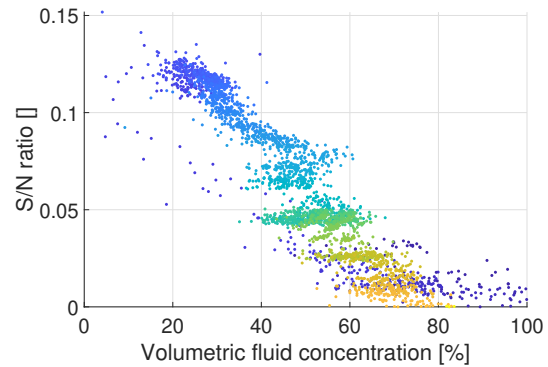
(a) *Event of the 2nd August 2005*
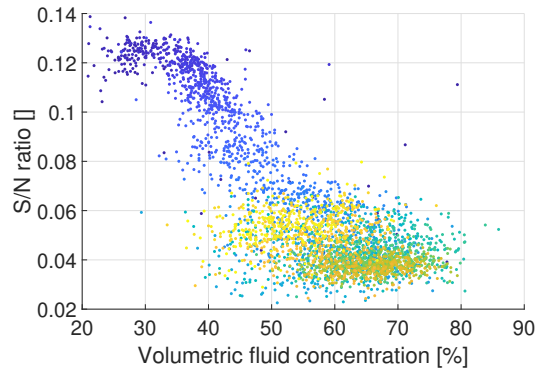
(b) *Event of the 28th July 2006*
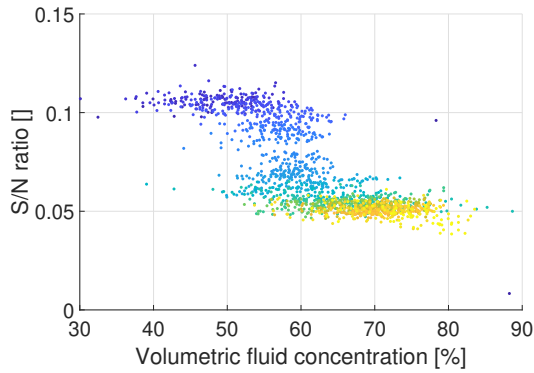
(c) *Event of the 29th July*

(d) *Event of the 29th July 2013*

Figure 4.5: *Experimentally measured shear-normal stress ratio (S/N) as a function of the measured fluid volumetric concentration for four different debris flow events. Each dot represents an experimental measurement. The color provides additional temporal information, the blue represents the debris flow front and the yellow the tail.*

and

$$\vec{\tau}_{\xi,1} = \frac{g\rho_1 ||v_1||^2}{\xi_1(\phi_f)}\vec{e}_1 \qquad \text{and} \qquad \vec{\tau}_{\xi,2} = \frac{g\rho_f\rho_f ||v_2||^2}{\xi_f}\vec{e}_2. \tag{4.25}$$

4.3.2 Voellmy Mixture Model including Pore Pressure Effects (PP Model)

Effective stress and pore pressure concepts have been applied to model debris flow motion [1,6,108, 134]. if we let p be the fluid pressure, then in depth-averaged models the effective stress N_{eff} is given by the difference between the normal pressure and the fluid pressure,

$$N_{eff} = N - p \tag{4.26}$$

On the assumption that the pressure p is hydrostatic, the Coulomb part of the shear stress is,

$$\vec{\tau}_{\mu,1} = \mu_1 N_{eff}\vec{e}_1 = \mu_1 \left[N - p\right]\vec{e}_1 = \mu_s(\rho_s - \rho_f)g_z h_{sb}\vec{e}_1 \quad \text{with} \quad p = \rho_f g_z h_{sb}. \tag{4.27}$$

Here note that we do not include the normal stress induced by free fluid, i.e. $N_f = \rho_f g_z h_{f,2}$, in the computation of the pore pressure. It is not required because N_f should be added to both normal stress (N) and pore fluid pressure (p). Therefore, the free fluid normal stress contribution will vanish in the computation of $\vec{\tau}_{\mu,1}$ in Eq. 4.27 as only the subtraction of N by p is relevant. Another interesting feature of the model is that the consistency condition given by eq. 4.19 is satisfied if and only if $\mu_2 = 0$. Therefore,

$$\vec{\tau}_{\mu,2} = 0. \tag{4.28}$$

In this formulation, Eq. 4.21 is still valid, therefore, the ξ-terms are the same as in the preceding approach,

$$\vec{\tau}_{\xi,1} = \frac{g\rho_1 ||v_1||^2}{\xi_1(\phi_f)}\vec{e}_1 \qquad \text{and} \qquad \vec{\tau}_{\xi,2} = \frac{g\rho_f\rho_f ||v_2||^2}{\xi_f}\vec{e}_2. \tag{4.29}$$

4.4 Steady State Solutions

The purpose of this section is to derive steady-state solutions of the two-layer debris flow equations with dilatancy. Because steady-states represent the balance between the driving and resisting forces acting on the debris flow body, the solutions are dependent on the different rheological formulations. For mixture models, the rheological formulations are, in turn, a function of the fluid fraction ϕ_f. In our model the fluid fraction is dependent on the available pore space between the churning rocks and boulders in the debris flow body and therefore intimately related to flow dilatancy. The demonstration that steady state solutions even *exist* for a two-layer mixture model for a specific fluid volume fraction ϕ_f is important. It indicates that states of steady flow are associated with states of constant flow density (zero changes in dilatancy and then in pore space) and therefore unchanging propagation speeds. The reverse statement appears also to be true: with changing speeds, the flow densities cannot remain constant, and therefore the evolution of debris flow speed, from the tail to the front of the debris flow, are always related to a change in flow density (and therefore a change in fluid volume fraction ϕ_f). Changing flow compositions are always accompanied by mass transfers between the bonded and free fluid components. The rheological mixture models must

allow for steady states to exist, if only theoretically. Steady-state results can also be used to test the numerical implementation of the mixture models.

In this section we study the mathematical solution of a sliding rigid block along an inclined plan with a constant slope angle θ. The block has a fluid volume fraction ϕ_f. A steady state has many properties, one of them is that the acceleration is zero i.e. $\dot{\vec{v}} = 0$. For our purpose, we study the flow in a single direction x. Then the equation of motion of a sliding block is, with respect to the axis $\hat{e}_x$ and $\hat{e}_z$,

$$\text{along} \quad \hat{e}_x \quad \rightarrow \quad mg\sin(\theta) - S = ma = m\dot{v} = 0 \tag{4.30}$$

$$\text{along} \quad \hat{e}_z \quad \rightarrow \quad -mg\cos(\theta) + N = 0 \tag{4.31}$$

with S the shear force in the x-direction. This implies,

$$\text{along} \quad \hat{e}_x \quad \rightarrow \quad mg\sin(\theta) - \frac{\rho_1 g v^2}{\xi} - \mu N = ma = 0 \tag{4.32}$$

$$\text{along} \quad \hat{e}_z \quad \rightarrow \quad -mg\cos(\theta) + N = 0 \tag{4.33}$$

where $\vec{v}$ is the velocity of the center of mass (i.e. always parallel to the slope direction $\hat{e}_x$). Note that as S and N are stresses, indicating that the mass m in Eq. 4.30 and 4.32 is defined per unit of the basal area A, i.e. $m = \rho_1 h_1$. This is not a problem for the numerical simulation and for this mathematical analysis, since the basal area A is in both cases constant and uniform. Note that in Eq. 4.32, μ and ξ have to be changed for $\mu(\phi_f)$ and $\xi(\phi_f)$ for the VM Model and N has to be changed for N_{eff} for the PP Model. The Froude number of the flow block is a function of the rheological formulation. It can be written for the VM Model (Fr_l) and the PP Model (Fr_p) as,

$$Fr_l = \frac{v}{\sqrt{gh}} \quad = \quad \sqrt{\frac{\xi(\phi_f)(\sin(\theta) - \mu(\phi_f)\cos(\theta))}{g}} \qquad \text{VM Model} \tag{4.34}$$

$$Fr_p = \frac{v}{\sqrt{gh}} \quad = \quad \sqrt{\frac{\xi(\phi_f)(\sin(\theta) - \mu\cos(\theta) + \mu\frac{\rho_f}{\rho_1})}{g}} \qquad \text{PP Model} \tag{4.35}$$

with $\mu(\phi_f)$ and $\xi(\phi_f)$ given by Eq.4.20. The entire derivation is presented in [132].

To test the model implementation we compare calculated and analytical Froude numbers. For the simulations, we use a smooth plane with a constant angle, this way the flow can reach a steady state. A block release is used to initiate the flow and erosion is not taken into account. In order to compute the convergence of the numerical simulations to the analytical derivation, we first compute the absolute value of the relative difference between the numerical outputs and the mathematical value of the Froude number, averaged on each cell containing mass, we call it 'percentage difference'. If F_n and F_a denote the numerical and analytical value of the Froude number, and if N is the number of cells containing material:

$$\text{percentage difference} = \frac{100}{N} \sum_{i=1}^{N} \frac{|F_{n,i} - F_{a,i}|}{F_{a,i}} \tag{4.36}$$

with i running over the cells containing mass. In Fig. 4.6a (VM Model) and 4.6b (PP Model), we plot the percentage difference as a function of the time. It is clear that the numerical outputs
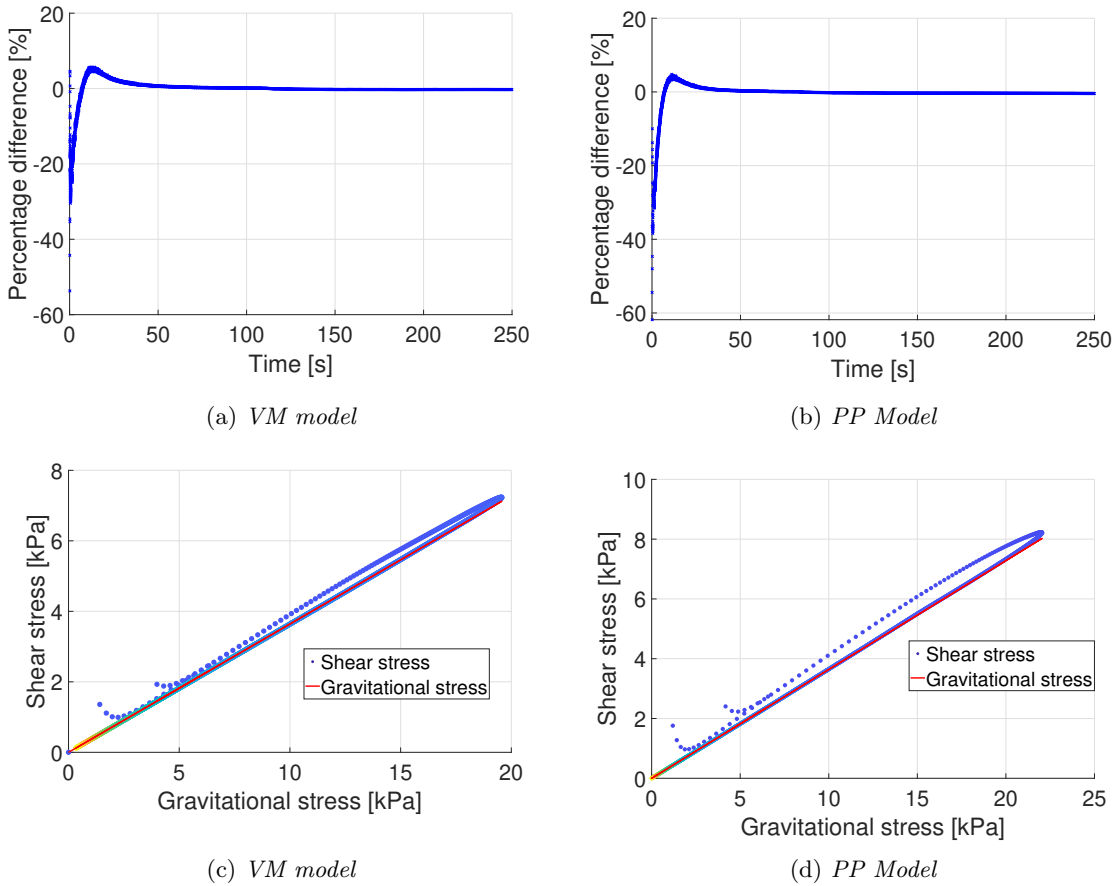
(a) *VM model*

(b) *PP Model*

(c) *VM model*

(d) *PP Model*

Figure 4.6: *a) (VM Model) and b) (PP Model) Convergence of the simulation results to the analytical value of the Froude number (Eq. 4.34, figure 4.a and Eq. 4.35, figure 4.b) in a steady state. An averaging is performed over the cells containing mass, which means that the entire flow is in a steady state (except the really front, see next). c) (VM Model) and d) (PP Model) According to Eq. 4.37, in a steady state, the shear stress (colored circles) does not depend on the rheological formulation and is equal to the gravitational stress (red lines). The color represents the time, the front is in blue and as we move towards the tail as the color becomes yellow, see Fig. 4.7. The very first part of the flow (blue markers) is not exactly in a steady state, due to numerical effects related to the shock-wave form of the front. The simulations are done on a smooth plane with constant angle, using a block release.*

converge to the analytical value. Another aspect of a steady state is that the gravitational force is in an exact balance with the shearing force, independent of the formulation of the shearing processes we consider. This fact is depicted in Fig. 4.6c (VM Model) and Fig. 4.6d (PP Model). The red line represents the gravitational stress and the colored markers (the blue markers represent the front of the flow while the yellow markers represent the tail, see Fig. 4.7. plot c) and d) depict the shearing stresses. Except for the leading edge of the flow, the two curves match perfectly. This difference in the front is linked with numerical effects due to the shock-wave form of the front of the debris flow.

This equivalence between shearing and gravitational stress (or force) in a steady state can be written in mathematical terms as follow:

$$S = mg\sin(\theta) \tag{4.37}$$

which implies that the derivative of S with respect to time is zero. Therefore, the shear work rate

$\dot{W}_f$, in Eq. 4.18, can be written as:

$$\dot{W}_f = \frac{d}{dt}(Sx) = \dot{S}x + S\dot{x} = Sv = mg\sin(\theta)v \tag{4.38}$$

Where x represents the position of the flow block on the x-axis. Using the expression for $\dot{W}_f$, eq. 4.18 can be solved exactly. We find in the limit of $t \to \infty$:

$$V_D = \frac{\alpha}{\beta}\dot{W}_f = \frac{\alpha}{\beta}Sv = \frac{\alpha}{\beta}mg\sin(\theta)v \tag{4.39}$$

combining with Eq. 4.17 and defining $\Gamma = \frac{\alpha}{\beta}$, we obtain, for the steady-state flow height of a dilatant debris flow:

$$h_{sb} = \underbrace{h_0}_{\text{non-dilated height}} + \underbrace{2\Gamma\frac{m}{(\rho_s - \rho_f)h_s}\tan(\theta)v}_{\text{Dilatancy}} \tag{4.40}$$

Note that this formula is valid for both rheological formulations. The difference between them is in the steady state's value of the velocity, given by Eq. 4.34 and 4.35. In our model, we have an additional assumption, which is that a solid matrix cannot dilate if there is no more free fluid above, i.e. $h_{f,2} = 0$. Therefore, Eq. 4.40 becomes:

$$h_{sb} = \begin{cases} h_0 + 2\Gamma\frac{m}{(\rho_s - \rho_f)h_s}\tan(\theta)v, & \text{if } h_{f,2} > 0. \\ h_s + h_{f,1}, & \text{if } h_{f,2} = 0. \end{cases} \tag{4.41}$$

Here, $\Gamma = \frac{\alpha}{\beta}$ is the ratio between the production α and the decay β of the configurational energy, see Eq. 4.18. We can see that in a steady state, only the ratio between them is important and β governs the time needed to approach a steady state. This formula holds for the two formulations. It is related to the fact that in a steady-states, the shearing forces are always equal to the driving forces, independently of their specific expressions.

In Fig. 4.7 we show the convergence of the numerical height to the analytical solution. In plot Fig. 4.7a (VM Model) and Fig. 4.7b (PP Model) we plot the absolute value of the relative difference between the numerical and the analytical value of the height, Eq. 4.36. We can see that the difference approaches zero after some time, which represents the fact that both values of the height coincide. In plot Fig. 4.7c (VM Model) and Fig. 4.7d (PP Model), we choose a location in the domain sufficient distanced from the release zone to ensure the flow can reach a steady state. We compare the calculated height from the numerical code and the analytical steady state solution. Both the numerical and analytical curves match well, which indicates that the flow has indeed reached a steady state in its height [1]. Steady states are indeed associated with no changes in density. Note that we assume that we always have enough fluid to fill the void space between the churning particles. Analytically, we do not consider the influence of one layer on the other. However, this effect is taken into account when we perform the numerical simulations. The fact that the numerical output converges to the analytical value shows that these effects are negligible. Therefore, the analytical derivation can be considered as valid even for a dilatant, two-layer model with solid-fluid interactions.
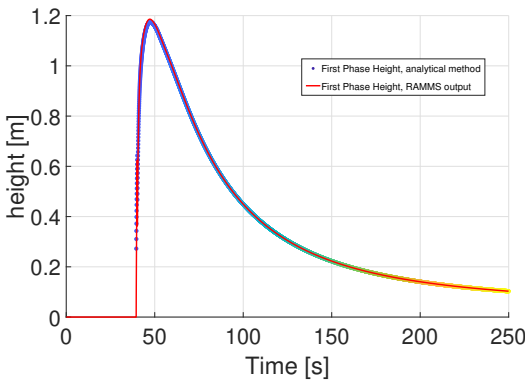
[1] At the leading edge of the debris flow (approx. The first 10 s), the two curves do not match perfectly, according to Fig. 4.6 c and d
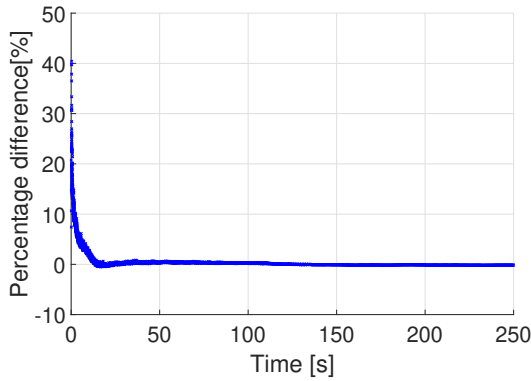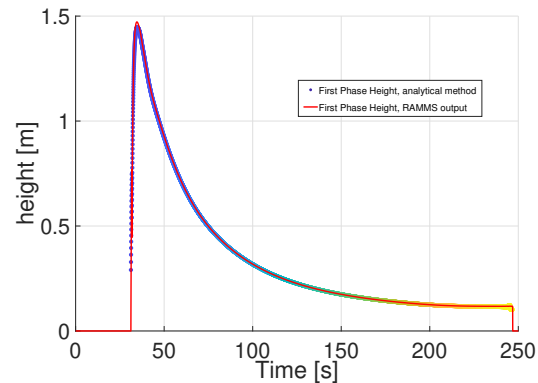
(a) *VM model*
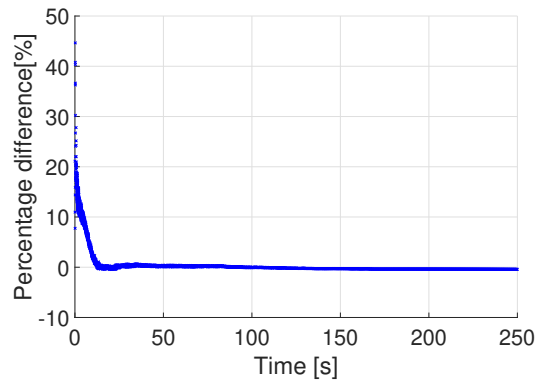
(b) *PP Model*

(c) *VM model*

(d) *PP Model*

Figure 4.7: *a) (VM Model) and b) (PP Model) Convergence of the simulation results to the analytical value of the height of the debris flow (Eq. 4.40) in a steady state. An average is done on each cell containing mass, which means that the entire flow is in a steady state and it is assumed that we always have enough fluid to filled the void space in between the particles. c) (VM Model) and d) (PP Model) Flow height on a particular cell taken in the middle of the flow. The red line represent the numerical outputs and the colored markers are obtained with Eq. 4.40. The simulations are done on a smooth plane with constant angle, using a block release.*

4.5   Case Study: Ritigraben, Switzerland

After checking the mathematical consistency of the computer implementation, we now model a recent event at a different catchment. For this purpose we choose the torrent of Ritigraben, located between Gräschen and St Niklaus, in Wallis, Switzerland[2]. The torrent is 3.75 km long with an elevation drop of approximately 1500 m (Fig. 4.8). At the top of the Ritigraben torrent lies a rock glacier, which provides sediments to the upper torrent catchment. Subsequently, sizeable debris flow events occur almost every year. Many studies have already been performed at this debris flow site, [135, 136, 137, 138, 139].

The event of the 7th of August 2021 is of particular interest to us because digital elevation models (DEM) were obtained two days before and two days after the event. This allows to estimate the mass balance for this particular debris flow [140], accurately, constraining the initial and entrainment volumes. To compute the volume eroded by the debris flow, the longitudinal profile of the torrent has been divided into several bins of 20m length each [50, 141], see Fig. 4.9. For each bin, the eroded and deposited material was computed by taking the difference between the two digital elevation models. A map of the erosion (negative difference, red) and deposited (positive difference, blue) volumes can be made (Fig. 4.9). We find that the total eroded volume reached approximately 10'000 m^3. In some parts of the torrent, no erosion or deposition was observed. It should be noted, that even if the entire eroded volume can be computed, it is still not possible to define separately the volume of solid-fluid entrained.

To initiate the flow, we assume a block release of 1000 m^3 (650 m^3 of solid and 350 m^3 of fluid) [140] and a hydrograph, to simulate the river flow in the channel. As the event occured just after a heavy rainfall, the river discharge, normally low, cannot be neglected, especially for an event of this size. Video recordings were used to estimate the fluid volume, see video. We use a 7 m^3/s discharge rate of river fluid. We performed two sets of simulations, with the VM model and the PP model. When we compare the two simulations, they were always performed with the same value of the model parameters. A list of the parameter values can be found in table 4.1, section 4.8.

Fig. 4.10a depicts the numerical distribution of erosion along the debris flow channel. Fig. 4.10b, represents the erosion computed for each of the bins shown on Fig. 4.9. The red line represents the measured data (drone flights), while the blue (VM Model) and green (PP Model) curves are obtained from numerical simulations. Both models provide similar results; both are in good agreement with the field data. Both models give a total erosion volume close to 10′000 m^3, which is the one obtained from the filed data. Note that we allowed erosion in our model only in the torrent sections where erosion was observed by field observations.

Figs. 4.11a (VM Model) and 4.11b (PP Model) show the simulated spatial evolution of the flow density. For both rheological formulations, the front (red region) has the highest density, ≈ 2000 kg/m^3, which is consistent with the fact that it is composed of large blocks, while the tail (blue region) has the smallest density ≈ 1300 kg/m^3, which is the density of a muddy fluid. Even if the computed front and tail densities are similar for both rheological models, the spatial evolution differs slightly. This fact will be discussed in Section 4.6.

The spatial variation of the friction coefficients μ and ξ is shown in Fig. 4.12. Figs. 4.12a (VM Model) and 4.12b (PP Model), resp. 4.12c (VM Model) and 4.12d (PP Model), show a decrease in μ as we go from the front to the tail for an erosion density of 2000 kg/m^3 (a and b) and 1800
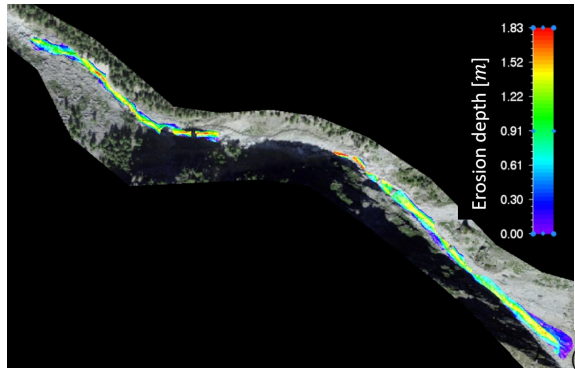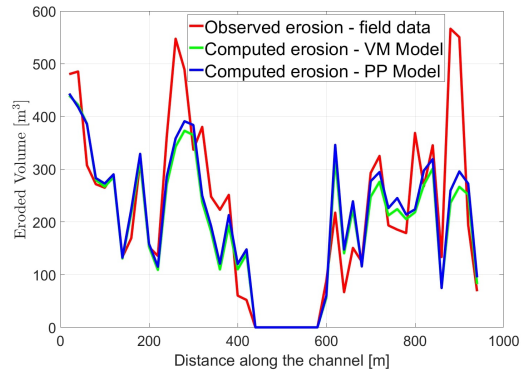
---

[2]46°11'15.8"N 7°49'20.1"E

Figure 4.8: *Map of the Ritigraben debris flow site. The original map can be found in [140]*

Figure 4.9: *Maps of the bins used to compute the erosion height. The colors represent the entrain-ment(red)/deposition(blue) heights. The original map can be found in [140]*


(a) *Erosion pattern obtained with the VM Model.*

(b) *Eroded volume per bins as a function of the po-sition of the bins toward the channel. The red curve is obtained from field data, the blue one with the VM model and the green line from the PP Model. The ero-sion computed with both models is in good agreement with the measurements.*
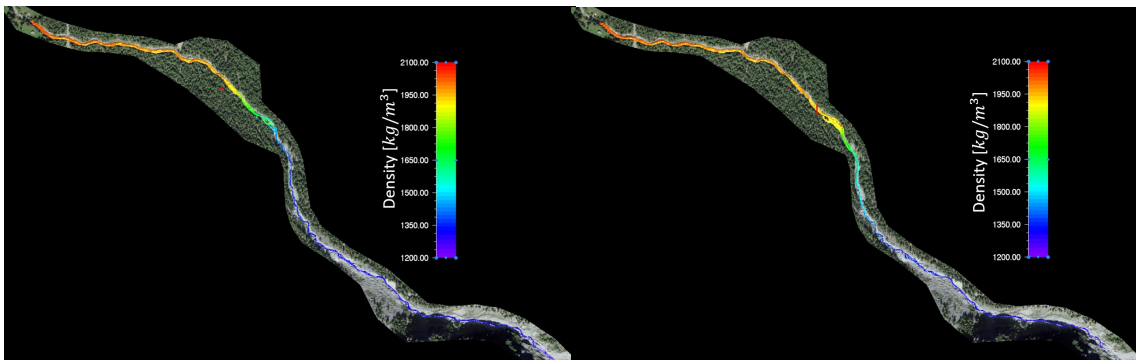
Figure 4.10

(a) *VM model*

(b) *PP Model*

Figure 4.11: *Spatial evolution of the flow density for a) the VM model and b) the PP Model. As we know for real events, the density varies from a large value ($\approx 2000 kg/m^3$) in the front to the value of the muddy fluid density ($\approx 1300\ kg/m^3$) as we go toward the tail. The front and tail value of the density are the same for both models, however their spatial evolution differs slightly.*

65
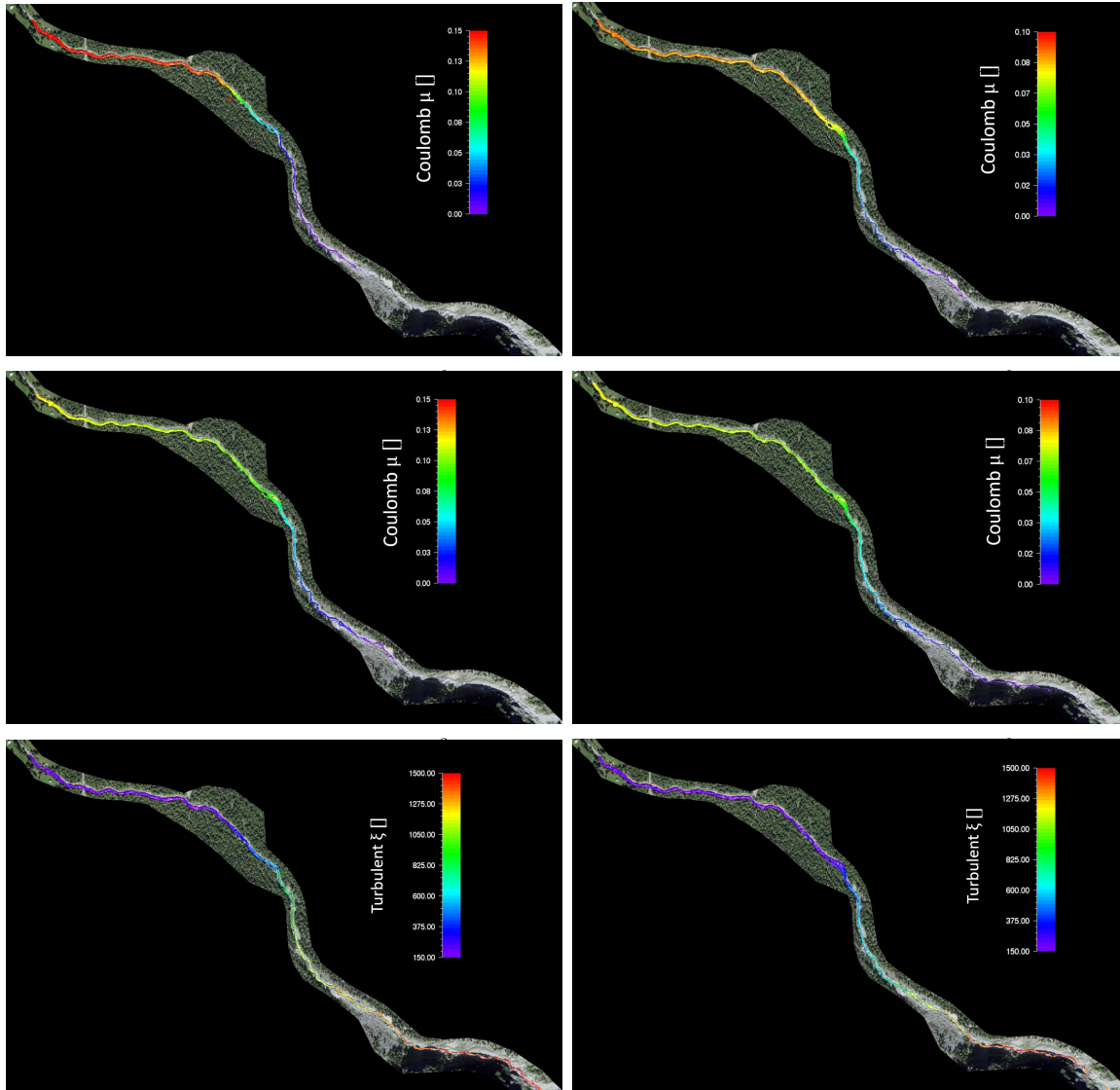
(e) *VM model, $\rho_e = 2000 kg/m^3$* (f) *PP Model, $\rho_e = 2000 kg/m^3$*

Figure 4.12: *Spatial evolution of the shearing coefficients μ and ξ. Panel a) (VM Model) and b) (PP Model) show a decrease of μ from the front to the tail. The erosion density is $2000 kg/m^3$. Panel c) (VM Model) and d) (PP Model) are the same as a) and b) but for an erosion density of $1800 kg/m^3$. One can see clearly that the value of μ depends strongly on the erosion density. Therefore, the erosion does not only influence the mass balance of the flow but the entire flow dynamics. Panel e) VM Model and f) PP Model represent the increase in ξ, which induces a decrease in the turbulent friction, from front to tail of the flow.*

(a) *VM model, location 1*   (b) *PP Model, location 1*

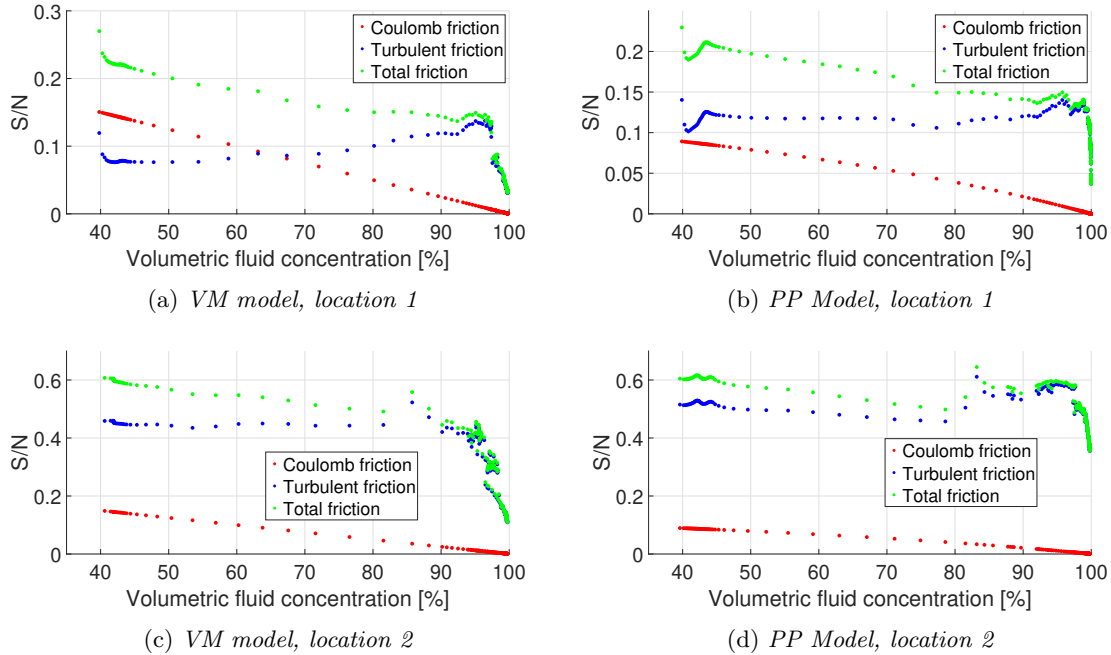(c) *VM model, location 2*   (d) *PP Model, location 2*

Figure 4.13: *Ratio of the total shear stress (green), the Coulomb shear stress (red) and the turbulent shear stress (blue) to the normal stress, as a function of the volumetric fluid content. This is done for two different locations, see Fig. 4.8 (top and bottom) and for the two models (left and right). Location 1 (plots a and b) is in the flat part of the channel ($\theta < 10°$) and then comparable to the Illgraben measurement, while Location 2 (Panel c) and d)) is in the steep part of the bottom channel ($\theta \approx 30°$).*

kg/m^3 (c and d, respectively). The values of μ given by both models are significantly different in the front but become closer as we go towards the tail. We find that the value of μ strongly depends on the erosion density. The spatial evolution of ξ is depicted in 4.12e (VM Model) and 4.12d (PP Model). As expected, the value of ξ increases when going from front to tail. A clear decrease in the shearing stresses is observed from front to tail. This is due to the decrease in density, and then an increase in fluid content of the flow, from front to tail. Note that ξ is given by Eq. 4.21 for both model and μ by Eq. 4.20 for the VM model and by the ratio of the Coulomb shear stress, Eq. 4.27, to the normal stress for the PP Model.

In Fig. 4.13, the ratio of the total shear stress (green), the Coulomb shear stress (red) and the turbulent shear stress (blue), to the normal stress, is plotted as a function of the volumetric volume concentration for two different locations in the debris flow torrent (Fig. 4.8). The first point (plots a and b) is located in the flat part of the channel ($\theta < 10°$) while the second point (plots c and d) is located in the steep part of the bottom channel ($\theta \approx 30°$), see Fig. 4.8.

In Fig. 4.14, the maximum solid (4.14a) and fluid (4.14b) heights in the run-out zone are shown. We can see that even if both fluid and fluid flow together in the steep channel, it is not the case anymore when the flow reaches the run-out zone. Indeed, the core of the flow stops and the fluid content is washed-out the solid matrix and can continue to flow downwards the valley. This is what is called by some authors phase separation, [142].
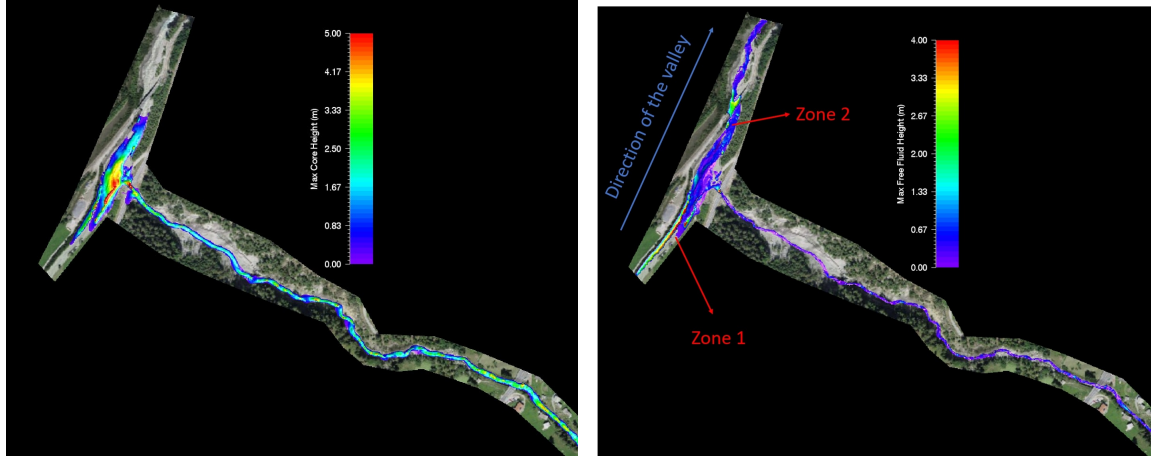
(a) *Maximum solid height in the run-out zone*   (b) *Maximum fluid height in the run-out zone*

Figure 4.14: *Maximum solid (a) and fluid (b) heights in the run-out zone. The solid stops at the end of the channel, while the fluid can dewater and continue to flow downstream (zone 2), or be holed by the core of the debris flow which acts as a dam (zone 1). The simulation is performed with the the VM model, but similar results can be obtained with the PP Model.*

4.6   Discussion and Conclusions

Measurements from the Illgraben debris flow test site indicate that frictional resistance depends on the fluid-solid composition of the flow (Fig. 4.5). Non-changing flow compositions are found at the front (high solid concentration of boulders and rocky debris moving with quasi-constant velocity) and at the tail (high concentration of fluid, also moving close to a constant velocity). These flow compositions persist over long periods of debris flow motion and mathematically represent steady flow conditions. A challenging problem in debris flow science is to model both flow compositions within the same model framework (and the same debris flow), without ad-hoc changes of resistance parameters. For this purpose, we have investigated the use of Voellmy-type mixture theories implemented within multi-phase/layer debris flow models.

In a first step, it was necessary to demonstrate the steady state properties of a two-layer debris flow model. The rheological mixture models implemented within the framework of two-layer simulation tools must allow for the possibility of two entirely different flow compositions *in the same debris flow*. Fig. 4.7 is of particular importance because it reveals the fact that the flow body can indeed reach a constant density in steady state, in which no more mass or momentum exchanges between the layers are possible. We therefore demonstrated that constant steady state velocities (given by the friction parameters) are associated with constant flow heights and therefore constant flow densities. A particularly important formula is,

$$h_{sb} = \begin{cases} h_0 + 2\Gamma \frac{m}{(\rho_s - \rho_f)h_s} \tan(\theta)v, & \text{if } h_{f,2} > 0. \\ h_s + h_{f,1}, & \text{if } h_{f,2} = 0 \end{cases} \tag{4.42}$$

which relates the total flow height of the debris flow to the slope angle, flow velocity and parameters governing granular dilatation. This formula provides us with a method to *experimentally* determine the ratio between two important model parameters governing the production α and decay β of the configurational (dilatational) energy, $\Gamma = \frac{\alpha}{\beta}$. Because in our model formulation the interstitial

fluid content is controlled by the granular dilatations of the solid phase, the frictional resistance is intimately related to this ratio. In the calculation example of a real debris flow we applied the value $\Gamma = 1$ s.

The primary difference between the two different mixture models is the dependency of the solid Coulomb friction parameter on the flow density (eqs. 4.24 and 4.27). As the flow density (solid composition) varies from front to tail of the debris flow we expected the two formulations to provide strongly varying results. Surprisingly, the numerical differences are small. We note that the difference in density between the debris flow front (≈ 2500 kg/m^3) and tail (≈ 1200 kg/m^3) is between 1300-1500 kg/m^3. Interestingly, this range is numerically close to the muddy fluid density ρ_f (≈ 1300-1500 kg/m^3). Therefore, the difference between the two approaches will only be in the front of the flow, where the density, used for the VM model, is much larger. Assuming the use of the same values of all friction parameters (μ_s, μ_f, ξ_s and ξ_f), the computed shear stresses will be larger at the front of the flow for the VM Model in comparison to the PP Model. This fact can be identified in Fig. 4.12a and Fig. 4.12b (erosion density 2000 kg/m^3) and Fig. 4.12c and 4.12d (erosion density 1800kg/m^3). These results illustrate the spatial change in μ, for two different erosion densities for both the VM and PP Models. For a given erosion density, the VM Model exhibits larger values of μ in the front than the PP Model but these values become similar at the tail. Note that the turbulent friction decreases analogously for both models when going from front to tail because the decrease is governed by the same relationships.

For both mixture formulations the calculated density values at the leading edge of the flow are similar. They appear to be governed almost entirely by the erosion density. The calculated densities at the tail of the flow are also similar, approximately a value corresponding to a muddy fluid. However, the spatial evolution of the calculated densities differs strongly between the limit and PP Models. For the VM Model, the density decreases faster behind the front. This implies that the solid fraction is more concentrated at the front in comparison to the PP Model. Due to its larger friction, the front acts a bit more like a dam in the VM Model. Consequently, the flow height in the front is slightly larger. This fact could have important impacts when simulating overflows and channel outbreaks. In Fig. 4.15, we depict two overflow cases. Even if this overflow is relatively small, the overflow is nonetheless significantly larger for the VM Model than for the PP Model. Therefore, even if the general behavior is similar, minor differences in flow height (and streamwise composition) could play a significant role in hazard analysis.

Our model comparison to the Illgraben measurements also helped identifying a possible problem with the experimental observations. To model the measurements it was necessary to apply very high values of the ξ-friction. These high ξ- values (low friction values) cannot be applied to model debris flows because they lead to unrealistically high flow velocities. In Illgraben, the shear stress is measured with a shear plate [109,114]. However, the turbulent ξ- stress depends on the roughness of the terrain [109,125]. The force plate consists of smooth steel without any additional roughness [125] and is smoother than the natural sediment bed of the channel. Therefore, it is possible that we do not measure the entire shear stress because one part of the turbulent ξ-stress is missing in the measurements, as if the flow was sliding over the plate. This hypothesis is supported by the fact that small values of the shear stress are measured for non-zero values of the normal stress (Fig. 4.5).

In Fig. 4.13, we plot the ratio of the shear to the normal stress, as a function of the volumetric
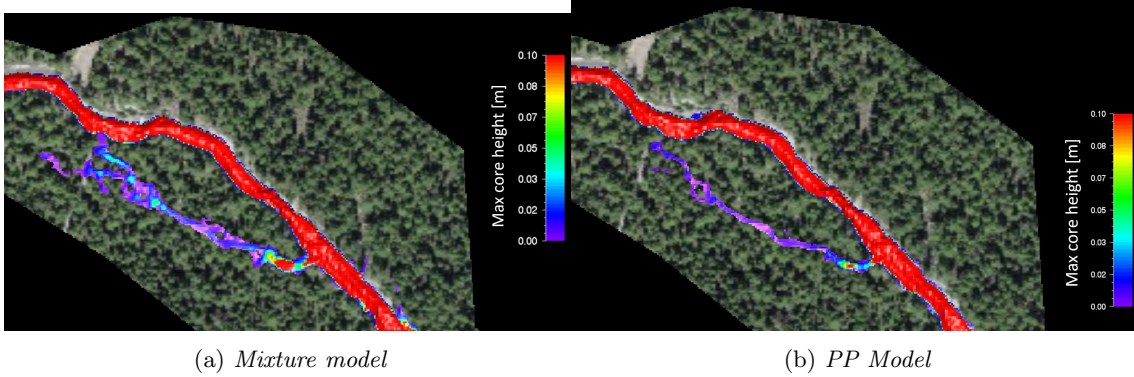
(a) *Mixture model*   (b) *PP Model*

Figure 4.15: *Overflow obtained with the numerical simulation. Despite the small size of this overflow, one can see that the mixture model predicts larger overflow than the PP Model.*

fluid concentration at two different track locations (i.e. the same plot as Fig. 4.5) for both mixture models, see Fig 4.8. The first location is on an almost flat slope, comparable to the location where the data from Illgraben are obtained (less than 10° steep), while the second location corresponds to steeper terrain (around 30° steep). These plots show that the decrease of the total friction (green dots) is because of the decrease in Coulomb friction (red dots). The turbulent ξ-friction (blue dots) is almost constant. Note that volumetric fluid concentration ≥ 95, correspond to negligible flow heights and therefore should be interpreted with precaution. This can be understood by referring back to the steady state analysis. When reducing the shear, the velocity increases until the flow reaches a steady state. This leads to the quasi constant behaviour of the turbulent term with increasing fluid content. This relationship (Fig. 4.5) is similar to the behavior of the Coulomb stress (red dots) in Fig. 4.13. These results strengthen the hypothesis that when measuring the shear stress experimentally, it might be possible that a large part of the turbulent stress normally acting on the flow is absent, due to the smoothness of the force plate. In future, shear plates should be artificially roughened to represent real terrain.

The Ritigraben event of the 7th August 2021 was of particular interest because drone flights were performed before and after the event. The pre-event flight was carried out two days before the event; the post-event flight was performed two-days after the debris flow. Bed erosion and deposition could therefore be quantified. Fig. 4.10b depicts the calculated erosion pattern using the two different mixture models. The general erosion pattern is quite similar for both formulations and can catch the general behaviour of the field data, which is remarkable, regarding the fact that we never take into account the local structure of the bed channel, which is obviously of major importance in erosion processes. The entire eroded volume ($\approx 10'000\text{m}^3$) is computed correctly using standard erosion parameters. The importance of erosion can be understood by comparing Fig. 4.12a with 4.12c and 4.12b with 4.12d. The difference between them are the erosion density (2000 kg/m^3 for 4.12a and 4.12c and 1800 kg/m^3 for 4.12b and 4.12d). It is clear that the shearing processes are strongly dependent of the erosion density. Therefore, the erosion does not only influence the mass balance of a debris flow, but its entire flow dynamics, [53,130,131,133], through the erosion density, which can modify the solid/fluid ratio of a debris flow. For instance, the simulation performed with an erosion density of 1800 kg/m^3 reaches the run-out zone more than one and half minutes earlier than the simulation executed with a density of 2000 kg/m^3 (on a complete flowing time of approximately 10 minutes).

Another aspect of the model is the ability to simulate dewatering and phase separations. Indeed,

when the flow reaches the run-out zone, it decelerates and the energy coming from the shear work is not sufficient anymore to maintain the solid matrix in a dilated configuration. Therefore the flow collapses and deposits (friction increases), as shown in Fig. 4.14a. During the collapse of the mixture layer, interstitial water is squeezed out and transformed into free fluid, which can escape from the solid matrix (Fig. 4.14b). If the free fluid is ejected downstream of the deposit (zone 2 on Fig. 4.14b) it continues to flow downward. If the fluid is squeezed out upward from the deposit, (zone 1 on Fig. 4.14a), it is stopped by the deposit which acts like a dam. This can be of major importance when simulating debris flow events. Indeed, in Ritigraben and many other torrents, the risk of a lake formation upstream the solid deposit which can potentially release afterward and inundate the valley downstream has been widely studied. Therefore, the possibility to be able to simulate these lake formations with our model could help in the future hazard analysis.

To summarize, there exists a strong interaction between the streamwise evolution of a debris flow and the modelling of the frictional resistance. In debris flow hazard mitigation, the problem is often to choose a consistent set of parameters that govern the frictional resistance. In many case studies, however, a single set of fixed rheology parameters is not able to predict accurately the motion of a debris flow because the streamwise evolution of debris flow structure is not considered. Therefore, large modelling uncertainties remain. Fortunately, we have measurement data from the Illgraben test site which allows us to test the application of Voellmy-type mixture models within the framework of layered debris flow approaches. We have demonstrated that a single set of mixture parameters can represent the entire behavior of a debris flow, provided the model formulation tracks the fluid and solid components separately. Although we can envision the application of more complicated rheological models in the future, our results suggest that Voellmy-type models can be applied as a first step, reducing the uncertainties of practitioners considerably.

4.7   Acknowledgments

4.8   Annexe

*For the definitions of these values, refer to [40, 50].

Name	Symbol	Unity []
Solid density	ρ_s	2500 kg/m^3
Fluid density	ρ_f	1300 kg/m^3
Solid Coulomb coefficient	μ_s	0.2
Fluid Coulomb coefficient	μ_f	0.0
Solid turbulent coefficient	ξ_s	100 m/s^2
Fluid turbulent coefficient	ξ_f	1000 m/s^2
Configurational energy production	α	0.15
Configurational energy decay	β	0.15 $1/s$
Steady state coefficient	$\Gamma = \frac{\alpha}{\beta}$	1 s
Entrained density	ρ_e	1800 or 2000 kg/m^3
Solid erosion rate	E_s	0.03 m/s
Fluid erosion rate	E_f	0.005 m/s
Critical shear stress	τ_c*	0.75 kPa
Critical shear coefficient	$\frac{d\tau}{dz}*$	-0.08 m/kPa
Maximum erosion depth	e_m*	2 m
Gridsize	Δx	1 m

Table 4.1: List of the parameter values used for the simulation

Chapter 5

Simulating Glacier Lake Outbursts (GLOFs) with a Two-phase/layer Debris Flow Model Considering Solid-Fluid Flow Transitions

abstract

Glacier lake outburst floods (GLOFs) initiate with the rapid outburst of a glacier lake, endangering downstream populations, land, and infrastructure. The flow initiates as a mud flow; however, with the entrainment of additional solid material, the flood will often transform into a debris flow. As the run-out slope flattens, the coarse solid material deposits and the flow de-waters. The flow transforms back into a muddy, hyperconcentrated flow of fine sediments in suspension. These flow transitions change the flow composition dramatically and influence both the overall mass balance and flow rheology of the event. In this paper, we apply a two-phase/layer model to simulate flow transitions, solid-fluid phase separations, entrainment, and run-out distances of glacier lake outburst floods. A key feature of the model is the calculation of dilatant actions in the solid-fluid mixture which control flow transitions and phase separations. Given their high initial amount of fluid within the flow, GLOFs are sensitive to slope changes inducing flow transitions, which also implies changes in the flow rheology. The changes in the rheology are computed as a function of the flow composition and do not need any adaptation by ad-hoc selection of friction coefficients. This procedure allows the application of constant rheological input parameters from initiation to run-out. Our goal is to increase the prediction reliability of debris flow modelling. We highlight the problems associated with initial and boundary (entrainment) conditions. We test the new model against the well-known Lake 513 (Peru, 2010), Lake Palcacocha (Peru, 1941) and Lake Uchitel in the Aksay Valley (Kyrgyzstan) GLOF events. We show that flow transition modeling is essential when studying areas that have significant variations in slope.

5.1   Introduction

A longstanding problem in hazard engineering in mountainous regions is to accurately predict the possible inundation area of glacier lake outburst floods (GLOFs) [23, 24, 25, 26, 27, 28, 29]. These are gravity-driven mixtures of water and granular sediments that can exhibit a wide range of different flow behaviors, depending on the initial (release) and boundary (entrainment) conditions, as well as on the terrain topography which controls the onset of solid deposition in the run-out zone and de-watering inducing subsequent flooding downstream [33, 34]. GLOFs are a growing hazard due to the increasing amount of lakes forming close by retreating glaciers [33, 143]. They are also very sensitive to changing climatic conditions including extreme rainfall events, sediment accumulations and increasingly unstable slope conditions caused by ice melt and permafrost warming and thawing [24, 28, 31, 32]. Because GLOFs can travel extreme distances, often in the order of magnitude of tens of kilometers [29, 34], they can cause extensive damage in populated areas with little warning [25].

The main difficulty in accurately predicting the travel velocity and run-out of GLOFs is that there is considerable uncertainty in the fluid/solid composition of a single event. The fluid and solid contents of a GLOF event can vary dramatically, from around 10% for a mud flow to more than 60% for a granular debris flow [144, 145], see Fig. 5.2. Often a GLOF will undergo flow transitions (Fig. 5.2) by depositing solid material on flatter slopes to turn into a flood, or eroding solid material on steeper slopes to turn into a debris flow [34]. Flow transitions tend to maximize GLOF run-out, but are difficult to model because they involve the interplay between flow rheology, sediment entrainment and terrain topography.
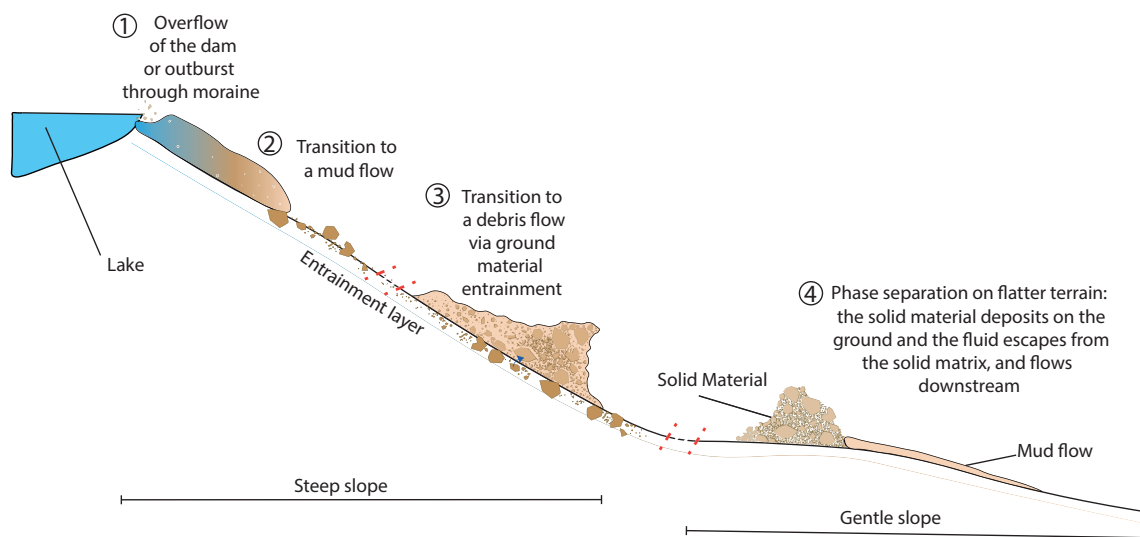

Figure 5.1: *Typical flow regime transitions during a GLOF event. The flow is initially a mud flow that can transform into a debris flow with the erosion of solid debris. If the slope becomes flatter, for example, in the run-out zone, the core of the debris flow deposits and stops. The fluid can separate from the solid matrix and continues to flow downstream in the form of a muddy or hyperconcentrated flow, [144]. If the slope becomes steeper, the entire process might occur again. The red dashed lines in the figure (between stages 2-3 and 3-4) indicate a potentially large distance between the different flow regimes, where flow transitions could occur again depending on the sediment availability and terrain topography.*

The inherent variability of flow regimes represents one of the largest sources of uncertainties

in the modeling of GLOFs, with critical implications for hazard management. This idea was first formulated by Iverson [7] who formulated the idea that the diversity of flow regimes cannot be modeled by a simplistic, single component flow rheology as the *rheology myth*. Even if the rheology of a specific flow regime (see Table 5.2, [145]) is relatively well parameterized, the neighboring flow regimes, differing only in fluid and solid content, can require an entirely different parameterization. A common feature of this phenomena is the wide range of Coulomb friction values needed to model the correct run-out distance in practical case studies [72, 73, 105], see Fig. 5.2. This observation is well supported by real-size debris flow measurements at the Swiss Illgraben test site, which show a wide variation of Coulomb friction values and an explicit dependency of the basal shear on the fluid concentration in the flow [132, 146]. Modern three-dimensional numerical schemes couple finite-strain elastoplasticity models to the conservation equations for mass and momentum in a relatively simple manner [45, 46]. This combination allows for the set up of extremely complex events with a limited need for parameter calibration [42]. However, this family of models is still in the development phase and is currently far away from practical applications from practitioners and authorities. It appears that the search for an accurate numerical model for GLOFs and other saturated granular flows, begins with the introduction of a numerical model that can reproduce the flow composition and its complex spatio-temporal variability, not only from initiation to run-out, but also from the leading edge to the tail of the flow.
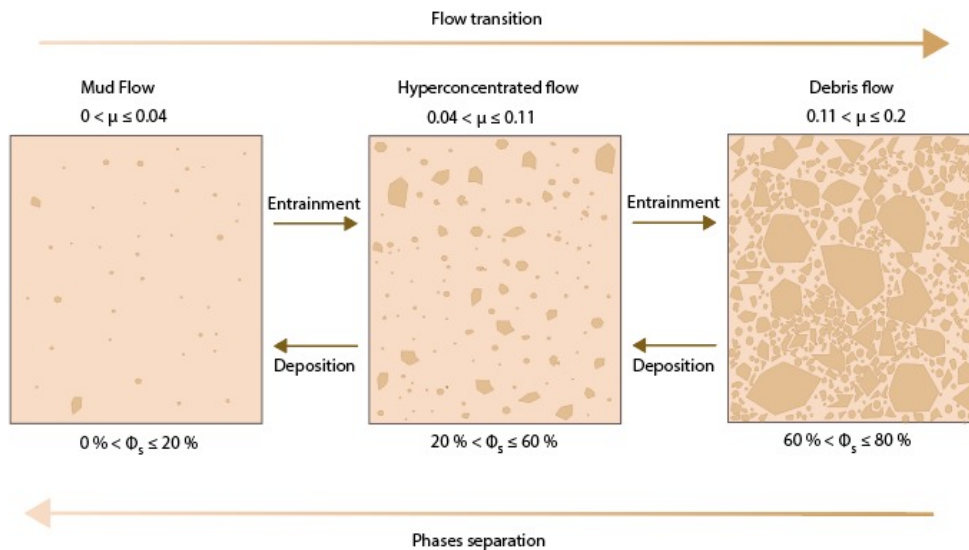

Figure 5.2: *Different flow types and their corresponding solid concentrations (ϕ_s) and rheologies (μ, [72, 73, 105]). The corresponding values of ξ are not given, because they are still not well constrained.*

The purpose of this paper is to apply a numerical model to simulate flow transitions and phase separations observed in three well-known GLOF case studies (Lake 513, Lake Palcacocha, and Aksay Valley). These flow transitions are responsible for the long-range flow mobility of the mass movements. To this end, we must address the entire complexity of GLOF dynamics, including

release conditions, flow rheology, entrainment and long-distance flow over complex terrain. Unlike many existing models that use a Darcy-like approximation to compute the fluid velocity [1, 2, 3, 5], we formulate a two-phase/layer model that contains an independent fluid phase in order to model dewatering and subsequent flooding. The Darcy approximation can be considered valid only for flows with high solid concentration, which is not necessarily the case when for GLOF-type events. Models which do not use a Darcy-like approximation to simplify the fluid momentum conservation equation [6, 147] are confronted with the mathematical problem of computing the momentum transfer between the solid and the fluid phases. Such approaches require the introduction of additional free parameters (up to three for instance, in the case of r.avaflow, [6]), which are difficult to calibrate and, therefore, problematic to use by practitioners. To overcome these problems, we adopt the method developed by Meyrat et al., [132, 146]. We first calculate flow dilations in the matrix of coarse granular sediments as a function of the basal shear stress and the volumetric solid concentration. Based on this, we predict the fluid mass that exists in the interstitial pore space between the solid, granular debris. Solid flow dilations induce fluid mass transfers between the solid and fluid layers. These mass exchanges are associated with interlayer momentum transfers. We show that this entire procedure can be modeled with only one additional free parameter, Γ, see table 5.6, [132], which controls the mean dispersion/contraction time of the dilatant configuration. This parameter is calibrated by back-calculating natural events to maximize the accuracy of the results.

To test the model, we analyze three GLOF events. The first two events are the outburst floods of the Lake 513 in 2010 and the Lake Palcacocha in 1941, both located in Peru. Lake 513 experienced a major GLOF in 2010, when a 450,000 m^3 rock-ice avalanche impacted the lake, causing severe damages along the GLOF trajectory and in the city of Carhuaz [47, 148]. The well-known Lake Palcacocha outburst in 1941 destroyed a large part of the city of Huaraz [37, 56]. The third event is the outburst flood of the Uchitel Lake in the Aksay valley in Kyrgystan [69, 149]. All three events are well described in the literature [47, 56, 69, 148, 150, 151, 152], providing us with valuable information and field data to validate, overturn and evaluate the model results. The literature, supported by observations, indicates that all three events underwent flow regime transitions.

Before describing the model equations, we must address the salient problem of bed erosion. In GLOF events, the initial release volume may represent only a small fraction of the total volume – sometimes only 10 % ([140, 153]). This indicates the important role of erosion in predicting long-distance GLOF run-out. Flow regime transitions are dependent on the entrainment and deposition processes, coupled with the evolving head-tail structure of the event. Thus, we enter into a complex, mechanical feedback loop between debris flow structure, governed by rheology and mass balance (difference between entrainment and deposition). Erosion processes strongly depend on the internal solid concentration and, therefore, on the flow structure, which clearly depends on the availability of solid debris, and therefore erosion. In the past, such complexity was modeled by ad-hoc adjustments to the flow rheology (for example, by changing the friction coefficients along the flow path, see Table 5.2). Although we perform an *a posteriori* analysis with event back-calculations, our motivation is to establish a well-defined and general set of parameters for debris flows that undergo flow regime transitions with entrainment.
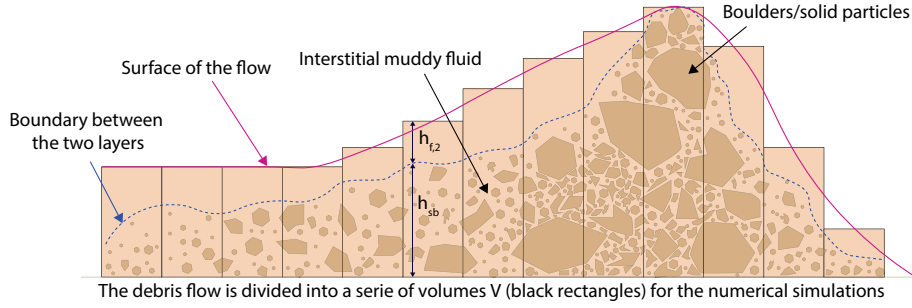
Figure 5.3: *Debris flow model. The flow consists of solid material in the form of boulders (granules) as well as two types of fluid. The bonded/interstitial fluid is located between the boulders and is fixed to the solid. The so-called free fluid is located above the granular solid/fluid mixture and can move independently.*

5.2 Model Definitions and Equations

We model debris flows with a two-dimensional, depth-averaged shallow water formulation. The model consists of two material components: a solid component (subscript s) consisting of coarse granular sediments (e.g., boulders, cobbles, and gravel) associated with a density ρ_s, and a fluid component (subscript f), hereafter referred to as the muddy fluid content, whose density is denoted by ρ_f, Fig. 5.3. The fluid component consists of water supersaturated with fine sediments that behave as suspended sediments (e.g., sand, silt, clay). Many models, for example r.avaflow, [6], treat coarse and fine sediments separately. In our formulation, the fine sediments are assumed to be suspended in the fluid. For this reason, the fluid density is assumed to be higher than water, approximately 1300 kg/m^3 (say). The coarse granular sediments form the solid phase. As the largest size of sediment in suspension is not well constrained in the literature, [154], we do not define the exact difference between suspended and non-suspended sediment size. It has been argued by Iverson [155], that particles larger than silt size are expected to contribute to the solid phase of debris flows. Others have demonstrated that the smallest particle size contributing to the solid phase in two-phase descriptions of flow is variable [154].

We therefore employ a two-layer approach to define the movement of the debris flow, [3, 4]. The first layer (subscript 1) contains the granular solid material and a part of the fluid. This layer is termed the mixture layer. The fluid is contained in the interstitial space between particles and is assumed to be bonded to the solid matrix. The second layer (subscript 2) is formed by the fluid, which can flow independently from the first layer. All the fluid which flows above the first layer is considered free, and subsequently, it can escape the matrix of solid particles, allowing debris flow de-watering and phase separation. Contrary to the approaches of [3, 4], we assume that the velocity of both fluid components (interstitial and free fluid) differ. This layer definition allows for the formulation of equations for the fluid phase (through the free fluid equations) without having to deal with the complex momentum transfer between the fluid and solid phases. Indeed, in the mixture layer, both solid and fluid are assumed to flow at the same speed. This model formulation allows us to describe highly complex momentum interactions via mass transfers associated with the

dilations in the solid matrix. As a consequence, the number of model parameters is reduced.

To describe the motion of the three different components (solid, interstitial fluid, free fluid) we need a system of three depth-averaged mass balance equations [104],

$$\frac{\partial h_1}{\partial t} + \vec{\nabla} \cdot (h_1 \vec{v}_1) = \left[\frac{\rho_f}{\rho_s}\right] Q_f + \left[\frac{\rho_e}{\rho_s}\right] E_1 \qquad \text{solid and inter-granular fluid} \qquad (5.1)$$

$$\frac{\partial h_{f,1}}{\partial t} + \vec{\nabla} \cdot (h_{f,1} \vec{v}_1) = Q_f + \left[\frac{\rho_e - \rho_f}{\rho_f - \rho_s}\right] E_1 \qquad \text{inter-granular fluid} \qquad (5.2)$$

$$\frac{\partial h_{f,2}}{\partial t} + \vec{\nabla} \cdot (h_{f,2} \vec{v}_2) = -Q_f \qquad \text{second layer, free fluid} \qquad (5.3)$$

where $h_{f,i}$ is the fluid content of the i-th layer and $\vec{v}_i$ its velocity; see Figs. 5.3 and 5.4. h_1 is a pseudo-variable used to simplify the conservation equations (see next), E_1 is the erosion rate, Q_f is the fluid mass exchange due to the dilatant action of the solid matrix, ρ_e is the density of the entrained material and $\vec{\nabla}$ is the divergence operator in cartesian coordinates.

As the mixture layer density is neither constant nor uniform, it is convenient to introduce the variable h_1, which is defined as the mixture layer mass, M_1, (per unit of area), normalized by the solid density ρ_s:

$$h_1 = \frac{M_1}{\rho_s} = \frac{\rho_s h_s + \rho_f h_{f,1}}{\rho_s} = h_s + \frac{\rho_f}{\rho_s} h_{f,1} \qquad (5.4)$$

where h_s represents the volume of the solid in the first layer (per unit area). With the introduction of this variable, we obtain a system of depth-averaged equations that can be defined by constant density and therefore be solved using existing shallow water solvers. For more details about the numerical scheme, see [132]. The *density* associated with the variable h_1 is ρ_s, which is constant and uniform. Importantly, the variable h_1 is without physical meaning and is introduced to mathematically simplify the mass and momentum balance equations. In this paper, the physical first layer height will be noted h_{sb} and is the sum of both first layer components; see Fig. 5.3 and 5.4:

$$h_{sb} = h_s + h_{f,1}. \qquad (5.5)$$

The equations relevant for the mixture layer, Eq. 5.2 and 5.1, contain the erosion rate, denoted by E_1. To compute the erosion rate, we adapted the single component model proposed by [40, 50] into the two-layer model. In the modified model, the erosion rate E_1 is no longer uniform nor constant as in [40, 50], but a function of the flow composition. If E_s represents the erosion rate for a completely solid flow and E_f for a completely fluid flood, the erosion rate E_1 is expressed under the assumption that erosion rates vary linearly between the two phases:

$$E_1(\phi_s) = \phi_s E_s + (1 - \phi_s) E_f \qquad (5.6)$$

where ϕ_s and ϕ_f are the first layer's volumetric solid and fluid fraction, respectively. They are defined as:

$$\phi_s = \frac{h_s}{h_s + h_{f,1}} = \frac{h_s}{h_{sb}}; \qquad \phi_f = 1 - \phi_s = \frac{h_{f,1}}{h_{sb}}. \qquad (5.7)$$

Erosion rates for debris flows have been calibrated with field events, and values for specific soil-types are available, see [40, 50]. However, the separation between E_s and E_f is difficult to describe (non-linear), and therefore complicated to calibrate, partially due to a lack of experimental data.

Therefore, we set as a first approximation, that E_s is some multiple of E_f. This reduces the number of free parameters in the model. Indeed, in this study, we prefer to describe the entrainment with a simple parametrization, with fewer model parameters and a simple physical interpretation rather than develop sophisticated but complex models, [42]. This approach facilitates the application to real events (and as we show in the results is sufficient to obtain realistic results). However, a better understanding of the erosion processes, more specifically the interdependency on the composition of the flowing debris, would help clarify the link between the solid and fluid erosion rates. The erosion rate is specified in the slope-perpendicular direction. Therefore, the model includes both downward erosion processes, but also lateral erosion from channel sides. Erosion begins when the shear stress is larger than some limit value. Because we adopt a Voellmy-type rheology, the basal shear stress is both a function of the normal stress and the velocity of the flow.

The free fluid can erode ground material only if the first layer height is zero (in fact, smaller than a typical granule size value, which we assume to be around 5 cm, see Table 5.6). In the alternative case, in which the free fluid flows above the mixture layer, the free fluid layer does not touch the ground (it is, by definition, flowing above the first layer). In this case, the eroded material is directly inserted into the mixture layer (because the second layer cannot possess solid material). This is the reason why E_1 is absent of Eq. 5.3. The erosion depth of the second layer is also computed using the model introduced by [40, 50], with an erosion rate corresponding to E_f. The shear stress used in the erosion depth computation, [40, 50], is the total shear stress, i.e., the sum of the shear stress of both layers. We also added a critical erosion velocity, $v_c = 0.5 \; m/s$ (see Table 5.6), which is the velocity threshold for erosion to begin.

The right-hand side of the mass conservation equations (Eq. 5.1- 5.3) contains the term Q_f [132], which is the fluid mass exchange rate between the inter-granular and free fluid. As stated above, the mass exchanges between the mixture layer and free fluid result from the dilatant actions of the solid particles in the debris flow, [108, 132, 134]. Under interactions with the rough bed of the channel, the solid matrix can dilate, [78, 80] and raise its center of mass from the co-volume configuration (whose height is noted h_0, right sketch on Fig. 5.4) to a dilated one (left sketch on Fig. 5.4). Under dilation, the void space between the particle increases [120], and free fluid fills this additional volume and is transformed into interstitial fluid. The inverse process occurs during the contraction of the solid matrix, for instance, when the flow reaches the run-out zone. The mass exchange rate is completely defined by the movement of the solid matrix center of mass (and the amount of fluid in the second layer). Therefore, the dilatancy governs the evolution of the first layer density, ρ_1, which can vary even if the solid mass (h_s) is conserved, throughout the inter-granular fluid concentration $\phi_f = (1 - \phi_s)$ (and then dilatancy), Eq. 5.7:

$$\rho_1 = \frac{M_1}{h_{sb}} = \frac{\rho_s h_s + \rho_f h_{f,1}}{h_{sb}} = \phi_s \rho_s + (1 - \phi_s)\rho_f. \tag{5.8}$$

Dilatant actions in the mixture layer are exploited to simulate de-watering and phase separations. Indeed, when the debris flow reaches the run-out zone, the flow decelerates, and the frictional shear work as well, which implies that the energy input coming from shearing is no longer sufficient to maintain the solid matrix in a dilated configuration. Consequently, the solid material contracts (the opposite of dilating), leading to an increase in friction and eventual deposition. During the collapse of the mixture layer, interstitial water is squeezed out and transformed into free fluid, which can

escape from the solid matrix. For more details about the mathematical structure of the dilatancy theory, see [132, 146].
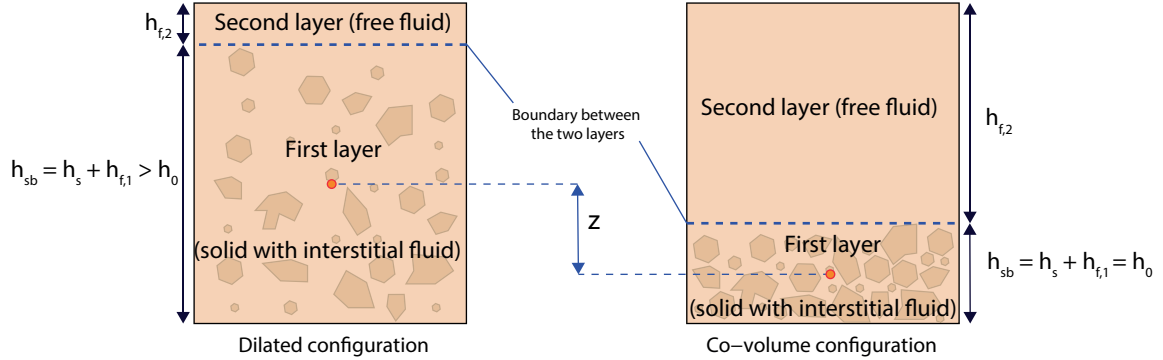

Figure 5.4: *Two different debris flow configurations consisting of equal amounts of solid and fluid masses. The left configuration is in a dilated configuration, occurring while flowing. The right configuration is the reference configuration, called the co-volume configuration, typically occurring when the flow is at rest. The different heights and other physical parameters are depicted in [132]. We define three variables associated with the solid mass, h_s, h_0, and h_{sb}. The height h_s is the volume of the solid particles in the flow, h_0 represents the reference height of the non-dilated mass, we call it the co-volume (It is different from h_s, because we consider that, even in the non-dilated configuration, the void space is not zero), whereas h_{sb} represents the dilated height of the solid mass, section 5.2.*

The variable h_1 is also used to simplify the two-dimensional, depth-averaged momentum balance equations: [104, 123, 124],

$$\partial_t(h_1 \vec{v}_1) + \vec{\nabla} \cdot \left(h_1 \vec{v}_1 \otimes \vec{v}_1 + \frac{g h_1^2}{2} I \right) + g h_1 \vec{\nabla} \left(b + \frac{\rho_f}{\rho_s} h_{f,2} \right) = -\frac{\vec{\tau}_1}{\rho_s} + \frac{\rho_f}{\rho_s} \vec{P}$$

$$\partial_t(h_{f,2} \vec{v}_2) + \vec{\nabla} \cdot \left(h_{f,2} \vec{v}_2 \otimes \vec{v}_2 + \frac{g h_{f,2}^2}{2} I \right) + g h_{f,2} \vec{\nabla} \left(b + h_{sb} \right) = -\frac{\vec{\tau}_2}{\rho_f} - \vec{P}$$

The vectors $\vec{v}_1$ and $\vec{v}_2$ represent the velocity of the first and second layers, respectively. The left-hand sides of Eq. 5.9 and 5.9 are the total variation of the momentum with respect to time, including the effect of gravity and the influence of each layer on the other [123, 124]. The right-hand side represents the change in momentum due to external forces (excluding gravity). The vector $\vec{P}$ is the rate of momentum exchange associated with the mass exchange Q_f, and $\vec{\tau}_i$ corresponds to the shearing stress acting on the i-th layer. To compute the shearing forces, we use the two parameters (μ and ξ) Voellmy-formulation, which is well-known in natural hazard mitigation practice in Switzerland and elsewhere [72, 73]. In this simple model formulation, the Coulomb friction determines the debris flow run-out, as it defines the critical slope angle θ_c at which the flow begins to decelerate, [105]:

$$\tan \theta_c = \mu. \tag{5.9}$$

The hydraulic friction ξ controls the flow speed of the movement. It allows for steady flow states to exist in ideal conditions, for example, infinitely long slopes with constant angle. Thus, we can

control the approximate run-out distance and steady flow velocity with only two parameters.

The debris flow rheology, $\vec{\tau}_i$, is not constant and uniform, but a function of the flow composition, [101]. The friction decreases when increasing the volumetric fluid fraction of the flow (or equivalently when decreasing the flow density). This empirical assumption is supported by well-constrained field measurements from Illgraben, [107,114,115,132]. In order to take the flow composition into account, let us define four frictional coefficients: ξ_s and μ_s, which describe the densest configuration of the mixture, i.e., the co-volume, and μ_f and ξ_f describe the free fluid. As the free fluid layer is always entirely fluid, its coefficients do not evolve and are always the same. That is, μ_f and ξ_f are constants.

For the mixture layer, we compute the Coulomb and turbulent coefficients by partitioning according to the solid and fluid volumetric parts:

$$\mu_1(\phi_s) = \frac{h_s \mu_s + h_{f,1} \mu_f}{h_s + h_{f,1}} = \phi_s \mu_s + (1 - \phi_s)\mu_f = \phi_s \mu_s \tag{5.10}$$

$$\xi_1(\phi_s) = \frac{h_s \xi_s + h_{f,1} \xi_f}{h_s + h_{f,1}} = \phi_s \xi_s + (1 - \phi_s)\xi_f. \tag{5.11}$$

We assume that the Coulomb friction will be negligible if the flow is entirely composed of fluid, which means that $\mu_f = 0$, eq. 5.10. This assumption is justified by the fact that the critical slope angle, Eq. 5.9, is zero for a liquid flow. Once the frictional parameters $\mu_1(\phi_s)$ and $\xi_1(\phi_s)$ are evaluated accordingly to the flow composition, we use the Voelly-Salm model to compute the frictional resistance of the flow, i.e.:

$$\vec{\tau}_1 = \mu_1(\phi_s)N_1\hat{e}_1 + \frac{\rho_1 g \|v_1\|^2}{\xi_1(\phi_s)}\hat{e}_1 \qquad \text{First layer} \tag{5.12}$$

$$\vec{\tau}_2 = \frac{\rho_f g \|v_2\|^2}{\xi_f}\hat{e}_2 \qquad \text{Second layer} \tag{5.13}$$

Where $\hat{e}_i = \frac{\vec{v}_i}{\|\vec{v}_i\|}$ is a unit vector pointing in the direction of the i-th layer. For more details concerning the two-phase rheological model, we refer the reader to [146].

The evolving flow rheology is a fundamental aspect of the model. Friction is described as a process, depending on erosion and the immediate terrain. Indeed, it can switch from a mud flow rheology, governed almost entirely by the turbulent term, to a rocky configuration, for which the Coulomb friction term is predominant. This fact will be of major importance when simulating complex GLOF events, because the flow composition, and therefore the flow rheology, does not change only from front to tail, as for standard debris flow, but can also endure important temporal transitions from muddy flow to a granular debris flow composition, when the flood has entrained enough solid material. Conversely, in the run-out zone, the core stops, and the fluid is washed-out, which corresponds to a transition from a debris flow to a muddy flow. Therefore, the rheology changes significantly during a single event, and a model which cannot take this evolution into account will likely not be able to give accurate numerical results with a simple set of frictional parameters. This will be demonstrated in the following case studies.

Event	Total Volume [m^3]	Peak discharge [m^3/s]
Lake 513	50'000	8333
Lake Palcacocha	1'800'000	4000
Aksay Valley	35'000	50

Table 5.1: Input hydrographs for the three case studies.

5.3 Case Studies

We apply a single set of rheological parameters to model all three separate case studies. The parameters are: $\mu_s = 0.16$, ξ_s=200 m/s^2 and $\xi_f = 600$ m/s^2. A forth parameter, the Coulomb friction of the fluid phase, is always set to zero, $\mu_f = 0$. These parameters are in close agreement to the values derived from debris flow measurements in Switzerland; see [146]. All of the other model parameters can be found in Table 5.6, Sec. 5.6. Except for one erosion parameter (the critical shear stress), all parameters are equal in the three different simulations. Once the initial conditions are fixed, the evolution of the flow friction (entirely defined by the value of μ and ξ in our model) will be computed according to the flow composition which itself is governed by the erosion and deposition processes.

To simulate these GLOF events, we define a flow hydrograph in which the total volume of the discharge is selected to match the field observations [47, 69, 148, 150, 156]. The initial material released during the breaching process is almost completely fluid (95% fluid, 5% solid). The input hydrograph parameters are provided in Table 5.1. The input values are based on [47, 56, 69]. The peak discharge of the Aksay event is lower than the two others because we assume a sub-glacial breaching process and not a wave that overtops the moraine dam. The definition of the initial conditions is of primary importance for hazard analysis because it controls the event magnitude and, therefore, the danger to humans and downstream infrastructure. In this study we focus on the reproduction of the cascading processes including flow transitions and phase separations, which do not depend directly on the initial conditions.

All the events have been simulated using a 10m x 10m DEM. The dataset used for the Aksay Valley DEM is: JAXA/METI ALOS PALSAR L1.0 2007, accessed through ASF DAAC 25 June 2022. For Lake 513, we resampled a 8m resolution DEM derived from Spring 2012 WorldView satellite imagery. For Lake Palcacocha we resampled a 5m photogrammetric DEM from 2013, provided by the Peruvian Ministry of the Environment (MINAM). To simulate the 1941 Lake Palcacocha event, we did not modify the 2013 DEM to account for terrain conditions in 1941, as for example in [56]. Although the channel clearly wandered between 1941 and 2013, we ran the simulations assuming the slope inclinations of the channel were approximately the same, and did not vary between 1941 and 2013.

5.3.1 Case Study 1: Lake 513, Cordillera Blanca, Peru

Lake 513 (4428 m a.s.l) is located in the Cordillera Blanca, Peru, Fig. 5.5. The Lake is surrounded by imposing glaciers and high mountains (peaks higher than 6000m a.s.l. are denoted by a triangle, see Fig. 5.5). Lake 513 is located in the upper part of the 20km long Chucchun catchment, which extends down to the city of Carhuaz (2640m a.s.l.), where the Chucchun River joins the main Santa River. The valley exhibits a complex topography, with many step-like changes in elevation, slope
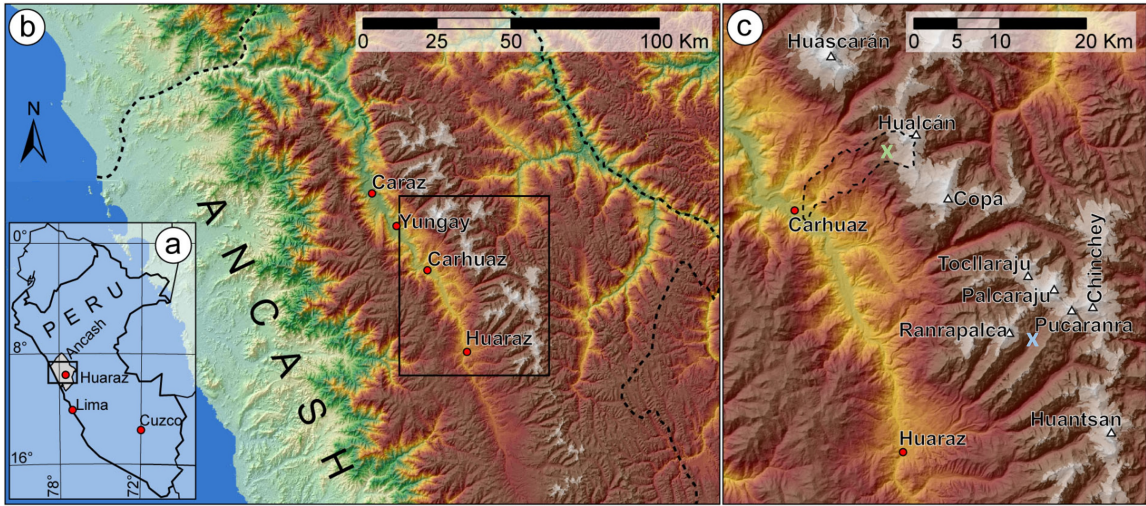
Figure 5.5: *a) Global map of Peru b) Location of the city of Carhuaz, Section 5.3.1, and the city of Huaraz. c) Lake 513 (green cross) and the Lake of Palcacocha (blue cross), Section 5.3.2 with their corresponding catchment (black dashed line). The original map can be found in [47].*

angle and channel width. On 11 April 2010, a 450,000 m^3 rock-ice avalanche detached from the bedrock beneath the steep hanging glaciers of Mount Hualcan. The avalanche impacted the glacial Lake and triggered a 24m high displacement wave that overtopped the rock dam of the Lake with a 19m freeboard by 5m. The event triggered a GLOF that caused severe damage to bridges, houses, roads and agricultural land as far down as the city of Carhuaz, see Fig. 5.5 and Table 5.2. The alternation between steep and flat terrain induces flow regime transitions and phase separations, due to the deposition of solid material on the flatter track segments, Fig. 5.6 and Table 5.2. The event of 2010 is of particular interest because different flow regimes have been characterized by field work performed immediately after the event, [47, 148]. The main features of the flow evolution are described in Table 5.2 and depicted in Fig. 5.6.

The flow types are computed by the model according to the definition supplied in Table 5.3, see Fig. 5.7. The blue color corresponds to a water/muddy flow, the yellow to a hyperconcentrated flow, and the red to a debris flow, see Table 5.3. Only zone five, i.e., corresponding to an hyperconcentrated flow, is not well reproduced by the model. In this region the solid material is deposited at the beginning of zone 5. Deposition in this area agrees with field observations; however, part of the solid material continued to flow until the flat valley above the city of Carhuaz. In our simulation, the part of the material flowing down the lower valley appears to be underestimated. Indeed, it is possible that fluvial bedload transport, which is not included in our model, may have transported some of this coarse sediment downstream.

Fig. 5.8 depicts the solid volumetric concentration integrated over time. The flow types, represented in Fig. 5.7, are based on these results. In zones four and five, the yellow ($\phi_s \approx 0.65$) sections correspond to the flowing material whereas the red zones ($\phi_s \approx 0.8$) located on the outer flow boundaries correspond to the deposition of solid material on the sides of the channel , which is consistent with [157]. The red part in the bottom valley (zone 5, in Fig. 5.8) also represents solid material deposition, as described in [47, 157].

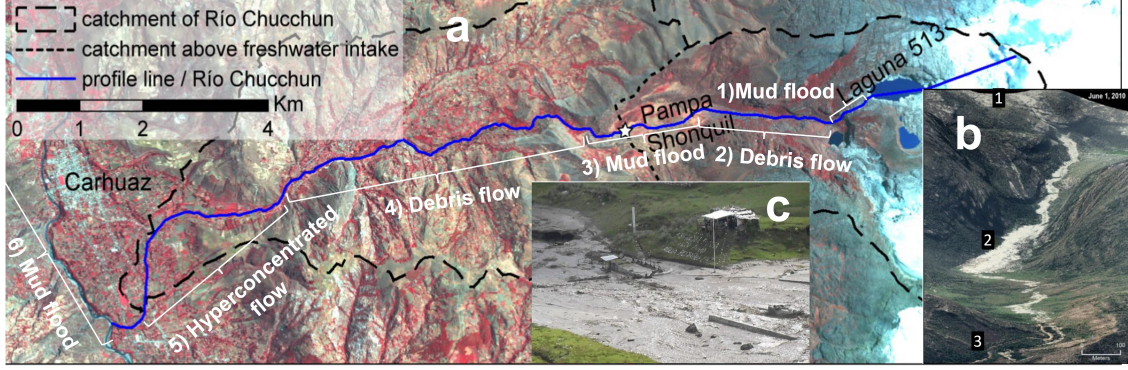In Fig. 5.9, the calculated values of μ are depicted. Values of μ are computed from the solid

Figure 5.6: *a) Map of the complete process chain of the 2010 GLOF at Lake 513. Six flow regime zones are defined following [47, 148]. The flow alternates between mud, hyperconcentrated and debris flows. A flow transition or phase separation occurs between each zone, leading to different flow regimes. The description of the flow in each zone, as well as the flow transitions are listed in Table 5.2. b) The inset depicts zones one, two, and three. We observe the deposition of solid material in zone two, [47]. c) Picture taken at the star location (Pampa Shonquil) during the 2010 event of Lake 513. The flow is almost entirely fluid, corresponding to a mud flow (Photo taken by Luis Meza, [148]).*

Zone	Flow type	erosion	Description
1	Mud flow	Yes	Initiation as a nearly pure water surge, the solid concentration increases due to entrainment along the steep slope downstream of the lake.
2	Debris flow	Yes	The flow continues to entrain material, reaching a debris flow type. As the slope flattens, the solid matrix deposits while the fluid is washed-out from the core, leading to phase separation.
3	Mud flow	Yes[1]	After the phase separation, the flow is almost entirely fluid. The slope is not steep enough in this zone to cause significant erosion.
4	Debris flow	Yes	As the slope increases, the erosion becomes more important and the flow evolves into a debris flow.
5	Hyperconcentrated flow	Yes	In some flatter and wider parts of the channel, lateral deposition of solid material occurred, leading to a lower solid concentration. The flow is closer to a hyperconcentrated flow.
6	Mud flow	No	The remaining part of the solid deposits in the flat valley close to Carhuaz, while the fluid continues to flow downstream.

Table 5.2: Description of the Lake 513 GLOF event. Due to the long and complex valley topography, the flow exhibits five flow transitions/phase separations. The footnote [1] indicates lateral erosion of the bed channel.

Color	Flow type	solid fraction ϕ_s	μ_1
Blue	Water/mud flow	$0 \leq \phi_s \leq 0.2$	$0 \leq \mu_1 \leq 0.04$
Green	Hyperconcentrated flow	$0.2 < \phi_s \leq 0.6$	$0.04 < \mu_1 \leq 0.11$
Red	Debris flow/solid material deposition	$0.6 < \phi_s \leq 0.8$	$0.11 < \mu_1 \leq 0.2$

Table 5.3: Color code used on Fig. 5.7, 5.13 and 5.18. Each color corresponds to a different flow type. The flow type is computed by integrating the volumetric solid concentration over time. This classification is only used for visualization.
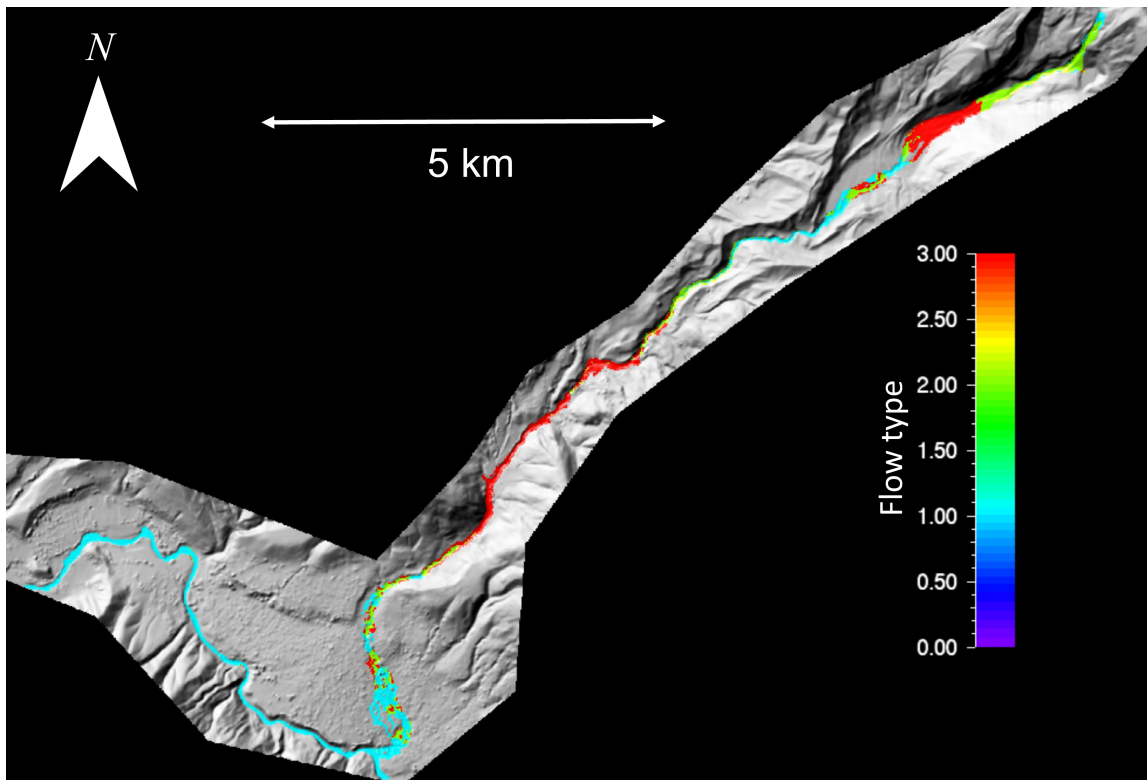
Figure 5.7: *Reconstruction of the flow type evolution for the event of Lake 513, in 2010. The colors represent different flow types, see Table 5.3. The computation is based on the volumetric solid fraction integrated over time, shown in Fig. 5.8. The flow transitions and phase separations, governed by entrainment and deposition processes, are captured by the model, see Table 5.2 and Fig. 5.6.*
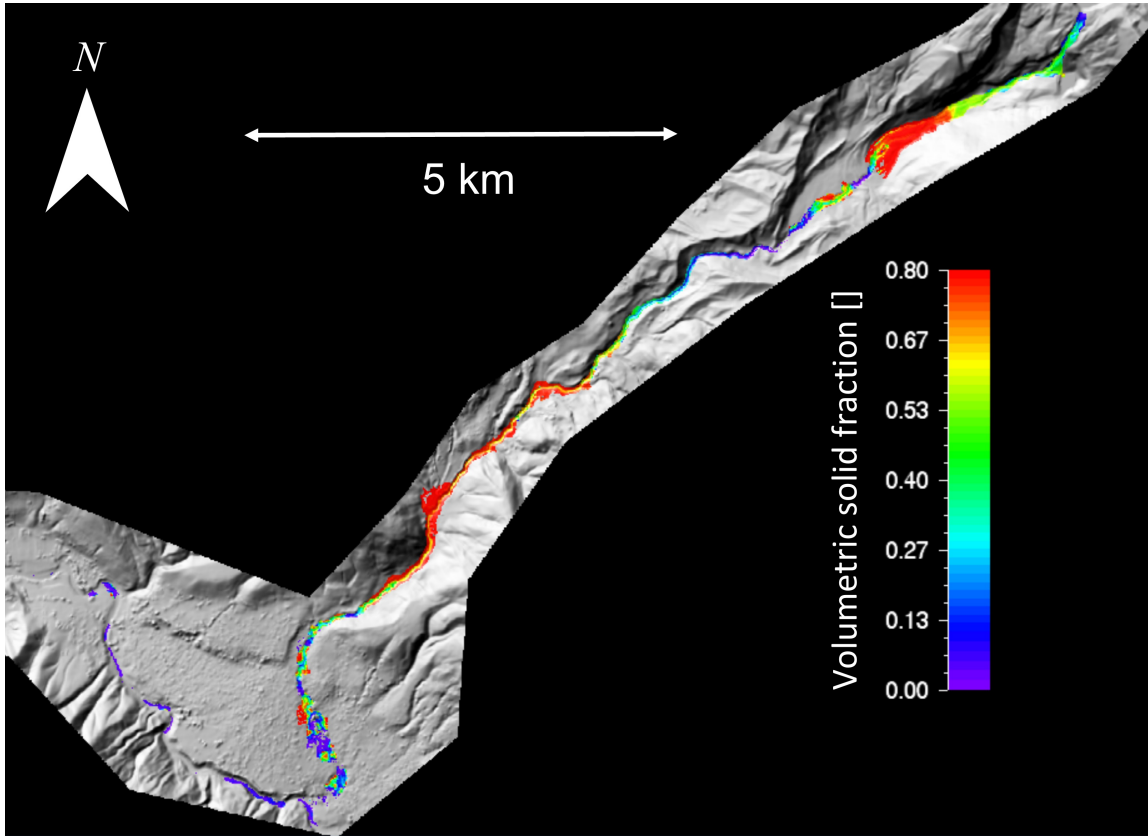
Figure 5.8: *Volumetric solid fraction integrated over time of the Lake 513 event of 2010. Flow type, see Tab. 5.2 and Fig. 5.7, is computed from the volumetric solid content.*

volumetric concentration (Fig. 5.8) using Eq. 5.10. The average value of the calculated μ coincides for each flow type with the values found in Fig 5.3. This result indicates that it is possible to model completely different flow regimes with a single set of parameters describing a process controlled change in flow rheology.

Fig. 5.10a shows the spatial evolution of the debris flow density in region four. The front of a standard debris flow is mainly composed of large blocks and is therefore associated with a high solid concentration. Towards the end of the flow in the upstream direction, the fluid concentration increases to reach an almost mud flow at the flow tail. Moreover, the largest density values are in the front and decrease towards the tail, as shown in Fig. 5.10a. The model appears to accurately compute the average solid-fluid concentration in time as well as over space.

Finally, Fig. 5.10b, depicts the simulated phase separation between zones two and three. The core of the flow (red) is in the process of decelerating and stopping, compared with Fig. 5.6c, while the fluid (blue) is washed-out and can continue to flow downstream, triggering a new debris flow farther down the valley.

The mass balance of this event, including specific erosion areas, was well characterized by [157]. The erosion depth obtained by our model is depicted in Fig. 5.11. According to [157], lateral erosion was observed in zone 3 but was not completely captured by the model. This may be due to the fact that in a depth-averaged model, which divides the flow into slope-perpendicular normal
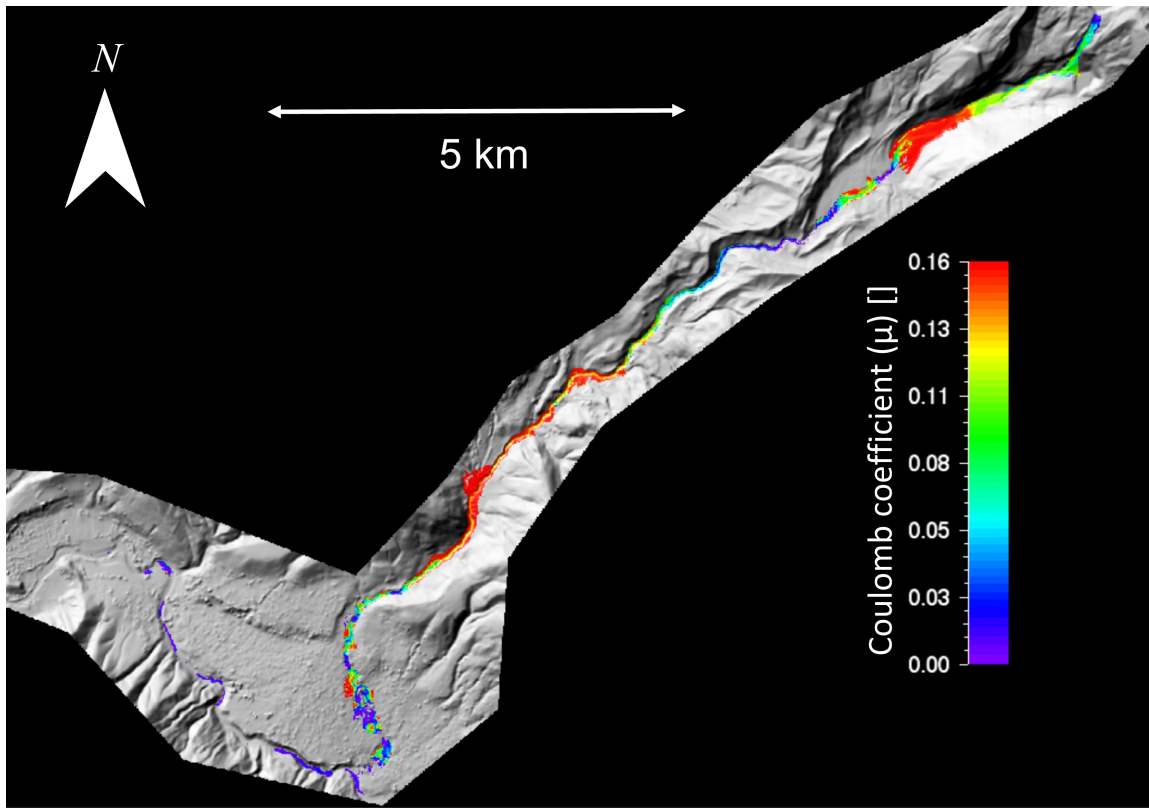
Figure 5.9: *Value of the Coulomb coefficient* μ, *based on the flow composition and Eq. 5.10. The evolution of rheology is of primary importance to simulate complex events with multiple flow regimes.*
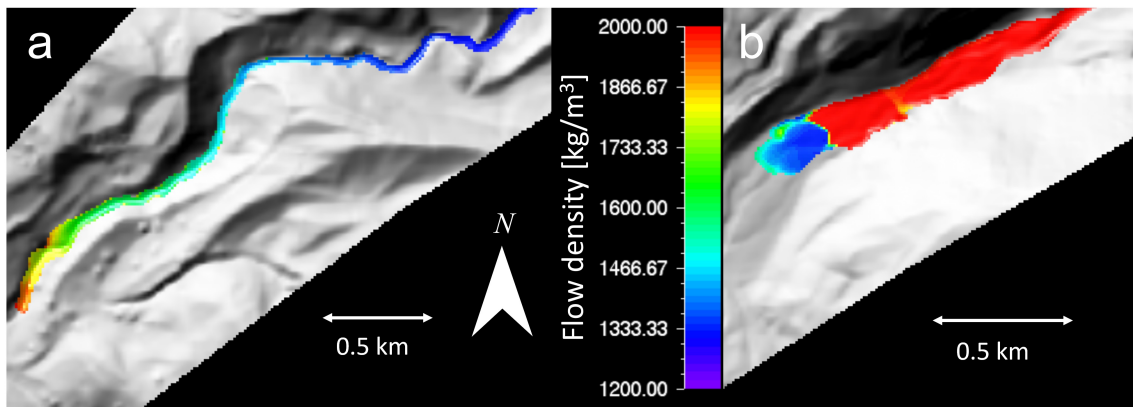
Figure 5.10: *a) Flow density (for t = 940s) in zone four. The density is high in the front and decreases toward the tail to reach the muddy fluid density, as expected for a standard debris flow. The model is able to compute the correct flow composition (or density) in time, as well as over the length of the torrent. b) Representation of the phase separation occurring between regions two and three. The core of the flow is stopped (red region), while the fluid is washed out (blue region)*

and slope-parallel shear stresses, might underestimate the total basal stress at steep, lateral edges. However, the strong erosion processes that occurred in regions 1,2, 4, and 5 coincide with the model results. The authors also noted deposition in zones 4 and 5, which also could be modeled, Fig. 5.8. In [157], the valley was divided into twelve different regions. For our study, we used only. The results of [157] have been averaged to fit our zone definition.

In this case study, the overall mass balance of the event, as well as the solid deposition behaviour are accurately reproduced indicating that the erosion behaviour integrated over the entire length of the torrent appears to be reasonable. However, there can be regions where the simulated erosion is over- or under-estimated. Finally, we underscore the fact that with a model that cannot reproduce the solid-fluid internal composition of such a flow, the rheology has to be tuned by hand in order to obtain correct results. Indeed, in the case of the back-computation of Lake 513 with the one-phase RAMMS model, [47], five different set of frictional coefficients have to be used to reproduce it accurately. This induces significant uncertainties about the numerical results, and cannot be done without past information on the back-computed event.

5.3.2 Case Study 2: Palcacocha Lake, Huaraz, Peru, 1941

Lake Palcacocha (4562m a.s.l.) is located in the Cordillera Blanca, above Huaraz (3050m a.s.l.), in Peru, Fig. 5.12. Similiar to the Lake 513 case study, the lake is surrounded by high mountains and large hanging glaciers. The Lake drains into the Cojup river, which arrives directly on the east side of Huaraz, after approximately 20 km, Fig. 5.12. In 1941 a breach formed in the moraine dam of Lake Palcacocha, possibly triggered by the impact of a mass movement (Mergili et al. 2020). The GLOF flowed downstream the Cojup valley. After completely entraining another Lake (Lake Jircacocha), which does not exist anymore [37, 158, 159], see Fig. 5.12, the resulting debris flow reached and destroyed a large part of the city of Huaraz killing approximately 1800 persons [37]. The damage to buildings and agricultural infrastructure, located either in the city of Huaraz, and also further downstream, was immense [160, 161].

Several numerical studies have already been performed of this event to back-calculate the 1941
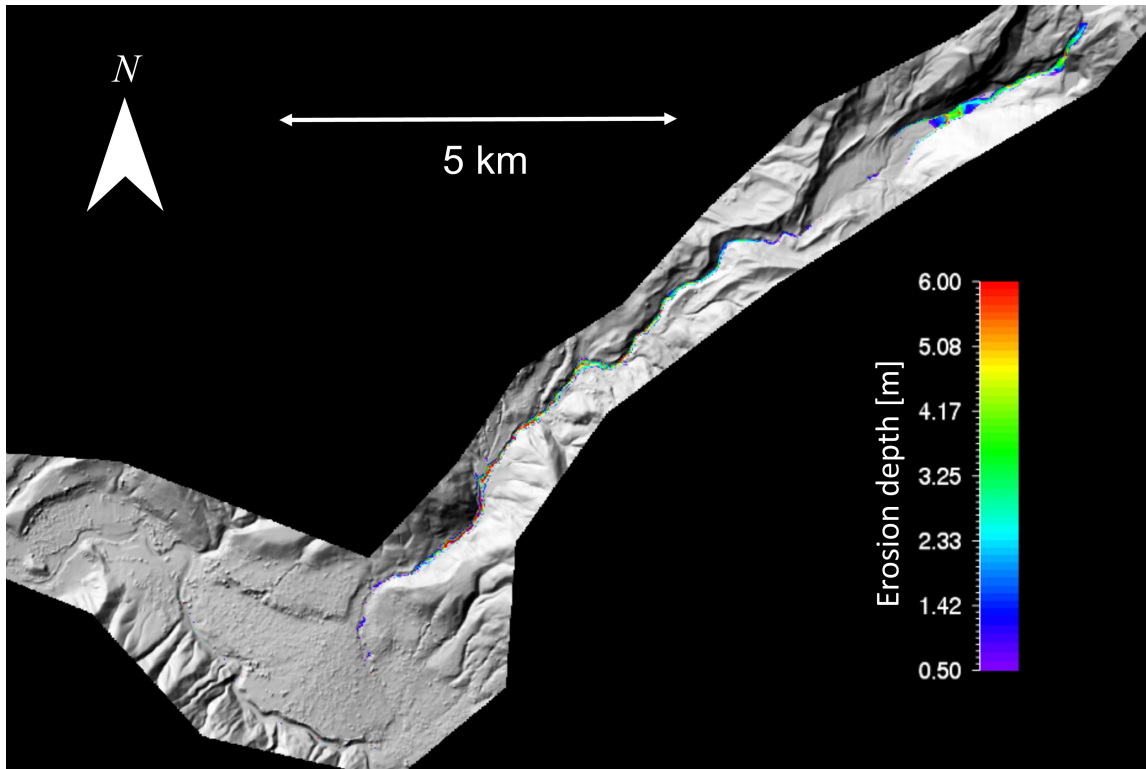
Figure 5.11: *Erosion depth of the Lake 513 event of 2010.*

outburst [56] and to predict future GLOF events [150, 162]. These studies indicate that the flow started as a water surge. The material entrained in the glacier moraine and on the steep slopes just below the initiation were deposited at the beginning of the long and flat Cojup valley. Up to an elevation of 4000 m a.s.l. (zone one in Fig. 5.13 and in Table 5.4) no surface erosion was observed, indicating a flow with a low solid concentration. Before the 1941 event, a Lake was present in the valley at an elevation of approximately 4130 m a.s.l. (see Fig. 5.12), which was completely entrained by the flow. At an elevation of around 4000 m a.s.l. (limit between zone a and two Fig. 5.13), the slope increases and significant erosion starts, leading to an increase in the solid concentration. The core stopped on flatter terrain before and inside Huaraz. Detailed studies by the Instituto Nacional de Defensa Civil have been performed to quantify the deposit area in the city, Fig. 5.14. After the stopping and deposition of the solid material, the flow, which was mainly composed of fluid with fine suspended sediments, continued to flow downstream the valley and cause great damage. This lower region was not simulated due to the unavailability of an accurate DEM, as well as due to the fact that the flow did not transition into another flow region. Therefore, we define only two flow regime zones for this case, which are separated by a red line in the plots.

Fig. 5.15 depicts the erosion depth obtained for the simulation of the 1941 event. Simulation results found in [156] indicate that erosion occurred mainly a few hundred meters downstream the Lake and in the lower part of the valley, see Table 5.4. This region is steeper than zone two, shown in Fig. 5.15. In between these two regions, no significant evidence of erosion was observed. The model captures this behavior, where the erosion is much stronger just below the release and in zone two. The red polygon in the Cojup valley corresponds to the entrainment of the Lake present before
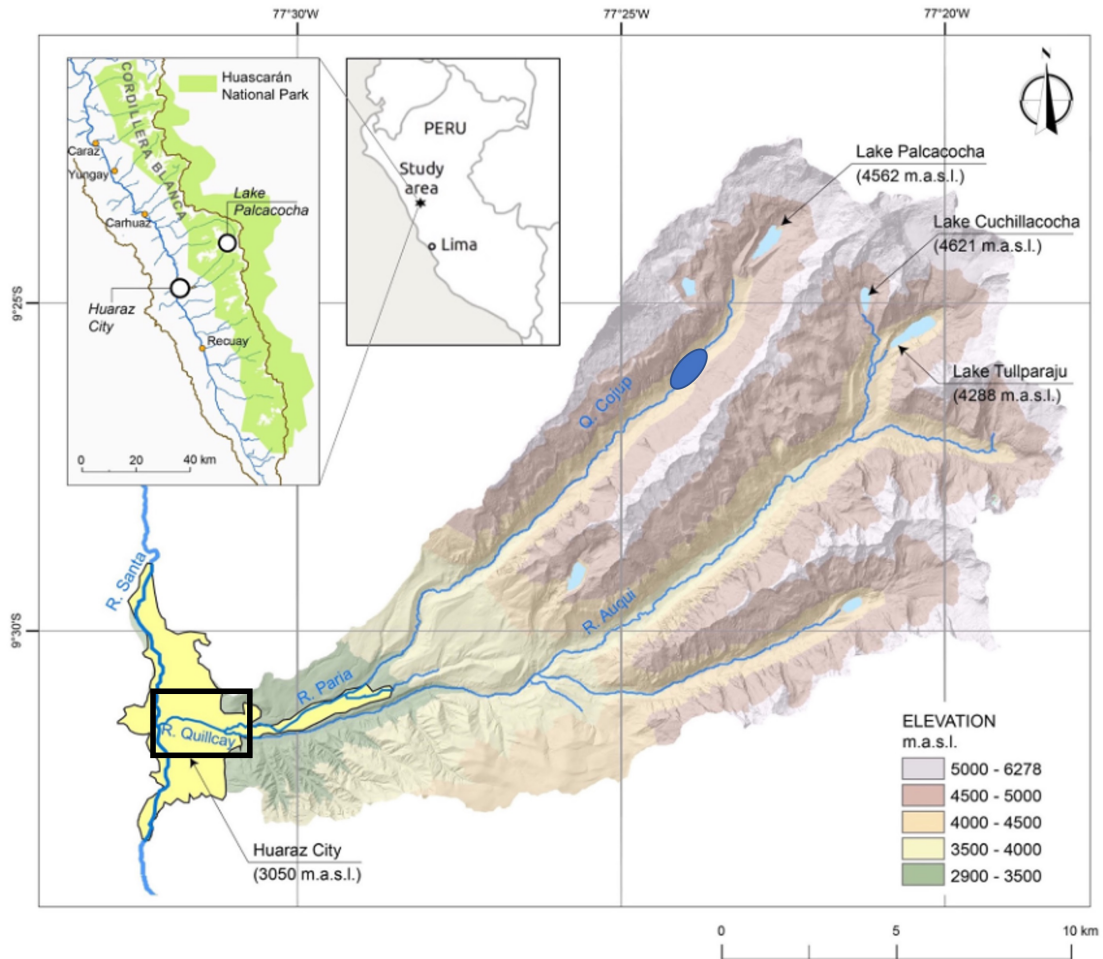
Figure 5.12: *Map of the Huaraz region with the Lake Palcacocha, which initiate the GLOF of 1941, including the location of Lake Jircacocha in the Cojup valley (blue ellipse). This Lake was completely entrained by the event of 1941. The black rectangle shows the extent of Fig. 5.14. Figure modified from [162], based on [150].*
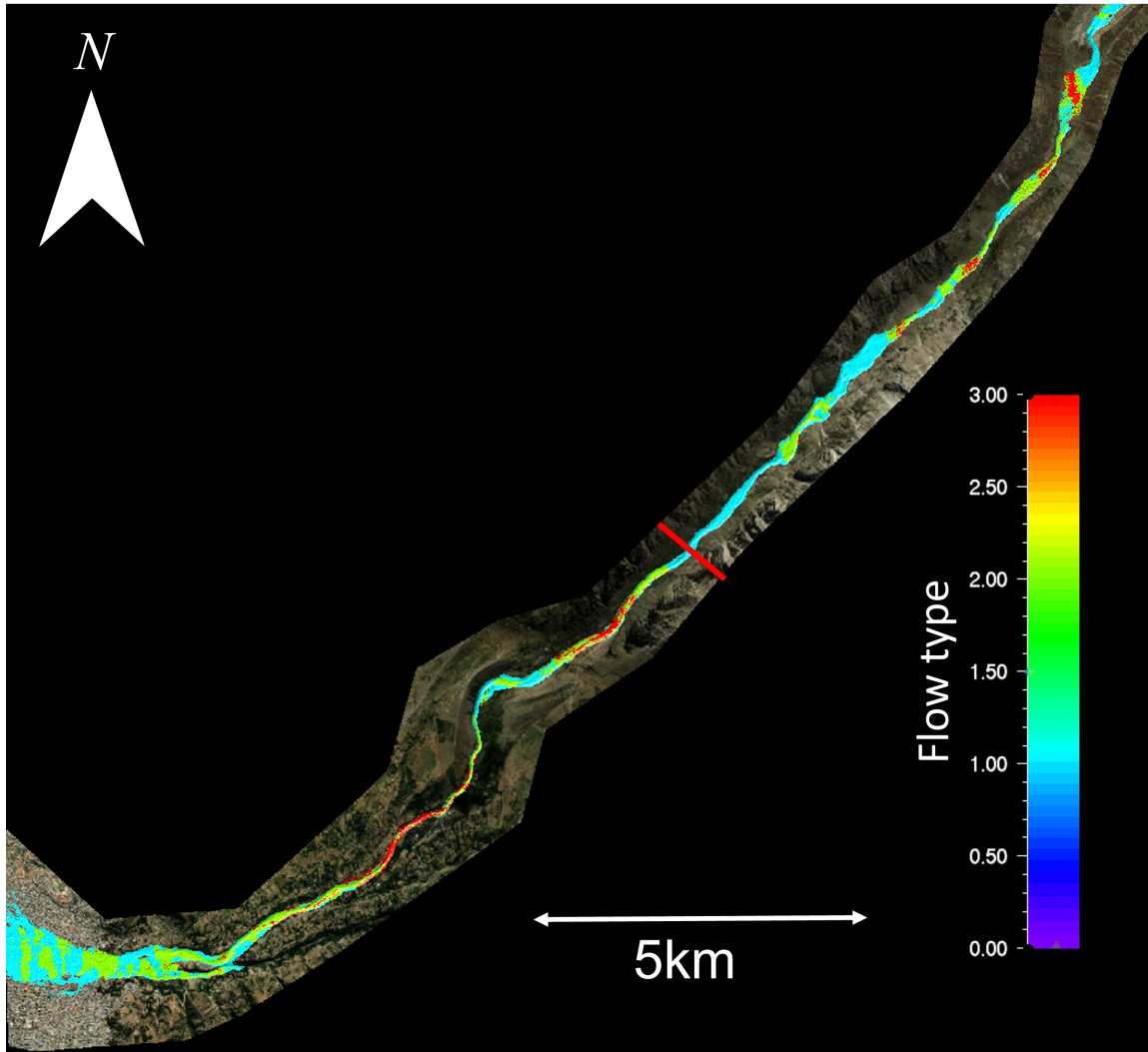
Figure 5.13: *Different flow types, see Table 5.3, that occurred during the Lake Palcacocha event. The simulated flow behavior corresponds to the observations, Table 5.4. The red line represents the separation between zones one and two. The flow has a high fluid concentration compared to the other two case studies, Fig. 5.7 and 5.18. The high fluid concentration is due to the entrainment of the glacier Lake while flowing in the Cojup valley.*
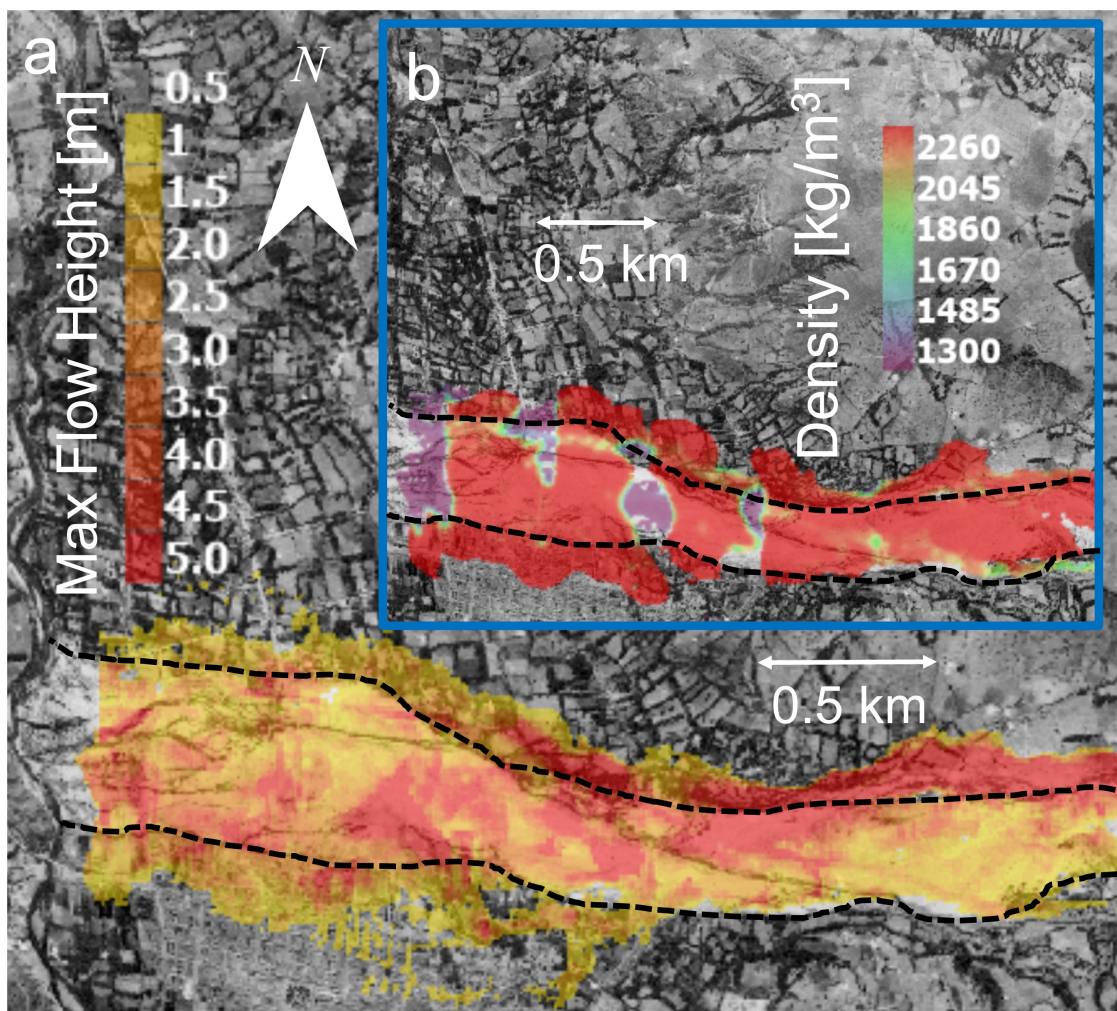
Figure 5.14: *a) Comparison between the observed debris flow fan of the 1941 event (background picture) and maximum flow height computed by the model. a. shows the observed deposit zone (black dashed line) as well as the flow height. The heights lower than 50 cm are not depicted. Inset b. shows the deposit density at the end of the event. The background picture is from A. Cicoira*

Zone	Flow type	Erosion	Description
1	Mud flow	no	Initiation as a nearly pure water surge, the small amount of solid material entrained in the moraine and below the lake stops a few hundred meters below the lake. At an elevation of $\approx$ of 4130 m a.s.l., the Lake Jircacocha was completely entrained by the flow.
2	Hyperconcentrated to Debris flow	yes	The flow starts to entrain a significant amount of solid material, increasing the solid concentration. As the flow becomes flat before and inside the city, the solid content deposits while the fluid is washed-out from the core, leading to a phase separation
3	Mud flow	no	After the phase separation, the flow is almost entirely fluid. The slope is not steep enough in this zone to cause significant erosion processes.

Table 5.4: Description of the Lake Palcacocha GLOF event, which occurred in 1941, destroying the center of the city of Huaraz and killing 1800 persons. A more detailed description of this event can be found in [56, 150].

the 1941 event. The surface and depth have been calibrated to fit the Lake volume, [56]. In this specific zone, the density of the entrained sediment is set to be the same as the fluid density, and stronger erosion is considered. The lake's entrainment does not only change the mass balance of the flow but its entire dynamics due to the fluidization of the flow. Indeed, the correct debris flow run-out distance, Fig. 5.14, would be impossible to model without the entrainment of the lake.

5.3.3   Case Study 3: Aksay Valley, Ala-Archa National Park, Kyrgyzstan

The Ala-Archa National park is located along the Kyrgyz Ridge, 40 km south of Bishkek, Kyrgyzstan (Fig. 5.16a). The debris flow fan of Aksay Valley is the largest in the Ala-Archa National Park, and several studies concerning debris flow monitoring, analysis, and simulation have been performed in this specific torrent [69, 151, 152]. The valley's elevation varies from 4895m a.s.l to 2200m a.s.l (run-out on the fan). Two glaciers can be found in the catchment's upper part: the Aksay glacier and the Uchitel Glacier (Fig. 5.16b). At the receding end of the Uchitel glacier stands a lake, which is the primary source of the GOLFs in this valley. The valley below the Lake can be decomposed into three distinct areas. The first one (denoted (1) on Fig. 5.16c) is a 2.3 km section characterized by a low average slope angle (less than 10°). It is followed by a 4.0 km long steeper section (denoted (2) on Fig. 5.16c) with a slope angle around 15° which ends in the bottom valley, i.e., the run-out area ((3) on Fig. 5.16c). This run-out section is almost flat (less than 5 °).

As we assume that the GLOF initiates with the outburst of the glacier lake, we expect a flood-type flow in the upper region (zone 1 Fig. 5.16c). Indeed, in this region, no significant erosion was observed. In zone 2, erosion processes started to become stronger; see Fig. 5.17b. As a consequence, we expect a flow with a higher solid concentration. Finally, the core of the debris flow stopped in the Aksay valley, see Fig. 5.17a and [151] (zone 3), and the fluid continued to flow downstream the valley (zone 4), almost without erosion processes. The flow history is summarized in table 5.5.

Fig. 5.18 shows the solid volumetric concentration integrated over time. One can see that the general behavior detailed above, i.e., flow transition from zone 1 to 2 and phase separation in zone 3, is captured by the model. Following [69, 151], we can estimate the run-out zone distance for the
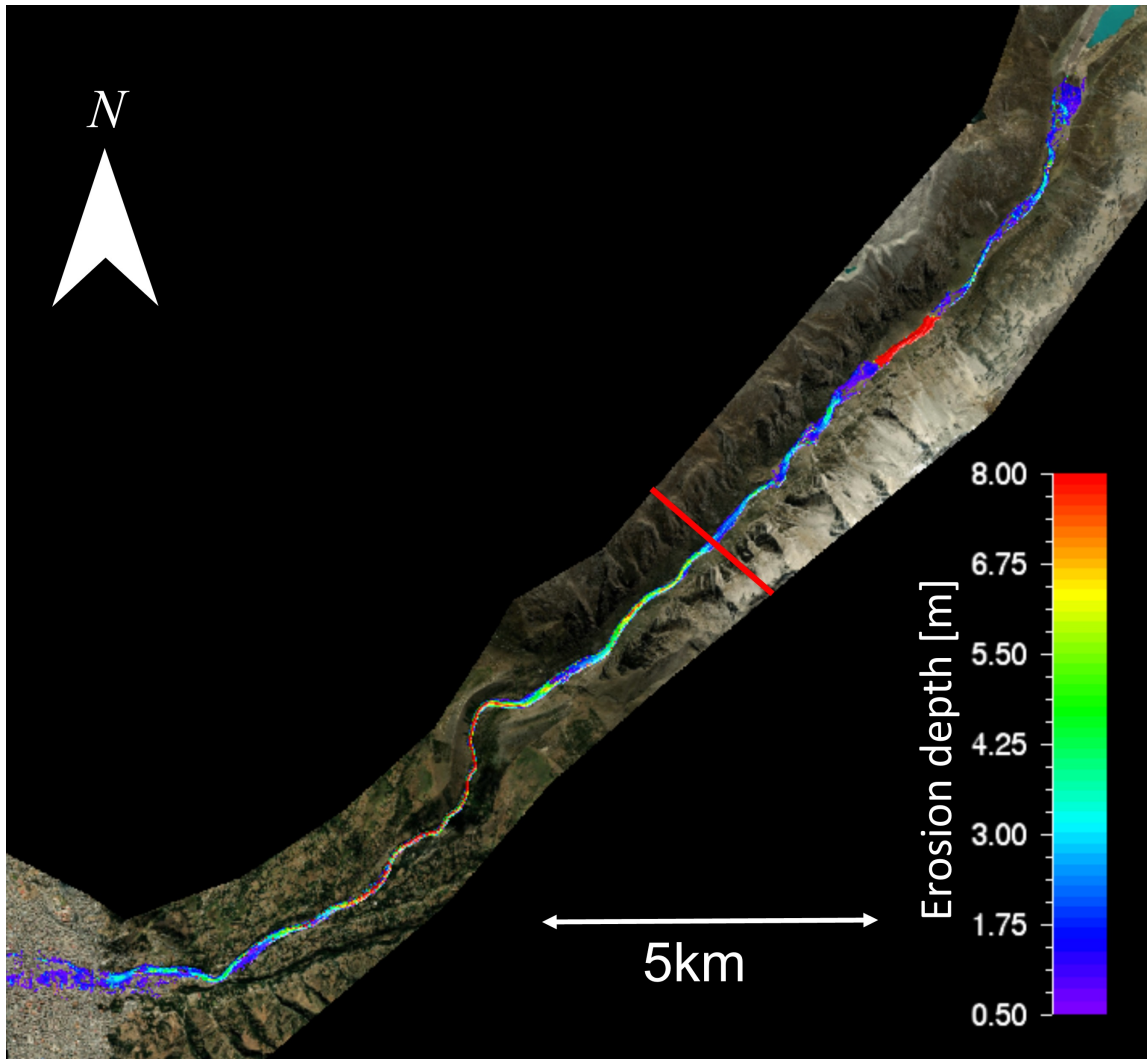
Figure 5.15: *Erosion depth obtained with the two-layer model. The red line represents the beginning of the area where significant erosion processes have been observed in the field, [156]. The red part before the red line (zone 1), represents the entrainment of the Lake Jircacocha, see Fig. 5.12.*

Zone	Flow type	erosion	Description
1	Mud flow to hyperconcentrated flow	no	Initiation as a nearly pure water surge, the solid concentration remains low because no significant erosion occurs
2	Debris flow	yes	The flow starts to entrain material, and the volumetric solid concentration increases.
3	Debris flow (deposition)	no data	As the flow reaches flatter terrain, a phase separation occurs
4	mud flow	no	After the phase separation, the flow is almost entirely fluid.

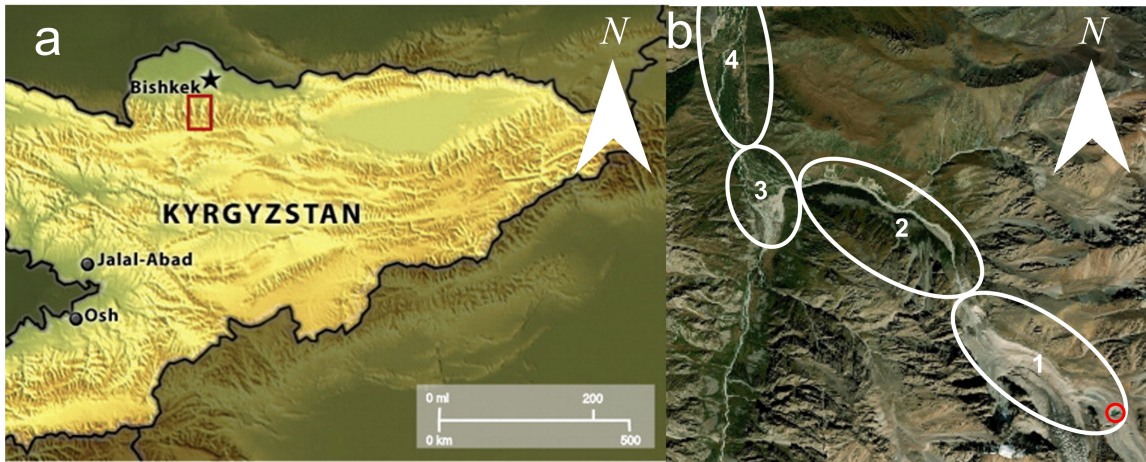Table 5.5: Description of the Aksay valley GLOF event.

Figure 5.16: *a) Location of the Ala-Archa Valley (National Park) in Northern Tien Shan. b) Orthophoto of the Aksay valley. The glacier Lake is indicated in red, while the valley itself has been decomposed into three different regions. The first one (1) with a low slope angle, the step channel (2), the run-out debris flow zone (3), and finally the gentle valley (4) which flows downwards the plain. Each zone exhibits different types of flow behavior and flowing transition occurs between them. However, no field observations concerning the flow types are available.*
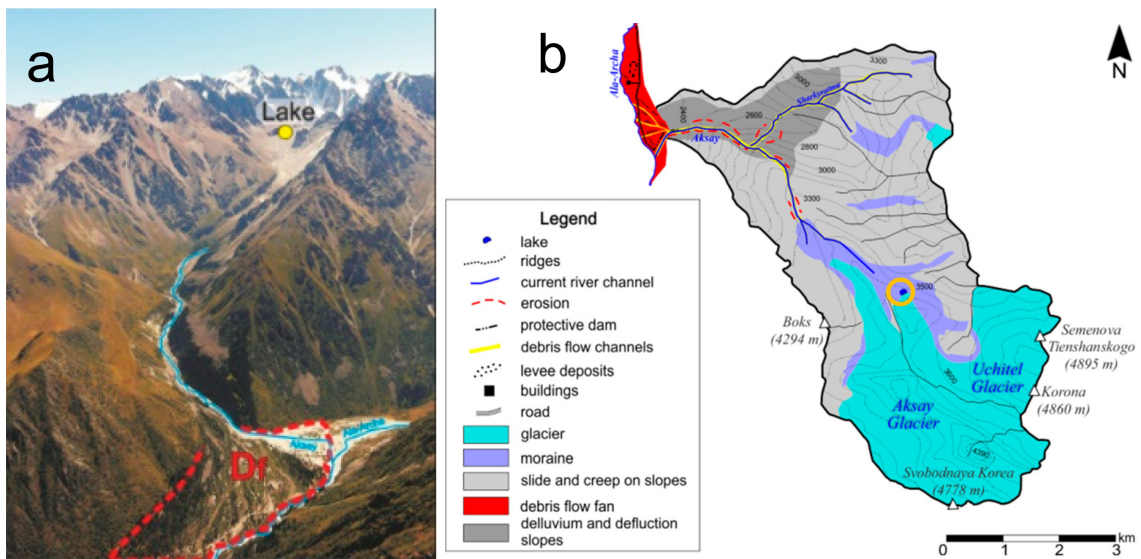
Figure 5.17: *a) debris flow fan zone. The red dotted line is the deposit zone delineated according to field observations [69]. b) Map of the Aksay Valley. The erosion area is denoted by the red dotted line while the initiating Lake is marked by an orange circle. Credit for the map: [69].*
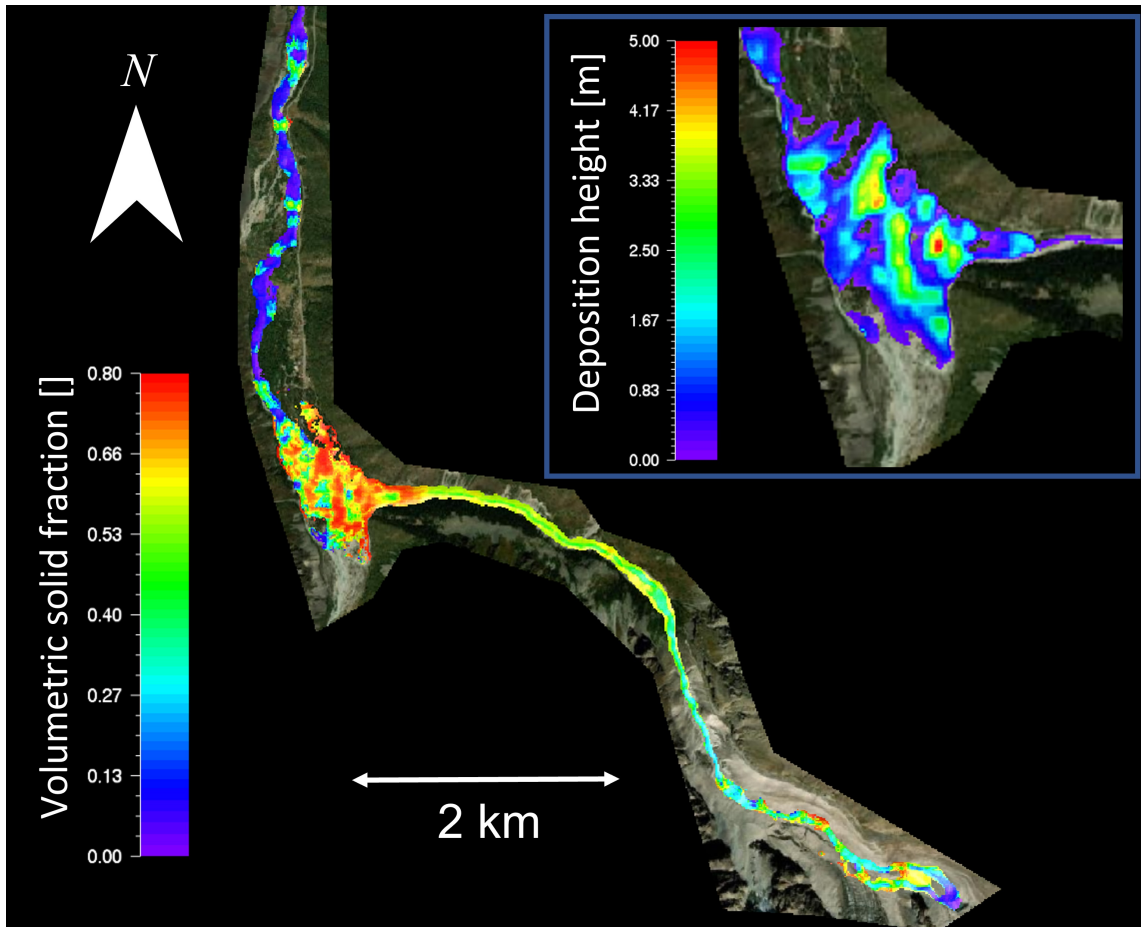
Figure 5.18: *Solid volumetric fraction of the flow, integrated over time. As expected, the flow is in a low solid concentration configuration in the first zone, where no erosion was observed. In the steeper part (zone 2), the volumetric solid concentration increases due to the erosion of solid material. Finally, the core deposits (zone 3) and the fluid is washed out and continue to flow downward (zone 4). The sub-figure on the upper right corner is the solid deposit of the flow, which is in good agreement with field observation reported in Fig. 5.17a.*

debris flow event of 1960 using satellite imagery, see Fig.5.17a. The average run-out area of the previous monitored event is approximately $A_{\text{run-out}} \approx 0.2$ km^2, [151]. In our simulation, we have the same order of magnitude for the value of the deposition area. The discharge could have been adjusted to fit the disposition area perfectly; however, without precise information about the peak discharge, we did not do so. Further, the run-out area detailed on Fig. 5.17a, is similar to the one we obtain in Fig. 5.18.

In [69], detailed observations of the erosion areas are provided; see Fig.5.17b. Fig. 5.19 depicts the numerically obtained spatial distribution of the erosion. The erosion depth is difficult to discuss due to a lack of information. However, the model accurately reproduces the erosion pattern (the region with or without erosion).

5.4   Discussion and Conclusions

GLOFs exhibit complex flow regime transitions due to the continually changing solid-fluid composition of the flow. Small inclination changes in the valley profile, or enlargement of the channel width, can produce solid-fluid phase separations, initiating the deposition of solid material. As GLOFs, by definition, initiate from a lake outburst, the initial flow is mainly fluid, leading to a mud flow. However, with the mobilization of loose sediments from the bed and channel sides, the floods acquire solid material, which leads to a transition from a mud flow to a hyperconcentrated flow. With the entrainment of more solid debris, the flows evolve to viscous, granular-type debris flows. These types of flow transitions could be captured by applying a Voellmy-type flow rheology [146] within the framework of a two-layer debris flow model [132]. The evolution of the internal solid-fluid composition governs the flowing properties, including the steady-state velocity in the channel or the run-out distance on flatter terrain. We apply a model to simulate the different flow regimes observed in the three case studies, Fig. 5.7, 5.13, and 5.18. The Lake 513 event is of great interest because it exhibits different flow regimes due to the long flowing distance (around 20km) over complex terrain topography. The field observations performed after the event [47, 148] permit a classification of the succession of flow types that enabled the validation of our model, which reproduces the events accurately from after the outburst to deposition. The erosion pattern and deposition area, described in [157], is also captured by the model. Although the model predicts with reasonable accuracy the erosion patterns, the run-out distances, the solid deposits and affected areas of the other two events (Fig. 5.14, Fig 5.15, Fig 5.18 and Fig. 5.19), the evaluation of model performance is more uncertain. The exact erosion depths are not known precisely, but the regions with and without erosion are well documented. These results indicate that both the erosion patterns and run-out distances can be captured by the model, which is an indirect validation of the model rheology.

The ability to model this complex flow behaviour has three main origins.

1. Firstly, a full *two-component approach* is used to predict the velocity of the solid debris with bonded fluid or the free (muddy) fluid. The physical and mathematical construction of the model is built on the foundation of a two-fluid, two-layer model involving well-constrained mass exchanges between the two fluid components. Unlike other models [1, 2, 3, 5], the fluid velocity is not computed using a Darcy-like approximation, which reduces two-component models to the solution of a single phase.
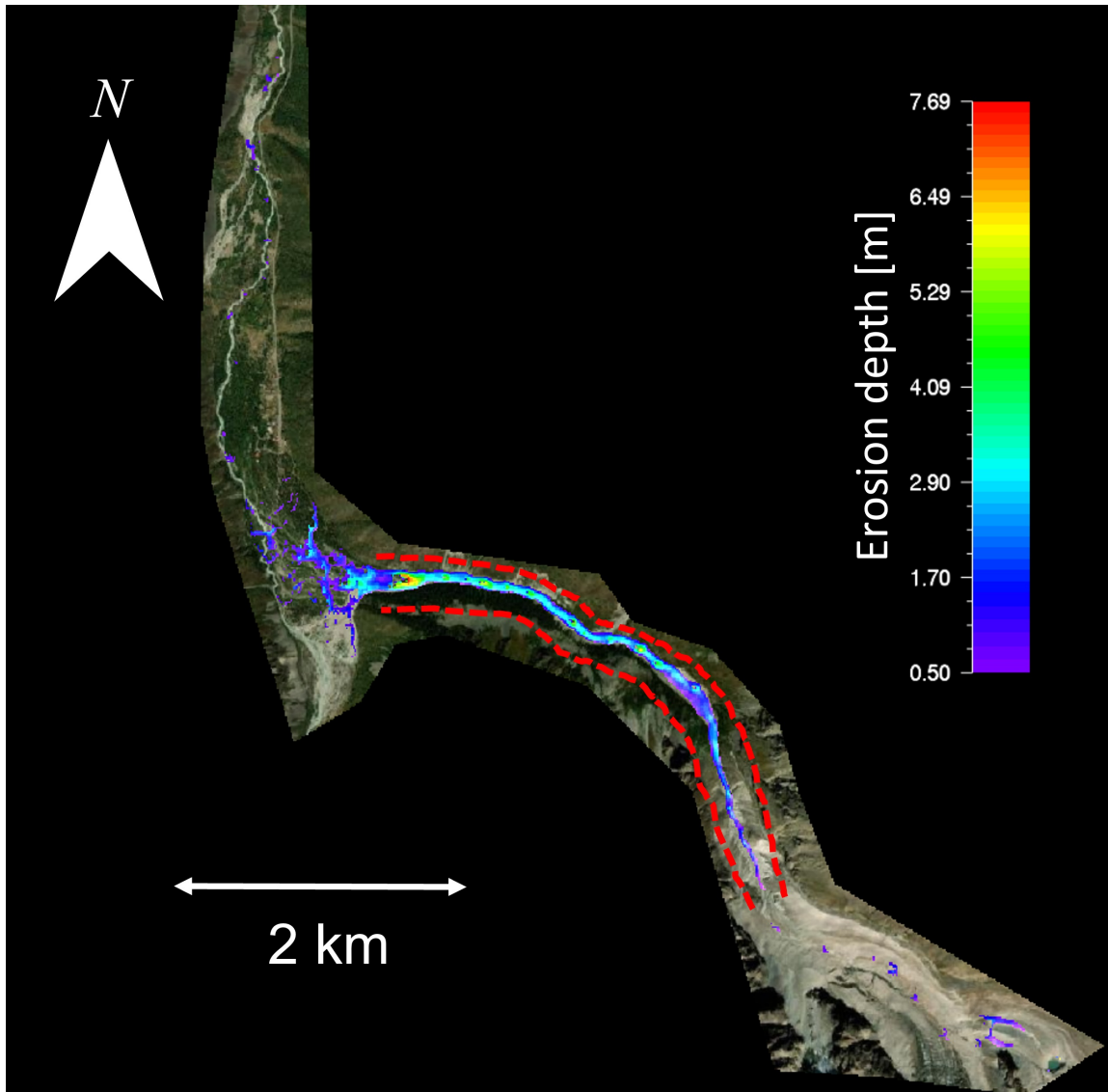
Figure 5.19: *Erosion depth obtained with the two-layer model. The red dotted line is the approximately observed erosion, shown in Fig. 5.17b, computed after field observations.*

2. Secondly, embedded into the governing equations is a *theory of granular dilantancy*. Mathematically, this requires the solution of an additional differential equation describing the production and decay of granular fluctuation energy, which drives the dispersive actions in the solid mixture. Although computationally more intensive, this approach enables us to predict the separation of the solid and fluid phases. The mass and momentum exchanges induced by the dilation of the solid matrix play a role in the interactions between the solid and the fluid components. It also controls the collapse of the solid matrix on flatter slope inclinations, allowing for phase separation and de-watering.

3. Finally, the central aspect of the model is the *evolving rheology*. A uniform and constant rheology fails to reproduce the dynamics of complex events such as GLOFs, [33], even if they can be applied with significant tuning to model specific debris flow events. For example, five different zones associated with different rheology coefficients (μ and ξ) had to be defined to reproduce the event of the Lake 513, [47] when using the one-phase, constant rheology RAMMS model. The use of Eq. 5.10 allows the two-layer model to reproduce a fluid-like behavior, driven by the turbulent friction, but also a granular-like flow, driven by the Coulomb friction, within a single mathematical framework. In this model, we assume a simple relation between the flow composition, given by ϕ_s and ϕ_f, and the rheology, represented by $\mu(\phi_s)$ and $\xi(\phi_s)$. More accurate data would be needed to develop a more sophisticated mathematical model. Preliminary laboratory studies show that in the range of $0.3 < \phi_s < 0.9$, the shearing intensity and the volumetric fluid concentration can be approximated by a linear relation.

The dependency of the rheological parameters on the flow composition also allows us to reduce the interval of possible values for the frictional parameters, μ_s, ξ_s, and ξ_f. Indeed, the same set value was used for the three scenarios, which exhibit different behaviors and a wide variation of flow volumes, i.e., 35'000 m^3 for the event of Aksay valley and 1'800'000 m^3 for the Lake Palcacocha event (without entrainment). The uniformity of the rheological free parameters is one of the attractive features of the model and will be of primary importance when applying it to hazard analysis prediction. Indeed, a model which is not able to reproduce the flow transitions and phase separations would have to be tuned to perform relevant simulations. This implies a major limitation for *a priori*-type applications, when there is no historical information available. Confidence in the free parameters is a central question in numerical models. A debris flow model should be able to perform accurate simulations of real events using the lowest number of free parameters possible. Back-calculation of existing events with models that contain few parameters is a first step to developing powerful, predictive tools for practical applications. We applied the same frictional parameters, within the framework of a theory based on modeling flow dilations within the solid matrix. Modeling flow behavior in this way, produced a model with only one free parameter. This is the ratio between α, representing the production of solid dilations and β, representing its decay. We fixed the production α,hence β is the free parameter governing flow regime transitions. Interestingly we were able to use the same value of β for all three events. More case studies are clearly required to determine if this approach is valid in general.

The uniformity of the rheological parameters was also helpful to better model erosion processes.

In the three case studies, the critical shear coefficient had to be adapted to correctly simulate the Palcacocha 1941 event. Even if the release material, as well as the terrain topography, are generally known with reasonable accuracy, the bed properties of the entire torrent are largely unknown. Therefore, the adaptation of the erosion parameters is rather linked to a need for more accurate knowledge about precise boundary conditions rather than a specific model deficiency. It is to be expected that the erosion parameters must be selected for a specific site. The selection of parameters remains a modeling problem that is, in the end, a more general problem well-known to the debris flow engineering community.

5.5   Acknowledgments

5.6 Annex

Name	Symbol	value	Unity []
Solid density	ρ_s	2500	kg/m^3
Fluid density	ρ_f	1300	kg/m^3
Co-volume density *1	ρ_{co}	2000	kg/m^3
Solid Coulomb coefficient	μ_s	0.16	-
Fluid Coulomb coefficient	μ_f	0.0	-
Solid turbulent coefficient	ξ_s	200	m/s^2
Fluid turbulent coefficient	ξ_f	600	m/s^2
Configurational energy production	α	0.2	-
Configurational energy decay	β	0.07	$1/s$
Mean collapse time	$\Gamma = \frac{\alpha}{\beta}$	2.86	s
Entrained density	ρ_e	2000	kg/m^3
Solid erosion rate	E_s	0.03	m/s
Fluid erosion rate	E_f	0.003	m/s
Critical shear stress	τ_c *2	0.5	kPa
Critical shear stress coefficient	$\frac{d\tau}{dz}$ *2	-0.2/-0.4*3	m/kPa
Critical erosion velocity	v_c	0.5	m/s
Gridsize	Δx	10.0	m
Granule size	Gr	7	cm

*1 defined without fluid in the interstitial space in between the solid particles. *2 For the definitions of these values, refer to [40, 50].

*3 the first value corresponds to the Lake 513 and Aksay events and the second one to the Lake Palcacocha event.

Chapter 6

Conclusion and Outlook

6.1 Conclusion

The aim of this thesis was to develop a two-fluid debris flow model to simulate gravitationally driven saturated granular flows. In a first step, we divided the debris flow into a mixture layer and a fluid layer and modified the shallow water equations to include the dilatant action of the solid matrix. The rheology and entrainment processes were implemented in the second step, using real-scale debris flow measurements and laboratory experiments as a guide. Finally, three well documented real-case scenarios were back-computed to validate the model.

Particle dilatancy plays an essential role in granular media due to its influence on the volumetric solid fraction. In debris flow science, various models [1, 4] have already been developed to include this phenomenon but their computation is based on restrictive assumptions. Our approach, that also includes dilatancy, is different. It is based on the balance between the production and decay of granular velocity fluctuations in the solid matrix. The production is constrained by thermodynamic arguments, most notably that it is some fraction of the irreversible shear work. These arguments are easier to manipulate within the framework of depth-averaged models. From a mathematical point of view, the use of dilatancy induces a natural coupling between the mass and momentum balance equations. It is possible to quantify the mass and momentum fluid interactions between the two layers. The dilatant action of the solid matrix controls the fluid content which subsequently governs the evolution of the debris flow composition. With this approach it is possible to accurately simulate real-case events. The comparison with measurements of Illgraben (a real-scale debris flow test site in Wallis, Switzerland), revealed that our model was able to reproduce the evolution of the spatial streamwise solid-fluid distribution. A last key point concerning dilatancy in granular flows is that when it is implemented within two-fluid layer models, it facilitates the simulation of different flow regimes. Indeed, in steep terrain, the capture and bonding of the free fluid by the mixture layer due to the dilatant action of the solid matrix leads to a solid-fluid quasi-uniform flowing behavior. When the slope flattens, the shearing energy is no longer sufficient to maintain the system in a dilated configuration. The solid collapses and eventually stops while the fluid is washed-out of the core of the debris flow and continues to flow downstream, leading to two completely different solid-fluid flow regimes.

There are two main difficulties to formulate a flow rheology in a two-phase modeling approach. Firstly, the computation of the momentum transfer between the two phases is difficult to quantify. In our real-scale debris flow experiments it cannot be separated from the total measured shear. Models for inter-phase shearing are necessary in all models which mathematically divide the balance equations into the solid and fluid parts. Consequently, their formulation requires introducing abstract free parameters, which are difficult to calibrate for practitioners. Furthermore, in the case when the flow components are moving with different velocities, large momentum exchanges are induced in the differential equations, which can lead to numerical instabilities and reduce the computational efficiency of the model (smaller time steps). Introducing a mixture layer, where both materials flow at the same velocity, bypasses this problem. In addition, the definition of a second layer, consisting entirely of muddy fluid, allows us to simulate phase separations (with the help of the dilatancy theory). Therefore, the proposed formulation is a proper two-phase model. It does not include a Darcy-like approximation [1, 2, 3, 5] and, in addition, simplifies the fluid momentum balance equations. A further advantage of this method is that it avoids the problem of directly computing the solid-fluid shearing interactions. The second problem associated with flow rheology is how to quantify flow resistance in terms of the solid-fluid flow composition. Real-scale measurements performed at Illgraben indicate that the shear stress intensity decreases with increasing the fluid content. Based on these considerations, we assumed a linear relationship between the decrease of the shear stress and the increase in volumetric fluid content. Although this ansatz is purely empirical, it allowed us to model different debris flow behavior, varying from a muddy flood to viscous granular flow. Moreover, with a single two-phase flow rheology it was possible to model different flow regimes. Similarly, we adapted an existing erosion model, based on the erosion measurements carried out in Illgraben, for our two-fluid model. To test the model, we compared it to field measurements obtained with two drone flights, one flight executed before and the other flight after an event (occurring in August 2021), in the Ritigraben (Switzerland) torrent. Subtracting both measured DEMs provided the eroded volume along the channel. We found a good agreement between the measured and numerical results. In GLOFs, field observations revealed zones with significant erosion adjacent to zones with little or no erosion. The comparison of our model with documented GLOF events, which are significantly larger in volume than the Ritigraben event, showed its capability to reproduce observed erosion patterns (zones with and without erosion).

The overall purpose of a debris flow model is to make predictions, especially in the context of a changing environment. Currently, debris flow models (to our knowledge) are not predictive and are mainly used to reproduce events with ad-hoc tuning of flow parameters. In fact, it is also often the case that the free parameters are manipulated by hand within the same simulation to be able to reproduce the different flow regimes observed in real events. This approach is no longer acceptable in practice. In future, the prediction of changing run-out and deposition volumes from debris flow hazards will require considering existing, but also ever more extreme, meterological boundary conditions. Scenario based simulations must implement these sediment and hydrological conditions without altering the free parameters governing the rheological behavior of the flow. Only then, can well founded predictions of debris flow hazard be made under consideration of changing, perhaps extreme, climatic conditions. A first step in this process is to reproduce experimental data

with the ultimate validation being the successful back computation of different real events using the same rheological parameters.

The new two-fluid, two-phase debris flow model we present in this thesis is designed to meet this challenge. There is no need for ad-hoc parameter manipulations and, subsequently, the model can be used as a predictive tool. As a validation, we simulated three GLOF events. We focused on events that are well documented and exhibit a complex flow behavior. The GLOFs included entrainment (leading to flowing transitions) and deposition of solid material (inducing phase separations). Therefore, these events reveal several different flow types, depending on the average solid-fluid volumetric concentration, which makes them challenging to model accurately. Our model successfully reproduced these three events, while keeping the same reduced set of initial free parameters. The model captured the flowing transitions and phase separations due to the erosion and deposition of solid material. The erosion patterns, run-out distances and inundated areas were correctly reproduced. The benefit of using a process-based rheology becomes apparent for events that travel long distances. As the flow composition changes continuously, implying a change in friction, a model with an unchanging flow rheology cannot model these hazardous flows without manual manipulation of the flow parameters for specific track sections. These simulations highlight the crucial role of the interplay between the dilatancy, the erosion/deposition processes and the evolving, ever-changing flow rheology. These processes are deeply entangled and indispensable to accurately model the complex dynamics of GLOFs.

6.2 Outlook

This dissertation presents a two-fluid, two-layer debris model aimed at application in engineering hazard analysis. Further work must be performed to improve the modeling results in order to improve the reliability of model predictions.

One important assumption concerns the relationship between the shear stress of the solid phase and the fluid content. We approximated this relation using a linear function. Laboratory experiments indicate that this approximation is valid for a large range extending from $\phi_s = 0.3$ to $\phi_s = 0.75$. Of great interest is how to define this relationship for the range $\phi_s < 0.3$; that is, for low friction values when the debris flow has the greatest mobility. For this important range a deeper understanding of the interplay between the solid and fluid, which engenders the complex flowing rheology, is needed. It includes theoretical development, numerical modeling and, more importantly, accurate laboratory experiments. Typically, kinematic values (velocities and flow heights) are measured in laboratory experiments. In this dissertation we utilized direct measurements of shear forces – both at the real (Illgraben) and laboratory scale. We measured shear forces using a flat and relatively smooth (without roughness) shear plate. This is not representative of a real debris flow channel. The preliminary analysis of debris flow measurements indicates that the measured shear stress on a smooth plate is too low to be realistic. In the absence of roughness, the flow slides over the plate with low friction. Therefore, we measured only one part of the total shear stress. These results are helpful, in the sense they quantify an extreme case and could be used in the modeling, but are nonetheless inconclusive. In future experiments, exchangeable force plates should be constructed which allow measurements with and without surface roughness. However,

adding realistic artificial roughness is complicated, as the roughness must scale with the size of the solid particles in the flow. To this aim, the force plates at Illgraben should be modified (enough control data exists for the smooth plates) to model channel roughness. In a laboratory setup, new 3-D printing methods could be employed to generate artificial roughness.

At present our numerical model is based on the relation $\phi_s + \phi_f = 1$. This assumption indicates that our debris flow cannot be undersaturated. Moreover, all the interstitial space between the particles *must* be filled by fluid. No air can exist between the particles. This assumption is reasonable for a muddy flood or at the tail of a debris flow when the flow is saturated by fluid. It is not the case at the bouldery, granular front. Often debris flow deposition begins at the lateral sides of the flow, which are also undersaturated. The problem to simulate undersaturated flow configurations is to introduce a third phase, the interstitial air ϕ_a. Clearly, we must consider the case $\phi_s + \phi_f + \phi_a = 1$, with $\phi_a > 0$. As mentioned above, a linear relation between the shearing intensity and the volumetric fluid content of the flow can be a reasonable hypothesis for a specific range of fluid concentration but is certainly no longer valid for undersaturated configurations. The current model likely underestimated the friction at the debris flow front and sides, leading to an undervaluation of the dam-like behavior of the front, as well as the channel side deposition of solid material. These two effects impact both the dynamics and mass balance of the flow. To solve this problem we must consider an additional mass balance equation (the momentum of the air can be supposed neglectable). The addition would only slightly increase the overall complexity of the model.

Once the critical shear stress exceeded, the erosion model used in this thesis assumes a constant erosion rate. Although it can reproduce real debris flow data, including the location of erosion in GLOF simulations, the assumption of a constant erosion rate is clearly questionable. A better understanding of the entrainment process would allow the computation of the erosion rate as a function of the physical properties of the flow, i.e, basal shear stress, momentum, kinetic energy, etc. Laboratory experiments accompanied with DEM simulations would be a great help to explore this problem in more detail. Another problem associated with erosion modeling is that the flow quantities at the running surface of the debris flow are relevant. These, of course, can differ significantly from the depth-averaged values. The new approach must be calibrated and validated by field observations and/or laboratory experiments and ideally would be implemented without the introduction of additional free parameters.

In this model, we assume that the rheology is always described by a turbulent term, proportional to the velocity squared. Even if this is realistic for a fast muddy flow, this approach will overestimate friction for a slow granular debris flow. Indeed, a laminar friction term, proportional to the velocity, could be more appropriate in this case. The difference between both regimes can be distinguished using the dimensionless Reynolds number. However, an abrupt change from 1 to 2 in the velocity exponent would probably induce numerical instabilities, or at least reduce the computational speed. Therefore, the velocity exponent must be computed as a smooth function of the Reynolds number (or any other number on which the analysis is based) rather than taking a non-continuous value.

The debris flow model we developed and tested in this thesis attempts to model different flow regimes within the same mathematical and numerical framework. There have been many recent events in which debris flow initiation is caused by mixed rock/ice instabilities (Chamoli, India, 2021), or when a large rock mass falls onto glacier ice (Cengalo, Switzerland, 2017). Considerable meltwater is generated by frictional heating (in addition to the entrainment of fluid-rich sediments). The existing model should be extended to include the ice-component, as well as the thermal heat production, leading to the production of meltwater. Thus, the model should include additional internal energy equations to track the temperature of the rock/ice/water mixture. Such a model would find large application in the back-calculation of cascading events in the high-mountain regions of the world.

Bibliography

[1] Richard M Iverson and David L George. A depth-averaged debris-flow model that includes the effects of evolving dilatancy. i. physical basis. *Proceedings of the Royal Society A: Mathematical, Physical and Engineering Sciences*, 470(2170):20130819, 2014.

[2] David L George and Richard M Iverson. A depth-averaged debris-flow model that includes the effects of evolving dilatancy. ii. numerical predictions and experimental tests. *Proceedings of the Royal Society A: Mathematical, Physical and Engineering Sciences*, 470(2170):20130820, 2014.

[3] E Bruce Pitman and Long Le. A two-fluid model for avalanche and debris flows. *Philosophical Transactions of the Royal Society A: Mathematical, Physical and Engineering Sciences*, 363(1832):1573–1601, 2005.

[4] François Bouchut, Enrique Domingo Fernandez-Nieto, El Hadji Kone, Anne Mangeney, and Gladys Narbona-Reina. A two-phase solid-fluid model for dense granular flows including dilatancy effects: comparison with submarine granular collapse experiments. In *EPJ Web of Conferences*, volume 140, page 09039. EDP Sciences, 2017.

[5] François Bouchut, Enrique D Fernandez-Nieto, Anne Mangeney, and Gladys Narbona-Reina. A two-phase two-layer model for fluidized granular flows with dilatancy effects. *Journal of Fluid Mechanics*, 801:166–221, 2016.

[6] Shiva P Pudasaini. A general two-phase debris flow model. *Journal of Geophysical Research: Earth Surface*, 117(F3), 2012.

[7] Richard M Iverson. The debris-flow rheology myth. *Debris-flow hazards mitigation: mechanics, prediction, and assessment*, 1:303–314, 2003.

[8] Markus Stoffel and Christian Huggel. Effects of climate change on mass movements in mountain environments. *Progress in physical geography*, 36(3):421–439, 2012.

[9] Markus Stoffel, Davide Tiranti, and Christian Huggel. Climate change impacts on mass movements—case studies from the european alps. *Science of the Total Environment*, 493:1255–1266, 2014.

[10] Luzia Fischer, Christian Huggel, Andreas Kääb, and Wilfried Haeberli. Slope failures and erosion rates on a glacierized high-mountain face under climatic changes. *Earth surface processes and landforms*, 38(8):836–846, 2013.

[11] Christian Huggel, John J Clague, and Oliver Korup. Is climate change responsible for changing landslide activity in high mountains? *Earth Surface Processes and Landforms*, 37(1):77–91, 2012.

[12] Wilfried Haeberli and Martin Beniston. Climate change and its impacts on glaciers and permafrost in the alps. *Ambio*, pages 258–265, 1998.

[13] Christian Huggel, Oliver Korup, and Stephan Gruber. Landslide hazards and climate change in high mountains. 2021.

[14] M. Beniston, D. Farinotti, M. Stoffel, L. M. Andreassen, E. Coppola, N. Eckert, A. Fantini, F. Giacona, C. Hauck, M. Huss, H. Huwald, M. Lehning, J.-I. Lopez-Moreno, J. Magnusson, C. Marty, E. Moran-Tejeda, S. Morin, M. Naaim, A. Provenzale, A. Rabatel, D. Six, J. Stötter, U. Strasser, S. Terzago, and C. Vincent. The european mountain cryosphere: a review of its current state, trends, and future challenges. *The Cryosphere*, 12(2):759–794, 2018.

[15] Fabian Walter, Florian Amann, Andrew Kos, Robert Kenner, Marcia Phillips, Antoine de Preux, Matthias Huss, Christian Tognacca, John Clinton, Tobias Diehl, et al. Direct observations of a three million cubic meter rock-slope collapse with almost immediate initiation of ensuing debris flows. *Geomorphology*, 351:106933, 2020.

[16] Patrick Baer, Christian Huggel, Brian W McArdell, and Florian Frank. Changing debris flow activity after sudden sediment input: a case study from the swiss alps. *Geology Today*, 33(6):216–223, 2017.

[17] C Wilhelm, GC Feuerstein, A Huwiler, R Kühne, et al. Rock fall cengalo and debris flows bondo: insights from the cantonal authorities. In *Forum für Wissen*, number 2019, pages 53–66. Eidgenössische Forschungsanstalt für Wald, Schnee und Landschaft, 2019.

[18] Marc-Henri Derron, Valerie Baumann, Tiggi Choanji, François Noël, Ludovic Baron, Simon Hiscox Baux, Aurelien Ballu, Emmanuel Nduwayezu, and Michel Jaboyedoff. Assessment of the 2019 chamoson debris flow event (swiss alps). In *EGU General Assembly Conference Abstracts*, page 15074, 2020.

[19] Lise Boulicault, Andrea Moscariello, Dario Ventra, and Julien Moreau. Reconstructing the evolution of the chamoson alluvial fan (swiss rhône valley) from outcrop observations and geo-radar survey. In *EGU General Assembly Conference Abstracts*, page 732, 2014.

[20] https://www.rts.ch/info/suisse/11486087-une-famille-de-six-personnes-secourue-suite-a-une-lave-torrentielle-a-jaun.html.

[21] https://www.bafu.admin.ch/landscape-award-bregaglia.

[22] https://www.rts.ch/info/suisse/11486087-une-famille-de-six-personnes-secourue-suite-a-une-lave-torrentielle-a-jaun.html.

[23] Adam Emmer, Simon K Allen, Mark Carey, Holger Frey, Christian Huggel, Oliver Korup, Martin Mergili, Ashim Sattar, Georg Veh, Thomas Y Chen, et al. Progress and challenges in glacial lake outburst flood research (2017–2021): a research community perspective. *Natural Hazards and Earth System Sciences*, 22(9):3041–3061, 2022.

[24] Adam Emmer. Glacier retreat and glacial lake outburst floods (glofs). In *Oxford Research Encyclopedia of Natural Hazard Science*. 2017.

[25] Dunning S. Taylor C., Robinson T.R. Glacial lake outburst floods threaten millions globally. *Nature Communications*, 14(487), 2023.

[26] Akhmetkal R Medeu, Nikolay V Popov, Viktor P Blagovechshenskiy, Maulken A Askarova, Alikhan A Medeu, Sandguash U Ranova, Aidana Kamalbekova, and Tobias Bolch. Moraine-dammed glacial lakes and threat of glacial debris flows in south-east kazakhstan. *Earth-Science Reviews*, 229:103999, 2022.

[27] Louis Lliboutry. Glaciological problems set by the control of dangerous lakes in cordillera blanca, peru. ii. movement of a covered glacier embedded within a rock glacier. *Journal of Glaciology*, 18(79):255–274, 1977.

[28] Guoxiong Zheng, Simon Keith Allen, Anming Bao, Juan Antonio Ballesteros-Cánovas, Matthias Huss, Guoqing Zhang, Junli Li, Ye Yuan, Liangliang Jiang, Tao Yu, et al. Increasing risk of glacial lake outburst floods from future third pole deglaciation. *Nature Climate Change*, 11(5):411–417, 2021.

[29] Shaun D Richardson and John M Reynolds. An overview of glacial hazards in the himalayas. *Quaternary International*, 65:31–47, 2000.

[30] SS Marchenko, AP Gorbunov, and VE Romanovsky. Permafrost warming in the tien shan mountains, central asia. *Global and Planetary Change*, 56(3-4):311–327, 2007.

[31] Daniel Farinotti, Laurent Longuevergne, Geir Moholdt, Doris Duethmann, Thomas Mölg, Tobias Bolch, Sergiy Vorogushyn, and Andreas Güntner. Substantial glacier mass loss in the tien shan over the past 50 years. *Nature Geoscience*, 8(9):716–722, 2015.

[32] Dmitry Petrakov, Alyona Shpuntova, Alexandr Aleinikov, Andreas Kääb, Stanislav Kutuzov, Ivan Lavrentiev, Markus Stoffel, Olga Tutubalina, and Ryskul Usubaliev. Accelerated glacier shrinkage in the ak-shyirak massif, inner tien shan, during 2003–2013. *Science of the Total Environment*, 562:364–378, 2016.

[33] Matthew John Westoby, Neil Franklin Glasser, James Brasington, Michael John Hambrey, Duncan Joseph Quincey, and John M Reynolds. Modelling outburst floods from moraine-dammed glacial lakes. *Earth-Science Reviews*, 134:137–159, 2014.

[34] Raphael Worni, Christian Huggel, John J Clague, Yvonne Schaub, and Markus Stoffel. Coupling glacial lake impact, dam breach, and flood processes: A modeling perspective. *Geomorphology*, 224:161–176, 2014.

[35] https://www.rts.ch/info/suisse/13765459-les-lacs-glaciaires-menaceraient-plus-de-700000-personnes-en-suisse.html.

[36] https://ruhrresidence.kunstvereineruhr.de/en/2017/11/14/life-and-death-at-lake-palcacocha-environmental-uncertainty-in-the-peruvian-andes-part-i/.

[37] Steven A Wegner et al. Lo que el agua se llevo consecuencias y lecciones del aluvion de huaraz de 1941. nota tecnica n° 7., 2014.

[38] Ying-Hsin Wu, Ko-Fei Liu, and Yi-Chin Chen. Comparison between flo-2d and debris-2d on the application of assessment of granular debris flow hazards with case study. *Journal of Mountain Science*, 10(2):293–304, 2013.

[39] Yu-Charn Hsu and Ko-Fei Liu. Combining trigrs and debris-2d models for the simulation of a rainfall infiltration induced shallow landslide and subsequent debris flow. *Water*, 11(5):890, 2019.

[40] Florian Frank, Brian W McArdell, Nicole Oggier, Patrick Baer, Marc Christen, and Andreas Vieli. Debris-flow modeling at meretschibach and bondasca catchments, switzerland: sensitivity testing of field-data-based entrainment model. *Natural hazards and earth system sciences*, 17(5):801–815, 2017.

[41] Jose Garres-Diaz, François Bouchut, Enrique Domingo Fernandez-Nieto, Anne Mangeney, and Gladys Narbona-Reina. Multilayer models for shallow two-phase debris flows with dilatancy effects. *Journal of Computational Physics*, 419:109699, 2020.

[42] Alessandro Cicoira, Lars Blatny, Xingyue Li, Bertil Trottet, and Johan Gaume. Towards a predictive multi-phase model for alpine mass movements and process cascades. *Engineering Geology*, 310:106866, 2022.

[43] Marc Christen, Julia Kowalski, and Perry Bartelt. Ramms: Numerical simulation of dense snow avalanches in three-dimensional terrain. *Cold Regions Science and Technology*, 63(1-2):1–14, 2010.

[44] G Lu, A Caviezel, M Christen, Y Bühler, and P Bartelt. Modelling rockfall dynamics using (convex) non-smooth mechanics. pages 575–583, 2018.

[45] Johan Gaume, Alec van Herwijnen, Ted Gast, Joseph Teran, and Chenfanfu Jiang. Investigating the release and flow of snow avalanches at the slope-scale using a unified model based on the material point method. *Cold Regions Science and Technology*, 168:102847, 2019.

[46] Johan Gaume, T Gast, J Teran, A Van Herwijnen, and C Jiang. Dynamic anticrack propagation in snow. *Nature communications*, 9(1):3047, 2018.

[47] Mark Carey, Christian Huggel, Jeffrey Bury, Cesar Portocarrero, and Wilfried Haeberli. An integrated socio-environmental framework for glacier hazard management and climate change adaptation: lessons from lake 513, cordillera blanca, peru. *Climatic Change*, 112(3):733–767, 2012.

[48] Abani K Patra, Andrew C Bauer, CC Nichita, E Bruce Pitman, Michael F Sheridan, M Bursik, Byron Rupp, A Webber, AJ Stinton, LM Namikawa, et al. Parallel adaptive numerical simulation of dry avalanches over natural terrain. *Journal of Volcanology and Geothermal Research*, 139(1-2):1–21, 2005.

[49] V d'Agostino and PR Tecca. Some considerations on the application of the flo-2d model for debris flow hazard assessment. *WIT Transactions on Ecology and the Environment*, 90, 2006.

[50] Florian Frank, Brian W McArdell, Christian Huggel, and Andreas Vieli. The importance of entrainment and bulking on debris flow runout modeling: examples from the swiss alps. *Natural Hazards and Earth System Sciences*, 15(11):2569–2583, 2015.

[51] Ramms (2017). ramms::debrisflow user manual. davos, switzerland: Eth.

[52] http://wikimapia.org/377499/Medeu-Mudflow-Control-Dam.

[53] Shiva P Pudasaini and Jan-Thomas Fischer. A mechanical erosion model for two-phase mass flows. *arXiv preprint arXiv:1610.01806*, 2016.

[54] Katherine R Barnhart, Ryan P Jones, David L George, Brian W McArdell, Francis K Rengers, Dennis M Staley, and Jason W Kean. Multi-model comparison of computed debris flow runout for the 9 january 2018 montecito, california post-wildfire event. *Journal of Geophysical Research: Earth Surface*, 126(12):e2021JF006245, 2021.

[55] Martin Mergili, Bernhard Frank, Jan-Thomas Fischer, Christian Huggel, and Shiva P Pudasaini. Computational experiments on the 1962 and 1970 landslide events at huascarán (peru) with r. avaflow: Lessons learned for predictive mass flow simulations. *Geomorphology*, 322:15–28, 2018.

[56] Martin Mergili, Shiva P Pudasaini, Adam Emmer, Jan-Thomas Fischer, Alejo Cochachin, and Holger Frey. Reconstruction of the 1941 glof process chain at lake palcacocha (cordillera blanca, peru). *Hydrology and Earth System Sciences*, 24(1):93–114, 2020.

[57] Martin Mergili, Jan-Thomas Fischer, and Shiva P Pudasaini. Process chain modelling with r. avaflow: lessons learned for multi-hazard analysis. In *Advancing Culture of Living with Landslides: Volume 2 Advances in Landslide Science*, pages 565–572. Springer, 2017.

[58] Martin Mergili, Michel Jaboyedoff, José Pullarello, and Shiva P Pudasaini. Back calculation of the 2017 piz cengalo–bondo landslide cascade with r. avaflow: what we can do and what we can learn. *Natural Hazards and Earth System Sciences*, 20(2):505–520, 2020.

[59] Seyed Ali Mousavi Tayebi, Saeid Moussavi Tayyebi, and Manuel Pastor. Depth-integrated two-phase modeling of two real cases: a comparison between r. avaflow and geoflow-sph codes. *Applied Sciences*, 11(12):5751, 2021.

[60] Hualin Cheng, Martin Mergili, and Yu Huang. Numerical analysis of debris flow erosion in the mountainous areas affected by the 2008 wenchuan earthquake using a depth-averaged two-phase model. *Natural Hazards*, pages 1–20, 2022.

[61] JN Procter, SJ Cronin, and MF Sheridan. Evaluation of titan2d modelling forecasts for the 2007 crater lake break-out lahar, mt. ruapehu, new zealand. *Geomorphology*, 136(1):95–105, 2012.

[62] R Williams, AJ Stinton, and MF Sheridan. Evaluation of the titan2d two-phase flow model using an actual event: Case study of the 2005 vazcún valley lahar. *Journal of Volcanology and Geothermal Research*, 177(4):760–766, 2008.

[63] E Bruce Pitman, Abani K Patra, Dinesh Kumar, Kouichi Nishimura, and Jiro Komori. Two phase simulations of glacier lake outburst flows. *Journal of Computational Science*, 4(1-2):71–79, 2013.

[64] Sylvaine J Charbonnier and Ralf Gertisser. Numerical simulations of block-and-ash flows using the titan2d flow model: examples from the 2006 eruption of merapi volcano, java, indonesia. *Bulletin of Volcanology*, 71:953–959, 2009.

[65] Stefania Sansone, D Zugliani, and G Rosatti. A mathematical framework for modelling rock–ice avalanches. *Journal of Fluid Mechanics*, 919, 2021.

[66] Gregor Ortner, Michael Bründl, Chahan M Kropf, Thomas Röösli, Yves Bühler, and David N Bresch. Large-scale risk assessment on snow avalanche hazard in alpine regions. *Natural Hazards and Earth System Sciences Discussions*, pages 1–31, 2022.

[67] Yves Bühler, Daniel von Rickenbach, Andreas Stoffel, Stefan Margreth, Lukas Stoffel, and Marc Christen. Automated snow avalanche release area delineation–validation of existing algorithms and proposition of a new object-based approach for large-scale hazard indication mapping. *Natural Hazards and Earth System Sciences*, 18(12):3235–3251, 2018.

[68] Yves Bühler, Peter Bebi, Marc Christen, Stefan Margreth, Lukas Stoffel, Andreas Stoffel, Christoph Marty, Gregor Schmucki, Andrin Caviezel, Roderick Kühne, et al. Automated avalanche hazard indication mapping on a statewide scale. *Natural Hazards and Earth System Sciences*, 22(6):1825–1843, 2022.

[69] Vitalii Zaginaev, Kristyna Falatkova, Bohumir Jansky, Miroslav Sobr, and Sergey Erokhin. Development of a potentially hazardous pro-glacial lake in aksay valley, kyrgyz range, northern tien shan. *Hydrology*, 6(1):3, 2019.

[70] Parameshwari Kattel, Khim B Khattri, Puskar R Pokhrel, Jeevan Kafle, Bhadra Man Tuladhar, and Shiva P Pudasaini. Simulating glacial lake outburst floods with a two-phase mass flow model. *Annals of Glaciology*, 57(71):349–358, 2016.

[71] M Cesca and Vincenzo D'Agostino. Comparison between flo-2d and ramms in debris-flow modelling: a case study in the dolomites. *WIT Transactions on Engineering Sciences*, 60:197–206, 2008.

[72] Matjaž Mikoš and Nejc Bezak. Debris flow modelling using ramms model in the alpine environment with focus on the model parameters and main characteristics. *Frontiers in Earth Science*, 8:605061, 2021.

[73] Alessandro Simoni, Maria Mammoliti, and Cristoph Graf. Performance of 2d debris flow simulation model ramms. In *annual international conference on geological and earth sciences GEOS*, 2012.

[74] Jianjun Gan and Yixia Sarah Zhang. Numerical simulation of debris flow runout using ramms: a case study of luzhuang gully in china. *Computer Modeling in Engineering and Sciences*, pages 981–1009, 2019.

[75] Brian W McARDELL. Field measurements of forces in debris flows at the illgraben: implications for channel-bed erosion. *International Journal of Erosion Control Engineering*, 9(4):194–198, 2016.

[76] Hedda Breien, Fabio V De Blasio, Anders Elverhøi, and Kaare Høeg. Erosion and morphology of a debris flow caused by a glacial lake outburst flood, western norway. *Landslides*, 5:271–280, 2008.

[77] T Bo Anderson and Roy Jackson. Fluid mechanical description of fluidized beds. equations of motion. *Industrial & Engineering Chemistry Fundamentals*, 6(4):527–539, 1967.

[78] Osborne Reynolds. Lvii. on the dilatancy of media composed of rigid particles in contact. with experimental illustrations. *The London, Edinburgh, and Dublin Philosophical Magazine and Journal of Science*, 20(127):469–481, 1885.

[79] Paul C Johnson and Roy Jackson. Frictional–collisional constitutive relations for granular materials, with application to plane shearing. *Journal of fluid Mechanics*, 176:67–93, 1987.

[80] Othmar Buser and Perry Bartelt. Production and decay of random kinetic energy in granular snow avalanches. *Journal of Glaciology*, 55(189):3–12, 2009.

[81] Peter A Thompson and Gary S Grest. Granular flow: friction and the dilatancy transition. *Physical review letters*, 67(13):1751, 1991.

[82] Peter W Rowe. The stress-dilatancy relation for static equilibrium of an assembly of particles in contact. *Proceedings of the Royal Society of London. Series A. Mathematical and Physical Sciences*, 269(1339):500–527, 1962.

[83] Richard M Iverson. Regulation of landslide motion by dilatancy and pore pressure feedback. *Journal of Geophysical Research: Earth Surface*, 110(F2), 2005.

[84] Lilach Goren, E Aharonov, D Sparks, and Renaud Toussaint. Pore pressure evolution in deforming granular material: A general formulation and the infinitely stiff approximation. *Journal of Geophysical Research: Solid Earth*, 115(B9), 2010.

[85] Paul Segall and James R Rice. Dilatancy, compaction, and slip instability of a fluid-infiltrated fault. *Journal of Geophysical Research: Solid Earth*, 100(B11):22155–22171, 1995.

[86] Roland Kaitna, Marisa C Palucis, Bereket Yohannes, Kimberly M Hill, and William E Dietrich. Effects of coarse grain size distribution and fine particle content on pore fluid pressure and shear behavior in experimental debris flows. *Journal of Geophysical Research: Earth Surface*, 121(2):415–441, 2016.

[87] Jacob Bear. *Dynamics of fluids in porous media*. Courier Corporation, 1988.

[88] Olivier Coussy. *Mechanics and physics of porous solids*. John Wiley & Sons, 2011.

[89] Stephane Roux and Farhang Radjai. Texture-dependent rigid-plastic behavior. In *Physics of dry granular media*, pages 229–236. Springer, 1998.

[90] Mickael Pailha and Olivier Pouliquen. A two-phase flow description of the initiation of underwater granular avalanches. *Journal of Fluid Mechanics*, 633:115–135, 2009.

[91] Karl Terzaghi. *Erdbaumechanik auf bodenphysikalischer Grundlage*. F. Deuticke, 1925.

[92] S NEMAT NASSER. On behavior of granular materials in simple shear. *Soils and Foundations*, 20(3):59–73, 1980.

[93] M. D. Bolton. The strength and dilatancy of sands. *Géotechnique*, 36(1):65–78, 1986.

[94] Guy Tinmouth Houlsby. How the dilatancy of soils affects their behaviour. 1991.

[95] Gustavo AM de Almeida, Paul Bates, Jim E Freer, and Maxime Souvignet. Improving the stability of a simple formulation of the shallow water equations for 2-d flood modeling. *Water Resources Research*, 48(5), 2012.

[96] Matthias Jakob, Oldrich Hungr, Oldrich Hungr, Scott McDougall, and Michael Bovis. Entrainment of material by debris flows. *Debris-flow hazards and related phenomena*, pages 135–158, 2005.

[97] SB Savage and K Hutter. The motion of a finite mass of granular material down a rough incline. *Journal of Fluid Mechanics*, 199:39–54, 1989.

[98] JS O'Brien, PY Julien, and WT Fullerton. Two-dimensional water flow and mudflow simulation. *Journal of Hydraulic Engineering*, 119(2):244–261, 1993.

[99] O Hungr. A model for the runout analysis of rapid flow slides, debris flows and avalanches. *Canadian Geotechnical Journal*, 32:610–623, 1995.

[100] D Laigle and P Coussot. Numerical modeling of mudflows. *Journal of Hydraulic Engineering*, 123(7):617–623, 1997.

[101] Richard M Iverson and Roger P Denlinger. Flow of variably fluidized granular masses across three-dimensional terrain: 1. coulomb mixture theory. *Journal of Geophysical Research: Solid Earth*, 106(B1):537–552, 2001.

[102] Roger P Denlinger and Richard M Iverson. Flow of variably fluidized granular masses across three-dimensional terrain: 2. numerical predictions and experimental tests. *Journal of Geophysical Research: Solid Earth*, 106(B1):553–566, 2001.

[103] D Rickenmann. Empirical relationships for debris flows. *Natural Hazards*, 19:47–77, 1999.

[104] Yongqi Wang, Kolumban Hutter, and Shiva P Pudasaini. The savage-hutter theory: A system of partial differential equations for avalanche flows of snow, debris, and mud. *ZAMM-Journal of Applied Mathematics and Mechanics/Zeitschrift für Angewandte Mathematik und Mechanik: Applied Mathematics and Mechanics*, 84(8):507–527, 2004.

[105] C Graf, M Christen, BW McArdell, and P Bartelt. An overview of a decade of applied debris-flow runout modeling in switzerland: challenges and recommendations. pages 685–692, 2019.

[106] D Rickenmann, DMBW Laigle, BW McArdell, and J Hübl. Comparison of 2d debris-flow simulation models with field events. *Computational Geosciences*, 10(2):241–264, 2006.

[107] Brian W McArdell and Mario Sartori. The illgraben torrent system. In *Landscapes and Landforms of Switzerland*, pages 367–378. Springer, 2020.

[108] Richard M Iverson. The physics of debris flows. *Reviews of geophysics*, 35(3):245–296, 1997.

[109] B McArdell, P Bartelt, and J Kowalski. Field observations of basal forces and fluid pore pressure in a debris flow. *Geophysical Research Letters*, 34(L07406), 2007.

[110] K Schraml, B Thomschitz, BW McArdell, C Graf, and Kaitna R. Modeling debris-flow runout patterns on two alpine fans with different dynamic simulation models. *Natural Hazards and Earth System Science*, 15(7):1483–1492, 2015.

[111] Julia Kowalski. *Two-phase modeling of debris flows*. ETH Zurich, 2008.

[112] Julia Kowalski and Jim N McElwaine. Shallow two-component gravity-driven flows with vertical variation. *Journal of Fluid Mechanics*, 714:434–462, 2013.

[113] Kolumban Hutter and Lukas Schneider. Important aspects in the formulation of solid–fluid debris-flow models. part i. thermodynamic implications. *Continuum Mechanics and Thermodynamics*, 22(5):363–390, 2010.

[114] Fritz Schlunegger, Alexandre Badoux, Brian W McArdell, Corina Wendeler, David Schnydrig, Dirk Rieke-Zapp, and Peter Molnar. Limits of sediment transfer in an alpine debris-flow catchment, illgraben, switzerland. *Quaternary Science Reviews*, 28(11-12):1097–1105, 2009.

[115] Alexandre Badoux, Christoph Graf, Jakob Rhyner, Richard Kuntner, and Brian W McArdell. A debris-flow alarm system for the alpine illgraben catchment: design and performance. *Natural hazards*, 49(3):517–539, 2009.

[116] Massimo Greco, Michele Iervolino, Angelo Leopardi, and Andrea Vacca. A two-phase model for fast geomorphic shallow flows. *International Journal of Sediment Research*, 27(4):409–425, 2012.

[117] CG Johnson, BP Kokelaar, Richard M Iverson, M Logan, RG LaHusen, and JMNT Gray. Grain-size segregation and levee formation in geophysical mass flows. *Journal of Geophysical Research: Earth Surface*, 117(F1), 2012.

[118] Tamotsu Takahashi. Debris flow. *Annual review of fluid mechanics*, 13(1):57–77, 1981.

[119] J Visser. Van der waals and other cohesive forces affecting powder fluidization. *Powder Technology*, 58(1):1–10, 1989.

[120] Perry BARTELT, Brian McARDELL, Christoph GRAF, Marc CHRISTEN, and Othmar BUSER. Dispersive pressure, boundary jerk and configurational changes in debris flows. *International Journal of Erosion Control Engineering*, 9(1):1–6, 2016.

[121] P Bartelt, O Buser, C Vera Valero, and Y Bühler. Configurational energy and the formation of mixed flowing/powder snow and ice avalanches. *Annals of Glaciology*, 57(71):179–188, 2016.

[122] P Bartelt and O Buser. The relation between dilatancy, effective stress and dispersive pressure in granular avalanches. *Acta Geotechnica*, 11(3):549–557, 2016.

[123] e Savary and Yves Zech. Boundary conditions in a two-layer geomorphological model. application to a. *Journal of Hydraulic Research*, 45(3):316–332, 2007.

[124] Kyle T Mandli. *Finite volume methods for the multilayer shallow water equations with applications to storm surges.* PhD thesis, 2011.

[125] B Salm. Flow, flow transition and runout distances of flowing avalanches. *Annals of Glaciology*, 18:221–226, 1993.

[126] Aronne Armanini, Luigi Fraccarollo, and Giorgio Rosatti. Two-dimensional simulation of debris flows in erodible channels. *Computers & Geosciences*, 35(5):993–1006, 2009.

[127] Manuel J Castro, Jose A Garcia-Rodriguez, Jose M Gonzalez-Vida, Jorge Macias, Carlos Pares, and M Elena Vazquez-Cendon. Numerical simulation of two-layer shallow water flows through channels with irregular geometry. *Journal of Computational Physics*, 195(1):202–235, 2004.

[128] Guiwen Rong, Xu Wang, Hui Xu, and Baiqing Xiao. Multifactor regression analysis for predicting embankment dam breaching parameters. *Journal of Hydraulic Engineering*, 146(2):04019051, 2020.

[129] Oldrich Hungr. Analysis of debris flow surges using the theory of uniformly progressive flow. *Earth Surface Processes and Landforms: The Journal of the British Geomorphological Research Group*, 25(5):483–495, 2000.

[130] Sabatino Cuomo, Manuel Pastor, Leonardo Cascini, and Giuseppe Claudio Castorino. Interplay of rheology and entrainment in debris avalanches: a numerical study. *Canadian Geotechnical Journal*, 51(11):1318–1330, 2014.

[131] Sabatino Cuomo, Manuel Pastor, Vittoria Capobianco, and Leonardo Cascini. Modelling the space–time evolution of bed entrainment for flow-like landslides. *Engineering geology*, 212:10–20, 2016.

[132] G Meyrat, B McArdell, Kseniya Ivanova, C Müller, and P Bartelt. A dilatant, two-layer debris flow model validated by flow density measurements at the swiss illgraben test site. *Landslides*, pages 1–12, 2021.

[133] Shiva P Pudasaini and Michael Krautblatter. The mechanics of landslide mobility with erosion. *Nature communications*, 12(1):6793, 2021.

[134] Richard M Iverson. Debris-flow mechanics. *Debris-flow hazards and related phenomena*, pages 105–134, 2005.

[135] Ralph Lugon and Markus Stoffel. Rock-glacier dynamics and magnitude–frequency relations of debris flows in a high-elevation watershed: Ritigraben, swiss alps. *Global and Planetary Change*, 73(3-4):202–210, 2010.

[136] Robert Kenner, Marcia Phillips, Jan Beutel, Martin Hiller, Philippe Limpach, Eric Pointner, and Martin Volken. Factors controlling velocity variations at short-term, seasonal and multiyear time scales, ritigraben rock glacier, western swiss alps. *Permafrost and Periglacial Processes*, 28(4):675–684, 2017.

[137] R Lugon and M Monbaron. Stabilite des terrains meubles en zone de permafrost et changements climatiques. *Deux etudes de cas en Valais: le Ritigraben (Mattertal) et la moraine du Dolent (Val Ferret). Rapport scientifique final PNR*, 31, 1998.

[138] Markus Stoffel, Igor Lièvre, Delphine Conus, Michael A Grichting, Hugo Raetzo, Holger W Gärtner, and Michel Monbaron. 400 years of debris-flow activity and triggering weather conditions: Ritigraben, valais, switzerland. *Arctic, Antarctic, and Alpine Research*, 37(3):387–395, 2005.

[139] Evelyn Zenklusen Mutter and Marcia Phillips. Thermal evidence of recent talik formation in ritigraben rock glacier: Swiss alps. In *Tenth International Conference on Permafrost, Salekhard, Russia, The Fort Dialog-Iset*, volume 1, pages 479–483, 2012.

[140] Laura Bindereif. Simulation of debris flows at the ritigraben torrent, valais, switzerland. *Master thesis*, 2022.

[141] Thibaut Quillard, Gregory Franck, Thomas Mawson, Eduardo Folco, and Peter Libby. Mechanisms of erosion of atherosclerotic plaques. *Current opinion in lipidology*, 28(5):434, 2017.

[142] Shiva P Pudasaini and Jan-Thomas Fischer. A mechanical model for phase separation in debris flow. *International Journal of Multiphase Flow*, 129:103292, 2020.

[143] Dan H Shugar, Aaron Burr, Umesh K Haritashya, Jeffrey S Kargel, C Scott Watson, Maureen C Kennedy, Alexandre R Bevington, Richard A Betts, Stephan Harrison, and Katherine Strattman. Rapid worldwide growth of glacial lakes since 1990. *Nature Climate Change*, 10(10):939–945, 2020.

[144] Oldrich Hungr, Serge Leroueil, and Luciano Picarelli. The varnes classification of landslide types, an update. *Landslides*, 11(2):167–194, 2014.

[145] Thomas C Pierson. Hyperconcentrated flow—transitional process between water flow and debris flow. In *Debris-flow hazards and related phenomena*, pages 159–202. Springer, 2005.

[146] Meyrat. Voellmy-type mixture rheologies for dilatant, two-layer debris flow models. *Landslide*, 1(1):1–2, 2007.

[147] Shiva P Pudasaini and Kolumban Hutter. *Avalanche dynamics: dynamics of rapid flows of dense granular avalanches*. Springer Science & Business Media, 2007.

[148] Demian Schneider, Christian Huggel, Alejo Cochachin, Sebastian Guillen, and Javier Garcia. Mapping hazards from glacier lake outburst floods based on modelling of process cascades at lake 513, carhuaz, peru. *Advances in Geosciences*, 35:145–155, 2014.

[149] Dmitry A Petrakov, Sergey S Chernomorets, Karina S Viskhadzhieva, Mikhail D Dokukin, Elena A Savernyuk, Maxim A Petrov, Sergey A Erokhin, Olga V Tutubalina, Gleb E Glazyrin, Alyona M Shpuntova, et al. Putting the poorly documented 1998 glof disaster in shakhimardan river valley (alay range, kyrgyzstan/uzbekistan) into perspective. *Science of The Total Environment*, 724:138287, 2020.

[150] Marcelo A Somos-Valenzuela, Rachel E Chisolm, Denny S Rivas, Cesar Portocarrero, and Daene C McKinney. Modeling a glacial lake outburst flood process chain: the case of lake palcacocha and huaraz, peru. *Hydrology and Earth System Sciences*, 20(6):2519–2543, 2016.

[151] V Zaginaev, D Petrakov, S Erokhin, A Meleshko, Markus Stoffel, and Juan Antonio Ballesteros-Canovas. Geomorphic control on regional glacier lake outburst flood and debris flow activity over northern tien shan. *Global and Planetary Change*, 176:50–59, 2019.

[152] V Zaginaev, Juan Antonio Ballesteros-Canovas, S Erokhin, E Matov, D Petrakov, and Markus Stoffel. Reconstruction of glacial lake outburst floods in northern tien shan: Implications for hazard assessment. *Geomorphology*, 269:75–84, 2016.

[153] Hervé Vicari, Steinar Nordal, and Vikas Thakur. The significance of entrainment on debris flow modelling: the case of hunnedalen, norway. In *Challenges and Innovations in Geomechanics: Proceedings of the 16th International Conference of IACMAG-Volume 2 16*, pages 507–514. Springer, 2021.

[154] Taro Uchida, Yuki Nishiguchi, Brian W McArdell, and Yoshifumi Satofuka. The role of the phase shift of fine particles on debris flow behavior: an numerical simulation for a debris flow in illgraben, switzerland. *Canadian Geotechnical Journal*, 58(1):23–34, 2021.

[155] Roger LeB Hooke and Neal R Iverson. Grain-size distribution in deforming subglacial tills: role of grain fracture. *Geology*, 23(1):57–60, 1995.

[156] Holger Frey, Christian Huggel, Rachel E Chisolm, Patrick Baer, Brian McArdell, Alejo Cochachin, and Cesar Portocarrero. Multi-source glacial lake outburst flood hazard assessment and mapping for huaraz, cordillera blanca, peru. *Frontiers in Earth Science*, 6:210, 2018.

[157] Vít Vilímek, Jan Klimeš, Adam Emmer, and Miroslava Benešová. Geomorphologic impacts of the glacial lake outburst flood from lake no. 513 (peru). *Environmental Earth Sciences*, 73:5233–5244, 2015.

[158] Vit Vilimek, Marco Luyo Zapata, Jan Klimeš, Zdeněk Patzelt, and Nelson Santillan. Influence of glacial retreat on natural hazards of the palcacocha lake area, peru. *Landslides*, 2(2):107–115, 2005.

[159] A Emmer and V Vilimek. New method for assessing the susceptibility of glacial lakes to outburst floods in the cordillera blanca, peru. *Hydrology and Earth System Sciences*, 18(9):3461–3479, 2014.

[160] Mark Carey. *In the shadow of melting glaciers: Climate change and Andean society*. Oxford University Press, 2010.

[161] Stephen G Evans, Nicholas F Bishop, Lionel Fidel Smoll, Patricio Valderrama Murillo, Keith B Delaney, and Anthony Oliver-Smith. A re-examination of the mechanism and human impact of catastrophic mass flows originating on nevado huascaran, cordillera blanca, peru in 1962 and 1970. *Engineering Geology*, 108(1-2):96–118, 2009.

[162] Holger Frey, Christian Huggel, Rachel E Chisolm, Patrick Baer, Brian McArdell, Alejo Cochachin, and César Portocarrero. Multi-source glacial lake outburst flood hazard assessment and mapping for huaraz, cordillera blanca, peru. *Frontiers in Earth Science*, 6:210, 2018.

Acknowledgments

I would like to thank my supervisor Perry Bartelt for his support all along the thesis. I am grateful to my ETH supervisor Christoph Müller for the scientific inputs and the interesting discussions. Many thanks also go to Jens, Nicki, Alexander, Chris and Meng, whose comments and advice were very helpful.

The working team is primordial. Special thanks to all the RAMMS group (Jess, Adi, Andrin, Marc, Guang, Gregor S., Gregor O., Ksenyia, Olga and Jöel) for your support, help and jokes during coffee breaks.

This thesis will not have been possible without my family. Endless thanks to my parents, la Puce et le Djet and to my grandparents Jacqueline, Agnès, Louis-Charles and Francis for their endless support in all my projects. I also would like to thank my cousin Nicolas, Régis, Axel, Charles, Marc, Noé, Lucas, Arno and especially Chiara, who came to help me with the experiments.

Aside from the scientific aspect I would like to thank all my friends who have supported me during these four and half years. Thanks to Greg Le Marseillais for the hangover mornings, Martin Le Lutin for the climbing moments, Michi to make exhausted me while running and biking and Camille Le Chamois for the chill moments in In den Büelen.

Many thanks to my girlfriend Wieke, who supported me as much as she can during the end of my thesis and was able to deal with my typical PhD work schedule (this should improve), as well as my typical Meyrat's character (not this...).

A special thought to Thibault Gerber, alias Le Gauche, for all the good moments we spent together. You did not directly help me for the thesis, but life was much nicer and funnier with you.

Curriculum Vitae

Personal information

Name:	Guillaume Meyrat
Born:	2nd August 1993
Nationality:	Swiss
Email:	guillaume.meyrat@slf.ch

Academic background

2018-present: Doctoral student at WSL Insitute for Snow and Avalanche Research SLF, Davos, Switzerland.

2015-2017:   Master of Science MSc inb Physics, Ecole Polytechnique federal de Lausanne, Lausanne, Switzerland.

2011-2014:   Bachelor in Physics, Ecole Polytechnique federal de Lausanne, Lausanne, Switzerland.

Work experience

2017-2018:   Internship for Rolex, Bienne

Journal Publications

Meyrat, G., McArdell, B., Ivanova, K., Müller, C. and Bartelt, P., 2022. A dilatant, two-layer debris flow model validated by flow density measurements at the Swiss Illgraben test site. Landslides, 19(2), pp.265-276.(Chapter 2)

Caviezel, Andrin, et al. "The relevance of rock shape over mass—implications for rockfall hazard assessments." Nature Communications 12.1 (2021): 5546.

Papers in preparation

Meyrat, G., McArdell, B., Müller, C., Münch, J. and Bartelt, P.. Voellmy-Type Mixture Rheologies for Dilatant, Two-layer Debris Flow Models. (Chapter 3)

Meyrat, G., Münch, J., Cicoira, A., McArdell, B., Müller, C., H. Frey, and Bartelt, P.. Simulating glacier Lake outburst floods (GLOFs) with a two-phase/layer debris flow model considering fluid-solid flow transitions (Chapter 4)

Conference proceedings

5th International Conference Debris Flows: disasters, risk, forecast, protection 2018, GEOSUM-MIT 2019, Queen's University Queen's University 2019, European Geosciences Union 2019, European Geosciences Union 2020, European Geosciences Union 2021, European Geosciences Union 2022, CCAMM Workshop 2018, CCAMM Workshop 2019, CCAMM Workshop 2020, CCAMM Workshop 2021, CCAMM Workshop 2022, CCAMM Annual Meeting 2019 CCAMM Annual Meeting 2020.